Università degli Studi di Cagliari
PhD Thesis

DOTTORATO DI RICERCA

in SCIENZE E TECNOLOGIE CHIMICHE

Ciclo XXVII

Settore scientifico disciplinare di afferenza CHIM/02

Erika Conca

Preparation and investigation of new heterostructures for prospective energetic and biomedical applications

Coordinatore Dottorato: Prof. Mariano Casu

Relatore: Prof. Maria Francesca Casula

A.A. 2013 – 2014

*Chiunque si pone come arbitro in materia di conoscenza
è destinato a naufragare nella risata degli dei.*

Albert Einstein

Contents

Introduction

Nanotechnologies, defined as the ensemble of disciplines aiming at manipulating matter on an atomic or molecular scale and at exploiting the corresponding properties, have recently emerged as one of the most relevant research fields due to its implications in applied science and technological applications.

Nanocrystals (NCs) with a uniformly crystalline structure and at least one dimension in the range 1÷100 nanometers, play a key role as building blocks for the assembly of innovative materials and devices for nanotechnology. A wide variety of nanocrystalline materials showing metallic, semiconducting, magnetic properties or their combinations are now available. It is well documented that nanocrystals exhibit physical properties, ranging from mechanical strength, chemical reactivity and conductivity that depend on their size and structure and differ from those of the corresponding bulk materials.

For this reason, nanocrystals are regarded as promising building blocks for the fabrication of functional materials with targeted nanotechnological application.

In particular, in semiconducting nanocrystals the formation of a set of discrete energy levels, at which the carriers can exist, results in quantum effects. Size restricts the movements of the charge carriers forcing them into a quantum confinement and is responsible for new properties. Again, magnetic materials with nanometric size may exhibit single domain structures, which reflect in unique physical properties such as superparamagnetism, enhanced coercivity, quantum tunnelling of the magnetization and giant magnetoresistance with respect to multi domain bulk magnets.

The controlled manufacture of matter at the nanoscale is considered therefore as a promising route to obtain novel materials which can be exploited in optical, electronic, photovoltaic and magnetic nanotechnological applications.

Within this framework, this PhD thesis has been focused on the design, preparation and characterization of heterostructures constituted by nanomaterials of different composition, which could be employed in two relevant areas such as energy and biomedicine.

In particular, we have addressed the preparation by chemical solution routes of heterostructures which include different domains (metal-semiconductor and metal-magnet) with the aim to develop nanocrystalline new materials with improved and combined functionalities.

A key aspect which has been taken into account is how to control the connection between the domains with different functionalities by tuning appropriate synthetic parameters of high temperature colloidal procedures and how this can be exploited to produce heterostructures with well-controlled morphology and microstructure.

In particular, metal-semiconductor heterostructures made out of platinum tips deposited at controlled sites of a chalcogenides semiconductor with a branched octapod morphology were

achieved. As the semiconducting domain is able to absorb solar light whereas the noble metal tip is capable to catalyze chemical reactions, it is prospected that the developed materials, i.e. CdSe@CdS-Pt octapods, are active as solar conversion devices and photocatalysis, with particular reference to hydrogen production through optimization of the redox process behind the photocatalytic water splitting reaction. Photophysical investigation of CdSe@CdS-Pt octapods enabled us to point out the effect of heterostructure morphology-properties relationship, as it was found that two regimes for capture of photoexcited electrons by Pt domains take place depending on the location of the metal tips onto the semiconductor octapods. When Pt is deposited at the octapod tip a slow capture takes place after energy relaxation in the semiconductor and result in large spatial separation of charges; while when Pt covers the whole octapods surface an ultrafast capture of hot electrons occurs, and charge separation happens faster than energy relaxation and Auger recombination.

As an alternative route to the fabrication of multifunctional nanostructures including different domains, the potential of high temperature polymer-mediated hydrolysis in producing magnetic clusters, which are aggregates constituted of many single crystallite approximately 10 nm in size, has been explored.

Such magnetic clusters retain the peculiar properties of the constituent nanoparticles such as superparamagnetism, while exhibiting specific features such as higher magnetization and stability which are advantageous for practical use. Here, the possibility to fine-tune the properties of the clusters by varying the composition of the primary particles has been investigated by including metal nanoparticles (Au, Ag, Pt) and through doping the iron oxide with manganese. This research has been achieved in order to perform a systematic study of the correlation between morpho-structural and magnetic and relaxometric properties, which may be employed for their potential use in biomedical field.

The development of novel magnetic doped clusters has enabled to investigate the relaxometric and heat mediator behaviour of the novel materials, in order to evaluate their potential in biomedicine as prospective novel contrast agents for detection through Magnetic Resonance Imaging and as therapeutic tools in Magnetic Fluid Hyperthermia.

In addition to contributing to the understanding of the mechanisms behind the preparation of functional and multifunctional heterostructures, this thesis also aims at elucidating the structure-properties relationship at the nanoscale in materials with highly controlled compositional and morphological features. To this end, extensive morphological and structural characterization was carried out by a multi technique approach including in particular X-Ray diffraction, conventional and advanced transmission electron microscopy techniques, X-ray absorption spectroscopy, UV-visible spectroscopy and dynamic light scattering.

The research work is presented according to the following thesis outline:

- Chapter 1 deals with a short review on theoretical background, synthetic approaches and physical and chemical properties of semiconductor nanocrystals and magnetic nanocrystals. An overview on application of semiconductor and magnetic nanocrystals in two relevant fields such as energy and biomedicine, respectively, is also provided.

- Chapter 2 reports on the design and applications of nanometric metal-semiconductor heterostructures. Here we will discuss in detail the formation of CdSe@CdS-Pt nanocrystal hybrid materials, obtained by synthesizing Pt metal nanoparticles onto preformed CdSe@CdS octapod semiconductor obtained by the seeded growth approach. We will present the physico-chemical properties of the developed heterostructures, as obtained by a systematic structural and morphological characterization. The optical properties of these new materials, performed by ultrafast optical spectroscopy in collaboration with Prof. Michele

Saba at the Department of Physics of the University of Cagliari, will also be presented and correlated to the dynamics of charges carriers of the nanocrystals, which can in turn be used to predict their prospective use in photocatalysis.

- Chapter 3 describes the synthesis and characterization of magnetic nanoclusters heterostructures based on iron oxide which were in part developed under the supervision of Dr. Antonios Kanaras during a research visit at the University of Southampton (UK). Here, a discussion on the hydrolysis approach adopted in order to produce doped magnetic nanoclusters based on iron oxide, i.e. noble metal $M-Fe_3O_4$ (M= Au, Ag, Pt) and $Mn_xFe_{3-x}O_4$ which may used as heat mediators on hyperthermia treatment cancer and as contrast agents for magnetic resonance imaging is reported. In these samples, the morpho-structural data were correlated to their magnetic and relaxometric behaviour, which was investigated through SQUID magnetometry and diffusion curves in collaboration with Dr. Teresa Pellegrino and coworkers at the Italian Institute of Technology (IIT, Genova).

Finally, conclusive remarks and future developments arising from this work are discussed.

Chapter 1

Nanomaterials and their properties

In recent years, nanotechnology has become among the most important and intriguing fields in Physics, Chemistry, Engineering and Biology. Nanomaterials have, by definition, one or more dimension in the nanometric scale (≤ 100 nm) range and show novel properties from their bulk materials. The most relevant characteristics, among many others, at the nanoscale are as follows: i) the small size of the particles, which leads to an increased surface area to volume ratio; ii) the increased surface area to volume ratio, which may result in the dominance of the surface atoms of the nanoparticle over those in its interior. For example, about 50% of the atoms in a spherical 3 nm particle are located at the surface and interface boundaries. [1]

The electronic structure, conductivity, reactivity, melting temperature and mechanical properties have all been observed to change when particles become smaller than a critical size. The dependence of the behaviour on the particle sizes can allow one to engineer their properties. It is well established that nanomaterials have enormous potential to contribute to significant advances over a wide and diverse range of technological areas, ranging from producing stronger and lighter materials, to shortening the delivery time of nanostructured pharmaceuticals to the body's circulatory system, increasing the storage capacity of magnetic tapes and providing faster switches for computers. [1]

The research area of nanotechnology is interdisciplinary, covering a wide variety of subjects ranging from the chemistry of the catalysis of nanoparticles, to the physics of the quantum dot laser. As a result, researchers in any one area need to reach beyond their expertise in order to appreciate the broader implications of nanotechnology and learn how to contribute to this exciting new field.

The broad implications of nanotechnology, together with the possibility of investigating the fundamental physico-chemical properties at the nanoscale, have inspired the preparation of more and more advanced materials over the past decades. While research has initially been focused on single nanoparticles, the attention has then turned to heterogeneous, composite and sandwich nanostructures. Among composite nanostructures, concentric multilayered

nanoparticles referred to as "core@shell" have emerged in the 1990s as technologically relevant nanostructures. Finally, many complex architectures have been prepared by controlled assembly of nanostructured building blocks. [2]

In this chapter, the fundamental properties of semiconductor and magnetic nanoparticles, which are the focus of this research, will be summarized.

1.1 Semiconductor nanocrystals and their properties

1.1.1 Semiconductor nanocrystals

In the last decades, semiconductor nanocrystals have attracted considerable interest in the field of nanoscience and nanotechnology. Many important nanostructures are composed of the group IV elements as Si or Ge, type III-V semiconducting compounds such as GaAs, or type II-VI semiconducting materials such as CdS, refer to columns of the periodic table into which these elements are formed. [1]

Over decades, the ability to control the surfaces of semiconductors with near atomic precision has led to a further idealization of semiconductor structures: quantum wells, wires and dots. Ignoring for a moment the detailed atomic level structure of the material, it is possible to imagine simple geometric objects of differing dimensionality (2,1 and 0), in each case made out of homogeneous semiconductor material and with perfect surface termination. Such structures should exhibit the idealized variations in density of electronic states predicted by quantum mechanics, with the continuous levels of the 3d case evolving into the discrete states of the 0-dimensional case. [3] (Figure 1.1)
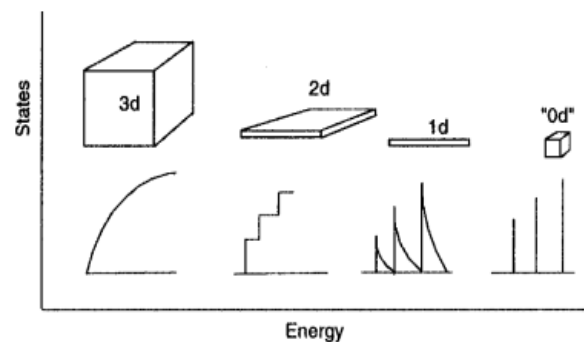

Fig.1.1 Idealized density of states for one band of a semiconductor structure of 3,2,1 and "0" dimensions. In the 3d case the energy levels are continuous, while in the "0d" or molecular limit the levels are discrete.

The main reason for the vast interest of semiconductor NCs is due on their electronic behaviour, the relatively easy and cheap approach to their fabrication, their robustness, as well as the flexible manipulation of their surface. The most striking property of nanoparticles made of semiconducting elements is the pronounced changes in their size-dependent optical properties compared to those of the bulk material, how we will discuss in detail forward. This particular behaviour can be explained by taking into account the fact that, at the nanometric scale, the laws of classical physics are no more valid while quantum mechanics has to be considered. [4] In a bulk semiconductor (Fig.1.2.a) the band gap arises from a separation in energy between the top filled energy level of the *valence band* and the nearest unfilled level in the *conduction band* above it and is an intrinsic physical property that depends solely on the type (composition and polymorph) of bulk semiconductor. [5]

Going from macroscale to nanoscale dimensions, in particular when the radius of the semiconductor nanocrystal is smaller than the exciton Bohr radius, i.e. the average distance

between the electron in the conduction band and the hole it leaves behind in the valence band, there is quantization of the energy levels according to Pauli's exclusion principle (Fig.1.2.a); the energy band gap becomes no longer a fixed parameter which depends only on the material. If we consider a semiconductor particle with size of about 10 nm, which corresponds to about 10^4 atoms, electronic excitations are affected by the particles boundaries and respond to changes in the particle size by adjusting their energy spectra, that is we are in a state of *quantum confinement*. In these conditions, the particle size directly affects the energy of band gap. This phenomenon is known as *quantum size effect,* so that nanoscale particles that exhibit it are often referred to as *quantum dots* (QD). [5]
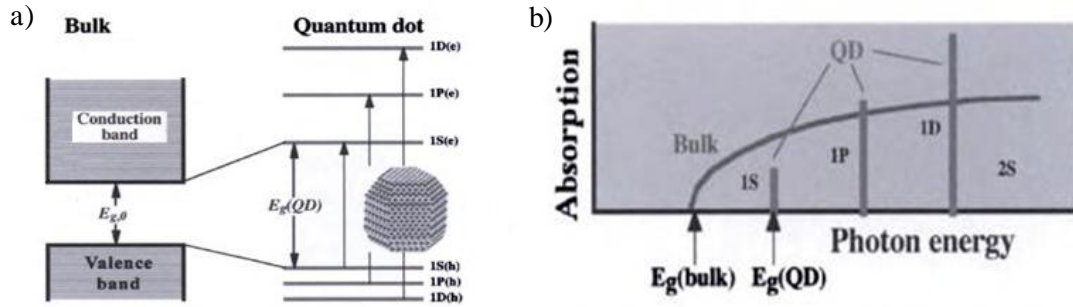

Fig.1.2 a) The electronic structure of quantum dots compared to bulk semiconductor; b) a schematic representation of the continuous absorption spectrum of a bulk semiconductor (curved line) compared to the discrete absorption spectrum of a QD (vertical bars). [5]

In the first approximation, this effect can be described using a simple quantum model. If we imagine a particle free to move in a three-dimensional potential well, performing the calculations, this model predicts that the size-dependent contribution to the energy gap is simply proportional to $1/R^2$. This model can be applied to the quantum dot. In detail, if we consider a spherical particle of radius R, the increase of $E_g(QD)$ with respect to $E_g(bulk)$ is given by the following equation:

$$E_g(QD) \approx E_g(bulk) + \frac{\hbar^2 \pi^2}{2m_{eh}R^2}$$

where m_{eh} is the reduced mass of the electron-hole pair in the quantum dot. [5]

Therefore, reducing the size of the particles, the energy separation between the various states inside the bands increases, especially at the band edges. This in turn influences the band gap, which also increases.

In addition to increasing energy gap, quantum confinement leads to a collapse of the continuous energy bands of the bulk material into discrete, "atomic" energy levels. These well-separated QD states can be labelled using atomic-like notations (1S, 1P, 1D, etc). As opposed to the continuous absorption spectrum of a bulk semiconductor, the discrete structure of energy states leads to the discrete absorption spectrum of QDs (Fig.1.2.b).

Thus, the size of a semiconductor nanocrystal influences its optical properties trough two effects: the density of the electronic states approaches that of a molecule, i.e. it becomes discrete near the band edges; also, the energy separation between occupied states and empty states increases.[6]

The optical properties of a nanocrystal also depend on its shape. In fact, by changing the shape of the nanocrystal it is possible to change its electronic structure, i.e. the energy position of the electronic states, the overall shape of the wavefunction, its symmetry, the polarization in the absorption/emission of light and the localization of the carriers.[7] In particular, the electronic states of different nanocrystal shapes (spherical dot, rod, arrow,

tetrapod) of the same semiconductor nanocrystal can be dramatically different, besides their energy band gaps. For example, the band gap of the CdSe rod is about 270 meV larger than that of the corresponding dot of the same volume [8] because of stronger quantum confinement in the lateral direction. The most compact shape, the spherical dot, has the smallest band gap, hence the smallest quantum confinement effect.

Also, the overall shapes of the electronic and the hole states are qualitatively different and there is so one-to-one correspondence between them. Nevertheless, the first few electronic and hole states look similar in the case of quantum rods. Instead, for shapes such as spherical dot, arrow and teardrop, the higher excited electronic states tend to develop nodes in the envelope function along the c axis and the nodes of the first few hole states are in the xy plane. Definitively, it is the overall shape that controls the qualitative picture of the single-particle states.

Also, if one dimension of the nanocrystals is stretched, such as in nanorods, the density of states will change considerably, because the quantum confinement will be now felt by the carriers only along the two others dimensions, along which the levels will be still quantized, while little or no confinement will be felt along the stretched direction. [9]

Based on the above discussion, applications in optoelectronics have driven the need for the design of semiconductor particles with fine-tuned size and shape.

Many protocols have been recently developed for synthesizing semiconductor nanocrystals. In particular, all the synthetic methods in solution can be grouped in two main categories, the synthesis in aqueous media and the colloidal synthesis in high boiling temperature solvents at high temperature. The latter approach gives the possibility to control the uniformity of the size, shape and composition of the nanocrystals in a much more controlled way. As a consequence of the highly controlled morphological and structural features, nanocrystals obtained by colloidal synthesis at high temperature exhibit much better optical properties, although the procedure to obtain them is more laborious. [10]

- Core@shell semiconductor nanoparticles

Over the past two decades, heterogeneous, composite or sandwich colloidal semiconductor particles have emerged as materials with better efficiency than their corresponding single particles. A successful strategy to improve the properties of such semiconductor materials is based on overgrowing semiconducting nanocrystals called "core" with a shell of a second semiconductor, resulting in the most typical configuration of core@shell nanosystems. [11]

In such structure, the shell passivates the surface of the optically active core by reducing the number of surface dangling bonds which could have a detrimental effect on the fluorescence quantum yield (QY) acting as trap states for charge carriers. In addition, the shell improves the stability of the core against photodegradation, protecting it from the surrounding medium, thus making the nanocrystals less sensitive to environmental changes and surface chemistry. Typical examples are combinations of semiconductors of type II–VI, IV–VI, III–V, such as CdS@ZnS, CdSe@ZnS, CdSe@CdS and InAs@CdSe, to mention a few.

Depending on the relative conduction and valence band edge alignment of the core and the shell, core@shell nanosystems can be classified in three different categories, denominated type I, reverse type I and type II (Fig. 1.3). Although this classification strictly applies to bulk semiconductor materials, it is also extended to core@shell nanocrystals.
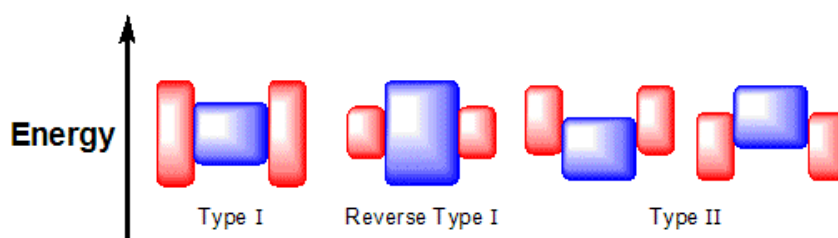
Fig.1.3 The three types of core@shell nanocrystals. The upper and lower edges represent the upper and lower energy edges of the core (blue) and the shell (red).

In *type-I systems,* the bandgap of the shell material is larger than that of the core and both electrons and holes are confined in the core. An example of this type of nanostructures is constituted by CdSe@ZnS core@shell nanocrystals. Shell growth is accompanied by a small red shift (5–10 nm) of the excitonic peak in the UV-Vis absorption spectrum and the photoluminescence (PL) wavelength: this observation is attributed to a partial leakage of the exciton into the shell material. [12]

In *reverse type-I systems*, a material with narrower bandgap is overgrown onto the core with wider bandgap. Charge carriers are at least partially delocalized in the shell and the emission wavelength can be tuned by adjusting the shell's thickness. Generally, a significant red-shift of the bandgap with the shell thickness is observed. The most extensively analyzed systems of this type are CdS@HgS, CdS@CdSe and ZnSe@CdSe. The resistance against photobleaching and the fluorescence quantum yield of these systems can be improved by the growth of a second shell of a larger-bandgap semiconductor on the core@shell NCs.

In *type-II systems*, shell growth aims at a significant red shift of the emission wavelength of the NCs. The staggered band alignment leads to a smaller effective bandgap than each one of the constituting core and shell materials. The interest on these systems is the possibility to manipulate the shell thickness and thereby tune the emission colour towards spectral ranges, which are difficult to attain with other materials. Type-II NCs have been developed in particular for near-infrared emission, using for example CdTe@CdSe or CdSe@ZnTe. In contrast to type-I systems, the photoluminescence decay times are strongly prolonged in type-II NCs due to the lower overlap of the electron and hole wave functions.

Among all these core@shell systems, CdSe@CdS semiconductor nanocrystals are the most widely investigated in terms of size and shape control, because of their unique optical properties (Fig. 1.4). [13]
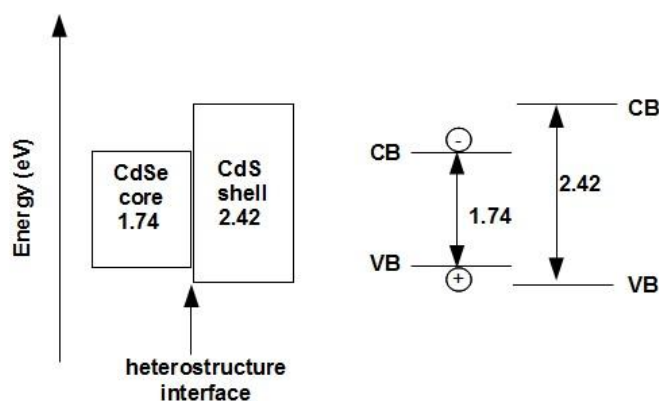

Fig.1.4 CdSe@CdS core@shell semiconductor nanocrystal band-edge alignment. VB is the valence band, CB is the conduction band.

In this work, CdSe@CdS dot@rods and dot@octapods core@shell nanocrystals, whose preparation routes will be described in the next paragraph, were investigated.

- Preparation of shape-controlled core@shell nanoparticles based on chalcogenides

Over the past decades, different approaches were developed for the synthesis of II-VI semiconductors such as cadmium chalcogenide (CdE with E = sulfide, selenide and telluride) because of their unmatched light absorption and emission properties. CdE nanocrystals were probably the first material used to demonstrate quantum size effects, corresponding to a change in the electronic structure with size. Since the pioneering studies on quantum dots, cadmium chalcogenides have been obtained in different aspect ratios and morphologies, such as rods, arrows, tetrapods and multi-armed nanocrystals.[14]

Among bottom-up approaches for nanomaterials synthesis, colloidal route has enabled to obtain structures with a high degree of control in terms of size and yield. Chalcogenide semiconductor nanocrystals are commonly synthesized through this procedure by thermal decomposition of an organometallic precursor dissolved in an solvent containing the source of chalcogenide and a stabilizing material (surfactant, polymer or capping ligand). Stabilizing molecules bound to the surface of particles, control their growth and prevent their aggregation although surfactants may also serve as solvents. Upon heating a reaction medium to a sufficiently high temperature, the precursors chemically transform into active atomic or molecular species (monomers); these then form nanocrystals, whose subsequent growth is greatly affected by the presence of surfactant molecules. The formation of the nanocrystals involves two steps: nucleation of an initial 'seed' and growth. In the nucleation step, precursors decompose or react at a relatively high temperature to form a supersaturation of monomers followed by a burst of nucleation of nanocrystals. These nuclei then grow by incorporating additional monomers still present in the reaction medium.[15]

Colloidal synthesis is regarded as the most suitable route for the preparation of core@shell NCs with a uniform thickness of the shell material. In particular, colloidal route of core@shell semiconductor nanocrystals through the seeded-growth approach involves the formation of a desired crystalline phase in the presence of surfactant molecules which coordinate the crystal surface, forming the seeds which will later constitute the core material of the final NCs. Later, injection of a solution containing the precursors of another material under conditions which favour heterogeneous growth, will result in the growth of a shell on top of the pre-formed seed.

This allows for the generation of semiconductor heterostructures with monodisperse size and variable shape, depending on the size of the seed and on the specific reaction conditions, such as concentration and temperature of the precursors.[15]

An additional advantage is that the shape of the core@shell NCs can be controlled by promoting anisotropic growth through specific adsorption of surfactants to individual crystallographic facets, thus altering their relative growth rates.[15] In addition, at the nanoscale dimensions, also the surface free energy contribute in determining nanocrystal shape.

For example, CdSe nanocrystals can occur in three distinct crystal forms: hexagonal wurtzite, cubic rock salt (observed only at high pressure) and cubic zinc blende, which relaxes to the wurtzite phase upon heating due to the relative high surface to volume ratio.

In particular, the metastable zinc blende structure of CdSe can be stabilized via surface strain effects, making it possible to engineer shaped functional materials, by tailoring crystal phases derived from both zinc blende and wurtzite phases; in this way, tetrapods structures of CdSe and CdTe have been synthesized.[16]

Hereafter, the method of preparation of CdSe@CdS different shaped core@shell NCs, obtained by seeded-mediated colloidal routes, i.e. dot@rods and dot@octapods, will be discussed in detail. These nanomaterials, indeed, in which the resulting morphology is strongly affected by the crystal structure of the CdSe core, have been used in this work to create hybrid metal-semiconductor heterostructures, as described in Chapter 2.

The synthesis of CdSe@CdS dot@rods is somehow well-established and relies on the growth of CdSe quantum dots in the wurtzite polymorph, which act as seeds for the anisotropic growth of CdS rods in the wurtzite phase. When this material forms in the hexagonal wurtzite lattice in the presence of suitable ligands, the lateral, non-polar facets can have much lower growth rates than the basal, polar facets and therefore the NCs can develop preferentially along their unique c axis, generating the rods shape. Furthermore, this axis does not have a plane of symmetry perpendicular to it, so that one can define a direction of polarity along this axis. As a consequence, the growth rates along one direction can be significantly different than other in the opposite side namely the two basal sides are not equivalent, both in terms of atomic arrangements at the surface and of dangling bonds.

The approach developed by Manna and coworkers for the fabrication of CdSe@CdS dot@rod nanocrystals [17] is based on the co-injection of appropriate precursors and preformed spherical CdSe nanocrystal seeds (nearly monodisperse in size) in a reaction flask that contains a mixture of hot surfactants suited for the anisotropic growth of CdS nanocrystals. In a typical synthesis of nanorods, CdO is decomposed in the presence of a mixture of trioctylphosphine oxide (TOPO), hexylphosphonic acid (HPA) and octadecylphosphonic acid (ODPA) in relative ratios that have been carefully optimized. The resulting solution is heated to 350 °C under inert atmosphere. Separately, a solution is prepared by dissolving sulphur precursor in trioctylphosphine (TOP) and by adding it to the CdSe dot nanocrystals, previously prepared, purified and solubilised in TOP. This solution is quickly injected in the flask, after which the temperature of the solution is allowed to recover at the pre-injection value and the synthesis is kept running for several minutes before stopping it by rapid quenching. Immediately after injection, CdS starts growing preferentially on the CdSe seeds rather than forming separate nuclei in solution because the activation energy for heterogeneous nucleation is much lower than that for homogeneous nucleation. As the homogeneous nucleation is bypassed by the presence of the seeds, all nanocrystals undergo almost identical growth conditions and therefore they maintain a narrow distribution of lengths and diameters during their evolution (Fig. 1.5).

The power of the seeded-growth approach carried out at high temperatures in suitable surfactant mixtures is therefore that large aspect ratio rods can be synthesized, which still preserve regular shapes and show no tendency to aggregate, all features that are not achievable with lower-temperature shell-growth approaches. A key issue of this type of approach is whether the original seed is preserved in the final rod structure and also which is the location of the seed along the rod.[17]
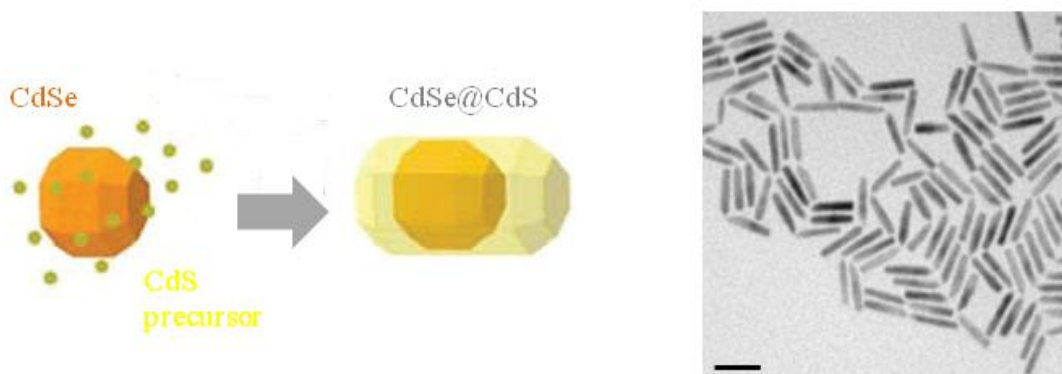
Fig.1.5 Sketch of the seeded growth approach applied for the synthesis of CdSe@CdS dot@rod (left) and TEM images of CdSe@CdS dot@rods (right). Scale bar is 20 nm.

While the synthesis of CdSe@CdS dot@rods is by now well rationalized, the mechanism underlying the formation of the CdSe@CdS octapods is currently investigated.

Recently, a complex synthesis leading to CdSe@CdS dot@octapods consisting of a central CdSe core and eight CdS "pods" departing from it has been developed by Manna and coworkers.[18] The key aspect of this synthesis is that the growth of a more symmetric branched morphology requires a CdSe seed in the cubic polymorph, which is highly unfavoured. A Cu/Cd cation exchange of the $Cu_{2-x}Se$ core having cubic berzelianite structure in CdSe allows to overcome this obstacle (Fig.1.6).

The synthetic process to fabricate CdSe@CdS octapod NCs proceeds therefore via seeded growth starting from $Cu_{2-x}Se$ nanocrystals in the cubic phase, which are obtained by reaction at 300°C under inert atmosphere between a solution of CuCl and oleylamine in 1-octadecene and a Se precursor solution prepared by dissolving Se in oleylamine. The resulting $Cu_{2-x}Se$ nanocrystals were purified, dispersed in TOP and mixed with a suspension of S in TOP, then injected at 380 °C in a mixture containing CdO, $CdCl_2$, ODPA, HPA, TOPO and TOP. After the injection, the reaction is run for a given growth time (typically 10 min) and then the solution cooled to room temperature. The resulting product is purified by repeated washings with toluene and methanol and finally dispersed in toluene.
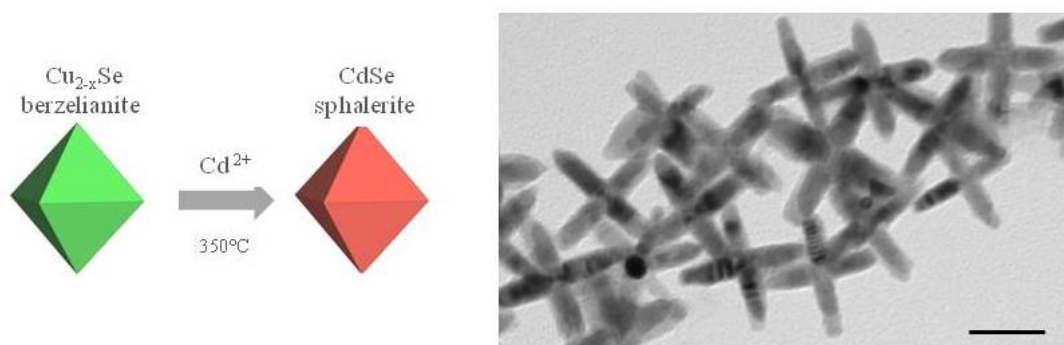
Fig.1.6 Sketch of the seeded growth approach applied for the synthesis of CdSe@CdS dot@octapods (left) and TEM images of CdSe@CdS dot@octapods (right). Scale bar is 50 nm.

As pointed out by Figure 1.6, cation exchange is a key step in the successful formation of CdSe@CdS octapods. Due to its potential relevance in nanocrystal design, cation exchange has been the subject of recent research in which it has been demonstrated that $Cu_{2-x}Se/CdSe$ conversion is reversible and occurs without altering the shape of the nanocrystals. [19]

In this work, the microstructural features of CdSe@CdS rods and octapods were investigated and compared. In addition, the different reactivity of the different crystal facets exposed by

the NCs with different shape were exploited to selectively deposit catalytically active metal tips.

1.1.2 Optical properties of semiconductor nanocrystals

Semiconductor nanocrystals exhibit peculiar optical properties compared to bulk semiconductors, as a consequence of their electronic structure described in Paragraph 1.1.1. In a semiconductor nanocrystal, a bound electron-hole pair, called an *exciton,* can be produced by a photon having an energy greater than that of the band gap of the material (Fig. 1.7). The photon excites an electron from the filled band to the unfilled band above. The result is a hole in the otherwise filled valence band, which corresponds to an electron with an effective positive charge. Because of the Coulomb attraction between the positive hole and the negative electron, the exciton is formed that can move through the lattice, the separation between the hole and the electron being many lattice parameters. [20]
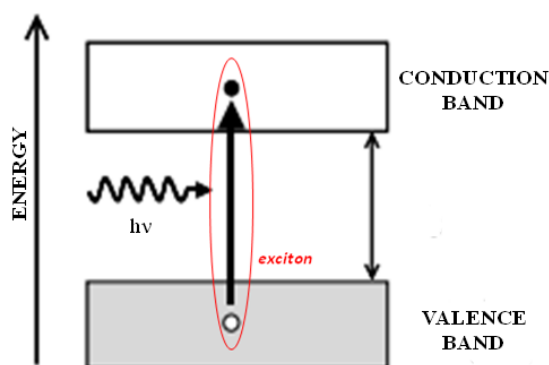
Fig. 1.7 Exciton formation in quantum dots

The existence of the exciton has a strong influence on the optical properties of a semiconductor; the characteristic effects of quantum confinement can be in fact observed in the optical absorption and emission spectra of semiconductor nanoparticles. Indeed, in a nanocrystalline semiconductor, the phenomenon of optical absorption reflects the nature of the electronic levels. In fact, the absorption spectrum appears composed of a series of partially overlapping peaks corresponding to different energy levels (Fig. 1.2.a) and covers hundreds of nanometers. The presence of these peaks is related to parameters such as dispersion in size of the sample investigated and temperature fluctuations.

Likewise, emission spectra are influenced by the size of the nanocrystals. In fact, when excited, semiconductor nanocrystals emit with a narrow and symmetric emission peak because of the radiative recombination of the electron-hole pairs.[14] More energy is then needed to excite the nanoparticle and more energy is released when the crystal returns to its ground state, resulting in a colour shift from red to blue in the emitted light. As a result of this phenomenon, semiconductor nanocrystals can emit any colour of light from the same material simply by modifying its diameter (Fig 1.8).

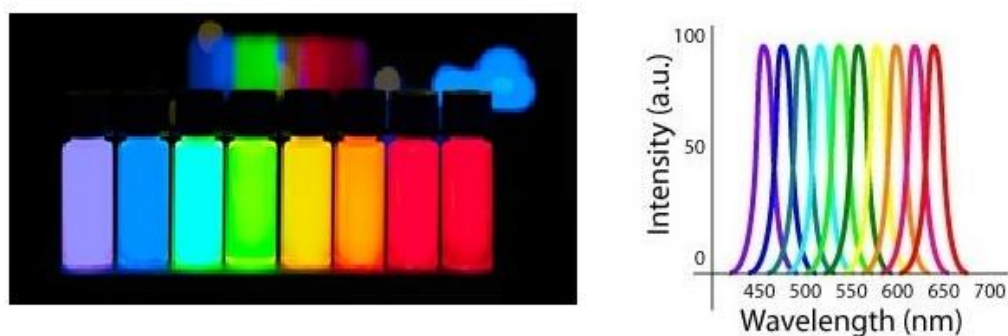*Fig. 1.8 a) QDs with emission maxima in a 10-nm step are being produced at PlasmaChem in a kg scale; b) Photoluminescence spectra at different wavelengths; the smaller its size is in a semiconductor nanocrystal, the more its optical emission is shifted towards the blue, that is toward higher energies.*

The photoluminescence properties of the nanocrystals depend on a variety of parameters that do not affect the absorption properties. These ones depend mainly on the surface structure and on the chemical environment around the nanocrystal. Since nanocrystals have a large surface-to-volume ratio, their optical, electronic and chemical properties are strongly affected by the chemistry on their surface. For this reason, a well-passivated surface in a sample of monodisperse nanocrystals leads to a band edge emission characterized by high quantum efficiency and narrow emission line width.[21] This suggest that, in the absence of defects, internal or surface-related, a nanocrystal should exhibit near unity fluorescence quantum yield, even if this is clearly not true because many defects, and in general many non-radiative channels, are active, thus reducing considerably the efficiency of the radiative recombination process. High luminescence efficiency is therefore ascribed to the growth of nanocrystals with few lattice defects.

Furthermore, the photoluminescence lifetime of semiconductor nanocrystals is longer compared to that in the corresponding bulk material, allowing one to increase the collection of photons, which increases enormously the signal to noise ratio. [22]

Thus, nanocrystals can be better photoemitters than bulk semiconductors because, in the former, electrons and holes are strongly confined, hence there is a considerable overlap of their wavefunctions.

1.1.3 Energy applications of semiconductor nanoparticles

The optical behaviour of the semiconductor nanoparticles and nanostructures can be strategically exploited in energy field. Efficient transfer of charges across the semiconductor interface is the key for converting light energy into electricity or fuels. Of particular interest is in fact, the role of semiconducting NCs in capturing incident photons to induce charge separation in nanometric solar cells and in photocatalyst systems, that make them promising building blocks in light harvesting systems.

In particular, chalcogenide semiconductor nanocrystals have been widely investigated for the development of quantum dot-sensitized solar cells as a cheaper alternative to conventional silicon based solar cells. [23]

Concerning the use of semiconductor nanocrystals as photocatalysts, titanium dioxide with particular reference to the anatase polymorph have been extensively used in a wide range of reactions. [24]

A specific application of semiconductor nanocrystals which has a major relevance for its implications in energy and environment, is related to the production of hydrogen through the so-called *water splitting reaction*.

Photocatalytic water splitting is an artificial photosynthesis process used for the dissociation of water into hydrogen (H_2) and oxygen (O_2), using either artificial or natural light, which can provide a clean, renewable energy, without having many adverse effects on the atmosphere.

Photocatalytic water splitting reaction is shown below:

$$2\,h\nu + semiconductor \rightarrow 2h^+ + 2e^-$$
$$2h^+ + H_2O \rightarrow \frac{1}{2}O_2 + 2H^+$$
$$2H^+ + 2e^- \rightarrow H_2$$
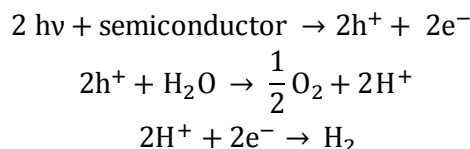
The process is highly endothermic ($\Delta H > 0$) and occurs naturally in photosynthesis when photon energy is absorbed and converted into the chemical energy through a complex biological pathway. However, production of hydrogen from water requires large amounts of input energy, making it incompatible with existing energy generation. There are several strict requirements for a photocatalyst to be useful for water splitting. The minimum band gap for successful water splitting at pH=0 is 1.23 eV, corresponding to light of 1008 nm, the electrochemical requirements can theoretically reach down into infrared light, albeit with negligible catalytic activity.

Additional parameters which should be taken into account in photocatalytic water splitting are that potential must be less than 3.0 V to make efficient use of the energy present across the full spectrum of sunlight; that water splitting can transfer charges, but not be able to avoid corrosion for long term stability; and finally that surface phenomena as defects within crystalline photocatalysts can act as traps, that is potential recombination sites, ultimately lowering the efficiency.

A typical example of semiconductor with the proper band structure is titanium dioxide (TiO_2) which has been the subject of extensive investigation for last three decades. [25]

However, due to the relatively positive conduction band of TiO_2, there is little driving force for H_2 production, so TiO_2 is typically used with a co-catalyst and metal (such as platinum and gold) -titania catalysts have been proposed to increase the rate of H_2 production. [26]

More recently, another class of photocatalysts based on metal chalcogenide (CdS, CdSe, PbS, PbSe), have been proposed for H_2 production through water splitting, due to a significant advantage related to their tunable response to visible light. In order to absorb visible light, it is necessary to narrow the band gap. Since the conduction band is fairly close to the reference potential for H_2 formation, it is preferable to alter the valence band to move it closer to the potential for O_2 formation, since there is a greater natural overpotential. As in the case of TiO_2, a possible way to boost the efficiency of photocatalytic reaction is to add co-catalysts to drive H_2 evolution in most photocatalysts due to the conduction band placement.

Photocatalysts can suffer from catalyst decay and recombination under operating conditions. In particular, catalyst decay becomes a problem when using a sulfide-based photocatalyst is combined to sacrificial reagents able to replenish any sulfur loss. [27]

A mentioned earlier, recombination of the electron-hole pairs needed for photocatalysis can occur with any catalyst and is dependent on the defects and surface area of the catalyst; thus, a high degree of crystallinity is required to avoid recombination at the defects. A successful class of novel photocatalysts for the water splitting reaction is represented by CdSe@CdS elongated nanocrystals with rod shape combined with Pt nanocrystals which are obtained with high crystallinity through colloidal techniques. It should be emphasized that conversion

of solar energy to hydrogen by means of photocatalysis is one of the most interesting ways to achieve clean and renewable energy systems.

For this reason, in this research work we have addressed the design, synthesis and characterization of metal-semiconductor nanocrystals for potential use in photocatalytic water splitting. In particular, whereas most of the photocatalytic studies focus on the net photoconversion efficiency, understanding of various electron-transfer steps at the fundamental level is still lacking. The manipulation of interfacial charge transfer is the most important factor that can assist in improving the photocatalytic and solar cell conversion efficiency. The data presented in this work aim to contribute to a better understanding of the charge-transfer dynamics between semiconductor and cocatalyst needed to improve the photocatalyst design.

1.2 Magnetic nanoparticles and their properties

1.2.1 Basic principles of magnetism (with reference to the nanoscale)

Magnetic particles are a class of materials which respond to an externally applied magnetic field; they have been the focus of much research recently because they possess attractive properties which could see potential use in catalysis, biomedicine, magnetic resonance imaging, nanofluids, sensors and optical filters. [28]

In the following, some of the main features of magnetic properties which are more relevant to the application of magnetic nanoparticles (MNPS) to biomedicine, with particular reference to hypertermia treatment and on magnetic resonance imaging, will be summarized.

The origin of magnetic properties in matter lies in the orbital and spin motions of electrons around the nucleus of a free atom, whose spin and angular momentum are associated with a magnetic moment; whereas contributions, like those ones related to the nuclear magnetic moment, are generally negligible.

When a material is exposed to a magnetic field of strength H, the individual atomic moments in the material contribute to its overall response, known as magnetic induction B:

$$B = \mu_0(H + M)$$

where μ_0 is the vacuum permeability ($4\pi \cdot 10^{-7}$ H/m) and M the magnetization, which can be expressed as magnetic moment m per unit volume V of the material. [29]

We can classify magnetic materials in terms of their volumic magnetic susceptibility (χ), which describes the magnetization degree of the material in response to an applied magnetic field, so that $M = \chi H$.

Magnetic behaviours can be classified into five main types; ferromagnetic, paramagnetic, antiferromagnetic, ferrimagnetic (Fig.1.9) and diamagnetic. [29]

In *ferromagnetic* materials (such as iron, nickel and cobalt) atoms have unfilled inner energy levels in which the spins of the electrons are unpaired, giving the atom a net magnetic moment. This class of material is composed of domains each containing large numbers of atoms wherein magnetic moments are parallel, producing a net magnetic moment of the domain that points in some direction. The magnetic moments of the domains are randomly distributed giving a zero net magnetic moment of the material. When the ferromagnetic material is placed in a magnetic field, the magnetic moments of the domains align along the direction of the applied magnetic field forming a large net magnetic moment. However, a residual magnetic moment exists even after the magnetic field is removed.

In *paramagnetic* materials (such as gadolinium, magnesium, lithium and tantalum) an atom has a net magnetic moment due to unpaired electrons' spins but magnetic domains are absent. When the paramagnetic material is placed in a magnetic field, the magnetic moments of the atoms align along the direction of the applied magnetic field forming a weak net magnetic moment. These materials do not retain magnetic moment when the magnetic field is removed.

In *diamagnetic* materials (such as copper, silver, gold and most of the known elements) atoms have no unpaired electrons' spin which results in zero net magnetic moment. These materials display a very weak response against the applied magnetic field due to realignment of the electron orbits when a magnetic field is applied. They do not retain magnetic moment when the magnetic field is removed.

Antiferromagnetic materials (such as MnO, CoO, NiO and $CuCl_2$) are compounds of two different atoms that occupy different lattice positions. The two atoms have magnetic moments that are equal in magnitude and opposite in direction which results in zero net magnetic moment.

Ferrimagnetic materials (such as magnetite Fe_3O_4 and maghemite γ-Fe_2O_3) are also compounds of different atoms residing on different lattice sites with antiparallel magnetic moments. However, in these materials, the magnetic moments do not cancel out since they have different magnitudes which results in a net spontaneous magnetic moment. When placed in a magnetic field, antiferromagnetic and ferrimagnetic materials show a behaviour similar to that of ferromagnetic ones.
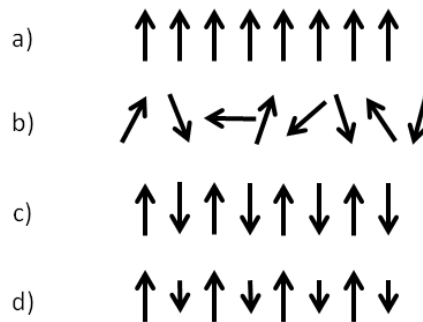

Fig 1.9: From top to bottom: a) ferromagnetism, b) paramagnetism, c) antiferromagnetism, d) ferrimagnetism.

The values of susceptibility in ordered materials allow to distinguish magnetic behavior of materials and different response subject to an external magnetic field H. Diamagnetic and paramagnetic materials show little magnetism and even then only in the presence of an applied field. The susceptibility χ falls in the range 10^{-6} to 10^{-1} for paramagnetic materials and in the range -10^{-6} to -10^{-3} for diamagnetic materials. The opposite verse of magnetization with respect to the external magnetic field H determines the negative sign of susceptibility for diamagnetic materials; instead, in ferro- and ferrimagnetic materials χ depends not only on the temperature, but also on the external magnetic field H, which gives rise to the typical hysteretic behaviour, which is commonly pointed out by measuring M while cycling the field between two large positive and negative field values. The coupling of magnetic moments can give rise to large spontaneous magnetization. [28] In case of antiferromagnetic materials the antiparallel coupling of magnetic moments with equal magnitude gives rise to a net magnetization of zero.

As previously mentioned, the magnetic structure of macroscopic magnetic materials breaks into small regions, called magnetic domains which are the result of balance of several energy

terms: the exchange energy, magnetocrystalline anisotropy and the magnetostatic (or dipolar) energy.

The *exchange energy*, which has quantum mechanical origin and is responsible for spin alignment in ordered structures, promoting the ferromagnetic or antiferromagnetic order. These kind of interactions come from the overlap between atomic or molecular orbitals and are related to the exchange energy between electrons. The exchange interactions can be roughly divided in two main classes: the direct exchange, when the orbitals of atoms carrying the magnetic moment directly overlap, and super exchange, when the interaction between two magnetic centres is mediated by a diamagnetic atom.

The *magnetocrystalline anisotropy energy* tries to orient magnetic moments along specific directions. In fact, it is a well known experimental fact that some crystals can be more easily magnetized in certain directions, called easy axes of magnetization, than in others. This is an intrinsic property of the material related to crystal symmetry and to atom arrangement in the crystal lattice. The origin of this contribution arises from the fact that orbital wave function reflects the symmetry of the lattice and this influences the spins through spin-orbit coupling.

The *magnetic dipole interaction energy* arises from dipolar interactions of magnetic moments. These interactions are weak compared to the exchange energy, but in some materials they are the only forces acting between moments and can induce magnetic order at very low temperature.

Within a single domain all magnetic moments are parallel. In the absence of an external magnetic field and any other constraint, the volume of the different domains is equally distributed along all the directions, resulting in a total magnetization equal to zero at the macroscopic scale.

The boundary between two neighbouring domains is a domain wall so-called Bloch's walls, which consists of few atomic planes of 100-200 nm in size in which the magnetic moment orientation change gradually from a domain to another one (Fig.1.10).
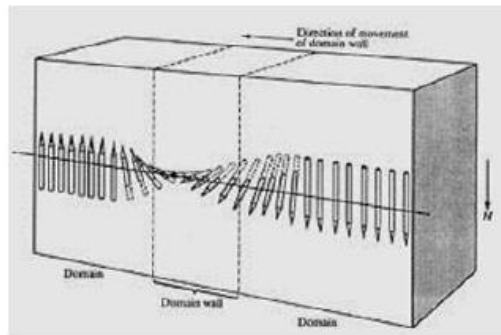
Fig 1.10 Magnetic moment arrangement in domains and domain wall (Bloch walls)

In a schematic representation of a ferromagnetic material, a Bloch wall will stand between two domains in which the magnetization is oriented in two opposite directions. Under the action of an external magnetic field, the walls will move causing the growth of the domain whose moments are oriented parallel to the field or in a more favourable direction, while reducing the other. As a result, the material will show a net magnetization M, parallel to H. Expansions and contractions of domains are reversible only for small values of field, while for higher ones irreversibility occurs, due to the interactions between the magnetic moments and the material structure. As a consequence, the material shows field irreversibility: the *magnetization*, from 0 to H_{MAX}, and the *demagnetization*, from H_{MAX} to 0.

Fig.1.11 Typical hysteresis loop of a ferromagnetic material

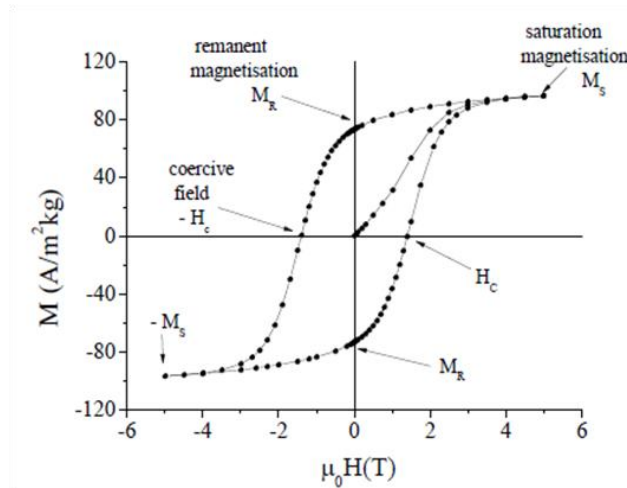In detail, when a ferro- or ferrimagnetic material is placed in a sufficiently large external field, the spins in each domain progressively rotate parallel to the direction of the applied magnetic field, reaching the saturation magnetization M_s. When the applied field is decreased, the magnetization decreases but the demagnetization curve during the removal of the applied field does not follow the initial magnetization curve and the material displays hysteresis, as shown in Figure 1.11.[30] *Remanent magnetization* (M_R) is the magnetization remaining at zero applied field after complete saturation. The magnetic field applied in the negative direction required to return the magnetization to zero is the *coercive field* (H_C). M_s, M_R and H_c are important parameters to estimate the magnetic properties of a material; indeed, the curve of the magnetization of a material versus the applied magnetic field is a typical measurement performed to characterize the magnetic behaviour of a ferro- or ferrimagnetic material.

In comparison to a homogeneously magnetized object, the formation of magnetic domains materials occurs in order to minimize the magnetostatic energy of the system proportional to the sample volume. However, a certain amount of energy is required for the creation of the domain wall, which is proportional to the domain interface. If the particle size is reduced, there is a critical volume below which it costs more energy to create a domain wall than to support the external magnetostatic energy (stray field). Under this critical diameter (d_c) the particle will consist of a single domain. [31]

Most of common magnetic materials have a d_c below 100 nm (14 nm for Fe, 128 nm for Fe_3O_4, 50 nm for $MnFe_2O_4$).

In *a single-domain particle*, all the spins are aligned in the same direction and the particle is uniformly magnetized. Because there are no domain walls to move, the inversion of the magnetization is no more caused by the movement of Bloch walls, but through the coherent rotation of all the spins in the single particle, resulting in large coercivity of the nanoparticles. In this case, the magnetic properties can then be described by *a total magnetic moment μ* obtained by the vectorial sum of the single atomic spins, that can be defined as

$$\mu = M_S \cdot V$$

where M_S is the saturation magnetization and V the average nanoparticles volume.

As already discussed, the magnetic material are anisotropic, as the magnetization tends to lay along favourite directions, the easy axis. There are different factors that contribute to the whole magnetic anisotropy: some of them are common to both bulk and nanostructured

materials, while others ones become significant only after the reduction of the material to the nanoscale.

• Magnetocrystalline anisotropy: as earlier discussed, this contribution arises from the influence of lattice symmetry on spins, through the spin-orbit coupling, and it is an intrinsic property of the material.

• Shape anisotropy: it is related to the magnetostatic energy. The presence of free magnetic poles on the surface of a magnetized object causes a magnetic field around the material called demagnetizing field, which is responsible for the magnetostatic energy. When the magnetic moment of the particle rotates, these poles move on the surface. Therefore, the particles shape establishes the amount of magnetostatic energy as a function of the magnetization orientation. A change in the spherical shape induce shape anisotropy that can compete with the magnetocrystalline contribution.

• Surface anisotropy: the origin of this contribution is due to the lower symmetry of the surface atoms with respect to the internal ones. For this reason, it is very sensitive to the chemical surrounding and can be influenced by the chemical species bound to the surface. The magnitude of this contribution increases on decreasing the size of particle, due to the increase surface to volume ratio. Stress anisotropy: it is related to magnetostriction, i.e. a change of length in the magnetization direction, due to the spin-orbit coupling. The mechanic strain is related to any kind of stress that can act on the system, then anisotropy can depend on the stress state.

• Exchange and dipolar anisotropy between particles: when two particles will magnetically interact and this interaction can be related both to the magnetic dipole and the exchange interactions, leading to another contribution to the total anisotropy. The whole anisotropy constant observed will then depend on the relative magnitude of each contribution, which depends on material structure, shape and size.

The magnetic moment per atom and the magnetic anisotropy of materials on the nanoscale can be different than those of a bulk material; in fact, as the size of the particle decreases, the ratio of the surface area to the volume of the particle increases. For nanoparticles, this ratio becomes significantly large causing a large fraction of the atoms to reside on the surface compared to those in the core of the particle and consequently with respect to the bulk ones. Also, when the size of magnetic materials are reduced to the nanoscale, the total magnetic anisotropy can be often assumed, as a first approximation, to be uniaxial, i.e. there is only one fixed direction which is largely energetically favoured with respect to all the others.[32]

In this case, the anisotropy energy will be described by the following equation:

$$E_a(\theta) = K_{eff} \cdot V \cdot sin^2\theta$$

where V is the nanoparticles' volume, k_{eff} the effective anisotropy constant and θ is the angle between the magnetic moment and the easy axis of the particle (Fig.1.12). From this equation it emerges that there are two energy minima corresponding to θ=0 e θ=π, separated by an energy barrier $\Delta E = K_{eff} \cdot V$.[32]

This is the energy which separates the two energetically equivalent easy magnetization directions i.e., the energy barrier to moment reversal (the size of this energy depends on many factors including magneto crystalline and shape anisotropies).
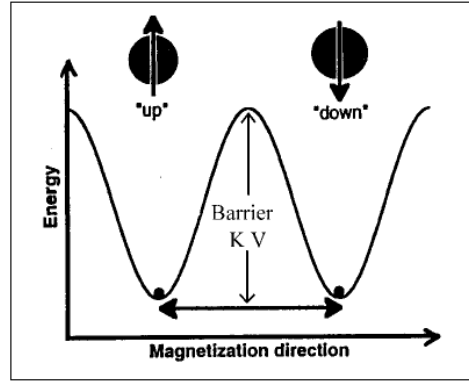
Fig. 1.12 Energy diagram of a particle with uniaxial anisotropy as a function of the angle between the magnetization vector and the easy axis

The magnetic behaviour of nanoparticles can be analyzed both as function of temperature and magnetic field. In the absence of an applied magnetic field, when the thermal energy is much lower than energy barrier ($K_BT<\Delta E$), the probability that the magnetization vector forms an angle θ with the easy axis has a finite value only in correspondence of the two minima, so that the magnetization is "blocked" aligned to the easy axis. On increasing temperature, the allowed θ values will have a broader distribution around the two minima and this causes the particle magnetization to oscillate freely around the direction of the easy axis. The temperature at which this spin flipping occurs is called the *blocking temperature, T_B* that depends on the particle size and other factors.

When the thermal energy is larger than the magnetic one ($K_BT>\Delta E$), the magnetization can freely flip from a minimum to the other one without constraints. In this state, the magnetic moment of the particle behaves as that of a single atom (like a paramagnet). The main difference from a paramagnetic system is that the magnetic moment value is much higher, because it corresponds to the sum of 10^2-10^5 spins. For this reason this state is called *superparamagnetic state*.

In the superparamagnetic state, the magnetic moments of the nanoparticles fluctuate around the easy axes of magnetization. Thus each one of the magnetic nanoparticles will possess a large magnetic moment that continuously changes orientation. When a magnetic field is applied, MNPs in the superparamagnetic state display a fast response to the changes of the magnetic field without remanent magnetization and without coercivity (the magnetic field required to bring the magnetization back to zero). Thus, in the superparamagnetic state, a MNP behaves as a paramagnetic atom with a giant spin. At temperatures below the blocking temperature, the thermal agitation becomes small and will not be able to cause fluctuations in the orientations of the magnetic moments of the nanoparticles where they freeze in random orientations. [33]

The first description of superparamagnetic relaxation is reported by Néel in 1949; considering a single uniaxial particle, with all the spins aligned along the easy axis and with the inversion of the magnetization due only to a coherent rotation of all the spins in the particles, Néel predicted that the *relaxation time* of the moment of a particle τ_N should follow an Arrhenius law:

$$\tau_N \propto e^{\frac{\Delta E}{K_B \cdot T}}$$

where *ΔE* is the barrier energy tied to the anisotropy and $K_B.T$ is the thermal energy.
If the time window of the measurement (τ_m) is longer than the time needed for the particle's magnetic moment to flip, the particle is said to be in a superparamagnetic state.

On the other hand, if the experimental time scale is shorter than the moment flipping time, the particle is said to be in the blocked state. The blocking temperature, defined as the mid-point between these two states, where $\tau_N = \tau_m$ depends on several factors: the size of the particles, the effective anisotropy constant, K_{eff}, the applied magnetic field, the experimental measurement time.

The second mechanism of electronic relaxation is the Brownian relaxation mechanism which involves the rotation of the particle itself against viscous forces. The time constant, characterizing this motion also increases with the particle volume, however, at a slower rate than the Néel relaxation time constant according to the following equation:

$$\tau_B = \frac{3 \cdot V \cdot \eta}{K_B \cdot T}$$

where η is the viscosity of the liquid containing the particles.

The *total magnetic relaxation time* is then given by

$$\tau_{eff} = \frac{\tau_N \cdot \tau_B}{\tau_N + \tau_B}$$

It can be seen that if $\tau_B < \tau_N$ (as for large nanoaprticle with radius > 15 nm), then it is the viscous component which dominates magnetic relaxation.

In this work the study of superparamagnetic clustered materials based on iron oxide, interesting for their potential implication in biomedical applications, with particular reference on MRI and magnetic hyperthermia, is presented. The aim of the study is to understand the correlation between magnetic properties and chemical composition and to investigate how magnetism influences the potential use of these nanoparticles in these two biomedical fields.

1.2.2 Spinel ferrite nanocrystals and their magnetic properties

Ferrites are metal oxides with the crystalline structure of the spinel. The unit cell of ferrite spinel structure (with lattice parameter value, d ~0.84 nm) is formed by 32 O^{2-} anions and 24 cations (Fe^{2+}, Zn^{2+}, Co^{2+}, Mn^{2+}, Ni^{2+}, Mg^{2+}, Fe^{3+}, Gd^{3+}). There are 96 possible positions for cations in the unit cell (64 tetrahedral and 32 octahedral positions). The octahedral sites are larger than the tetrahedral sites. Only 8 tetrahedral positions and 16 octahedral positions are occupied by cations (divalent or trivalent). [34]

The spinel $(A)[B_2]O_4$ structure can be generally described as a cubic closed-packing of oxygen ions. In this structure, the round brackets represent the tetrahedral interstitial (A) sites and the square brackets represent the larger octahedral interstitial [B] sites. Both the tetrahedral and octahedral interstitial lattice sites are occupied by cations. When all the divalent cations occupy the tetrahedral sites while all the trivalent cations occupy the octahedral sites, the structure is called *the normal spinel structure* of the form $(A)[B_2]O_4$. When all the divalent cations occupy the octahedral sites while half of the trivalent cations occupy the tetrahedral sites and the other half occupy the octahedral sites, the structure is called *the inverse spinel structure* of the form $(B)[AB]O_4$.

The general structure of the ferrites spinel structure can be written as $(M^{2+})[Fe^{3+}_2]O_4$, where M^{2+} represent divalent metals ions such Fe^{2+}, Zn^{2+}, Co^{2+}, Mn^{2+}, Ni^{2+}, Mg^{2+} and the Fe^{3+} cations serve as the trivalent ions. In the spinel structure of ferrites (Fig.1.12), the Fe^{3+} atoms occupy the octahedral positions while M^{2+} occupy tetrahedral positions.
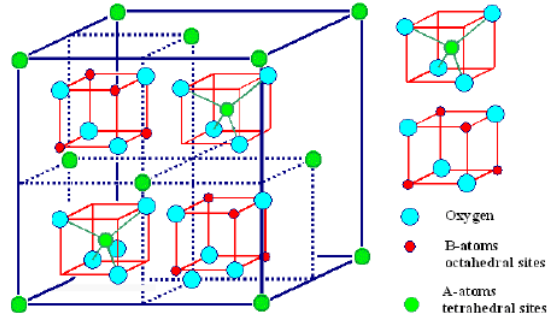
Fig.1.12 AB_2O_4 spinel structure; the Fe^{3+} atoms (red spheres) occupy the octahedral positions while M^{2+} (green spheres) occupy tetrahedral positions.

In some situations, the ferrite structure might have a structure that is in between the normal and inverse spinel structures. Hence, in general, the formula of the ferrite spinel can be written as $(M^{2+}_{1-x}Fe^{3+}_x)\,[M^{2+}_x Fe^{3+}_{2-x}]O_4$. The variable x is called the *degree of inversion* and represents the proportion of Fe^{3+} occupying the tetrahedral sites. When x=0, we obtain $(M^{2+})[Fe^{3+}_2]O_4$, which is the normal spinel structure. When x=1, we obtain $(Fe^{3+})[Me^{2+}Fe^{3+}]O^4$, which is the inverse spinel structure. The magnetic properties of the spinel ferrite materials originate from the antiferromagnetic coupling between the octahedral and tetrahedral sublattices.

In spinel ferrites, all the cations at the octahedral lattice sites have magnetic moments which are oriented in the same direction. At the same time, all the cations on the tetrahedral lattice sites have magnetic moments which are oriented in the same direction but antiparallel to that of the cations at the octahedral lattice sites.[35] The net magnetization of the spinel ferrites is due to the difference in the magnetic moments of the cations at the octahedral lattice sites and those at the tetrahedral lattice sites. [36] In the bulk material, the majority of divalent cations (Fe^{2+}, Co^{2+}, Ni^{2+}, Cu^{2+}, Mg^{2+}) prefers incorporation at the larger octahedral lattices sites. In contrast Mn^{2+} divalent ion, displays preference to occupy the tetrahedral A-sites. In pure $MnFe_2O_4$ ceramics, approximately 80% of manganese enters the spinel structure at tetrahedral sites and 20% at octahedral sites: $(Mn_{0.8}Fe_{0.2})\,[Mn_{0.8}Fe_{0.2}]O_4$.[37]

The most important member of the family of ferrites is by no doubts magnetite (Fe_3O_4). It has been employed in a large number of applications and, still today, it is the most used and investigated magnetic material. Fe^{2+} in magnetite can be partly or fully replaced by other divalent ions (i.e. Co, Zn, Mn). Fitting of guest ions into the structure is allowed by the flexibility of the oxygen framework, which can expand or contract to accommodate cations with different size. Cation substitution is accompanied by changes in unit cell edge length. [38]

Since the peculiar properties of ferrites are strictly related to the distribution of cations between octahedral and tetrahedral sites in the spinel structure, the control of cation distribution provides a mean to tailor their properties. Therefore, there is a particular interest in studying the cation distribution in ferrites, which, in turn, depends on the electronic configuration and valence of the considered ion. Some studies show that also the particle size can influence the cation distribution, especially at the scale of the nanometers.

Ferrites are generally ferrimagnetic. By adjusting the chemical identity of M^{2+}, the magnetic configurations of MFe_2O_4 can be molecularly engineered to provide a wide range of magnetic properties. Due in part to this versatility, nanometric scale MFe_2O_4 materials have been among the most frequently chosen systems for studies of nanomagnetism and have shown great potential for many important technological application.[39]

1.2.3 Biomedical applications of magnetic nanoparticles

Magnetic nanoparticles are of great interest for a wide range of disciplines; with particular reference in medical field, they are used as contrast agents to enhance the contrast in MRI [40]; in tumour therapy, where they can be selectively introduced into the tumour cells and then their temperature is increased using an oscillating magnetic field to reach near 43°C, temperature known to make the tumour cells more sensitive to radiation and other treatment modalities [41]; and finally used as site-specific drug delivery agents which involves immobilizing the drug on magnetic materials under the action of external magnetic field.

For biomedical applications, several properties of nanoparticles must be attained; in particular, in vivo applications require magnetic nanoparticle to be biocompatible, stable, nontoxic and monodispersed, which requires controlling particle material, size and coating properties. [42]

Moreover, high saturation magnetization is an important requirement because both the movement of the particles in the blood can be controlled with a moderate external magnetic field, and the particles can be moved close to the targeted pathologic tissue.

The magnetic nanoparticles which are used in biomedical applications are mainly iron oxide particles such as magnetite (Fe_3O_4) and its oxidized product, tetragonal maghemite (γ-Fe_2O_3). These natural materials are found in many biological systems. [43]

Instead, metallic magnetic materials such as iron, cobalt and nickel are toxic, and susceptible to oxidation.

The next paragraphs will provide some background on two biomedical implications, in which the nanocrystal clusters based on iron oxide, synthesized in our laboratory, have found potential application: magnetic resonance imaging (MRI) and magnetic hyperthermia.

- Contrast agents for MRI

Magnetic resonance imaging is one of the most important non-invasive imaging methodology nowadays available in clinical medicine for the diagnosis of diseases. Its advantages includes excellent soft tissue contrasts, high depth of penetration and high spatial resolution (under specific condition imaging at cell resolution is achieved). A major advantage is that it is considered safe, since the used frequencies (typically 40-130 MHz) are in the radiofrequency range, and there are no associated adverse health effects. The MR signal is sensitive to a broad range of influences, such as nuclear mobility, molecular structure, flow and diffusion.

The main disadvantage, however, is the intrinsically low sensitivity. As a result, large doses of contrast agents are typically administrated to increase the sensitivity of MRI.

The basis of MRI is the directional magnetic field, or moment, associated with charged particles in motion. Nuclei containing an odd number of protons and/or neutrons have a characteristic motion or precession. Because nuclei are charged particles, this precession produces a small magnetic moment.

When a human body is placed in a large magnetic field, many of the free hydrogen nuclei align themselves with the direction of the magnetic field. The nuclei precess about the magnetic field direction; this behaviour is termed Larmor precession. The frequency of Larmor precession is proportional to the applied magnetic field strength H_0 as defined by the Larmor frequency ω_0:

$$\omega_0 = \gamma \cdot H_0$$

where γ is the gyromagnetic ratio. The gyromagnetic ratio is a nuclei specific constant; for hydrogen, its value is 42.6 MHz/Tesla. [44]

To obtain an MR image of an object, the object is placed in a uniform magnetic field, between 0.5 to 1.5 Tesla. As a result, the object's hydrogen nuclei align with the magnetic field and create a net magnetic moment, M, parallel to H_0. Next, a radio-frequency (RF) pulse, is applied perpendicular to H_0. This pulse, with a frequency equal to the Larmor frequency, causes M to tilt away from H_0. Once the RF signal is removed, the excited nuclei relax to achieve the initial equilibrium state.

This return to equilibrium is referred to as *relaxation*. During relaxation, the nuclei lose energy by emitting their own radio signal. This is detected using antennas (coils) and can be processed or *reconstructed* to obtain 3D grey-scale MR images of body tissues.

MR image contrast depends on two tissue-specific parameters: *the longitudinal relaxation time, T_1* and *the transverse relaxation time, T_2* (Fig.1.13). The first one, T_1 measures the time required for the magnetic moment of the displaced nuclei to return to equilibrium, realigning itself with H_0 and reflects a exchange of energy between the system to its surrounding "lattice"; the transverse relaxation T_2 is driven by the loss of phase in nuclear precession after the electromagnetic field is removed.
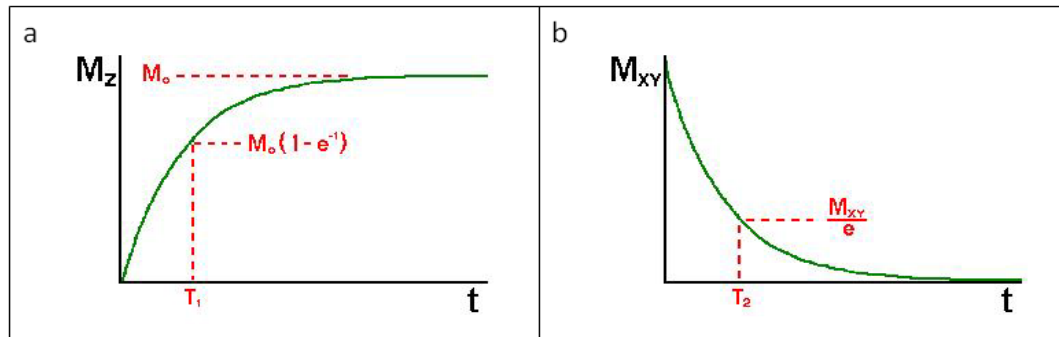

Fig 1.13 Trend of longitudinal (a) and transverse (b) magnetization as a function of time. Here have shown the longitudinal relaxation time, T_1 and the transverse relaxation time, T_2 respectively.

The contrast comes from local different density of hydrogen nuclei in different tissues and from local differences in nuclear spin relaxation along the longitudinal and transverse directions. On this basis, endogenous contrast depends on the chemical and physical nature of the tissues and often arises from local variation in the protons density (water concentration). Otherwise, the use of contrast agents that alter the signal intensity by selectively shortening the hydrogen relaxation times T_1 or T_2 of the tissue are essential to improve sensitivity and specificity of MRI.

The contrast agents can be distinguished in positive and negative: positive contrast reduce T_1 resulting in a brighter signal, while negative contrast agents reduce T_2 resulting in a darker signal.

T_1 or T_2 -weighted MR-images are generated based on the rate of longitudinal or transverse relaxation of the water, respectively. The positive contrast agents are based on paramagnetic compounds (the most used are gadolinium ion complexes) whereas the negative ones are generally nanoparticles constituted by superparamagnetic ferrites. [33]

There are two contributions to proton relaxation in paramagnetic systems: the inner- and outer-sphere relaxations. Inner-sphere relaxation deals with the direct chemical exchange of hydrogen nuclei located in the first hydration sphere with hydrogen nuclei of bulk water and is dominated by dipolar and scalar coupling of the spins. Outer-sphere relaxation is due to the movement of the water protons near the local magnetic field gradients generated by the paramagnetic ion. The inner-sphere relaxation is dominant in paramagnetic contrast agent.

For superparamagnetic particles, the inner-sphere contribution to the relaxation is minor and more often completely negligible as compared to the dominant outer-sphere contribution. [45]

The nuclear magnetic relaxation properties of a compound are ideally obtained by the study of its nuclear magnetic resonance dispersion (NMRD) profile. These curves give the relaxivity evolution versus the external magnetic field.

The ability of a contrast agent to enhance the proton relaxation rate is defined in terms of its relaxivity:

$$R_{1,2} = \frac{1}{T_{1,2}} = R_{1,2}^0 + r_{1,2} \cdot C$$

where $R_{1,2}^0$ are the relaxation rates without the presence of the contrast agent, C is the molar concentration of the contrast agent and $r_{1,2}$ are the relaxivity constants ($s^{-1} \cdot mmol^{-1} \cdot L$) of the agent. [45]

The field dependence of the longitudinal relaxation rate (NMRD profile) in aqueous colloidal suspensions of superparamagnetic particles is led by two different physical mechanisms: the Néel relaxation and the Curie relaxation. The Néel relaxation, i.e. the reversal of electronic magnetization that overcomes the energy barrier in a superparamagnet, has influence on the relaxivity behaviour for frequencies below about 1-10 MHz (low fields) through the related magnetic anisotropy. The Curie relaxation accounts essentially for the high frequency (i.e. high field) part of the NMR profiles ($H_0 > 0.05$ Tesla approximately) and is given by the spin-spin correlation function related to the diffusion of nuclei, times the square of the Langevin function, so taking into account the correlation time typical of nuclear spin diffusion "weighted" by the effective electron magnetic moment.

Another important parameter to evaluate the relaxometric properties of a contrast agent is the ratio r_1/r_2. It is used to classify a given type of MRI contrast agent as T_1 or T_2 relaxing. [46]

The efficiency of contrast agent can be enhanced by using materials that have larger magnetic moments such as ferromagnetic particles, mainly iron oxides, or indeed ferrites substituted with elements such as Gd, Mn, Zn, etc. As explained earlier these materials behave as giant paramagnetic spins when their volume is reduced to the nanoscale. Due to their high T_2 relaxivity (relaxation rate per concentration of MNPs) and their biocompatibility, colloidal iron oxide nanoparticles are the most promising superparamagnetic contrast agents and commercial formulations are already available. [47]

Unlike some other medical imaging techniques, MRI does not involve radioactivity or ionising radiation. The frequency used (typically 40÷130 MHz) are in the normal radiofrequency range, and there are no adverse health effects. Very detailed images can be made of soft tissues such as muscle and brain.

The MR signal is sensitive to a broad range of influences, such as nuclear mobility, molecular structure, flow and diffusion.

- Mediators for magnetic hyperthermia

A recent and promising cancer treatment is the clinical hyperthermia, which consists in the rise of the temperature of cancer cells (from 40-41 °C up to 45 °C), in order to weaken or destroy them. Cells subjected to high temperatures undergo to irreversible damage related to the reduction of the efficiency in the restorative systems usually found in cellular ambient (low pH, lack of oxygen and poor vascular nutrition). Tumour tissues are more sensitive to high temperatures than healthy ones, due both on genetic characteristics and the microenvironment in which the cells are placed.

Studies confirmed the hyperthermia efficiency and demonstrated the therapeutical gain from its association with radiotherapy and chemotherapy [48] but even hyperthermia treatment alone may damage tumour tissue. In fact, the hyperthermia treatment allows an increase of perfusion in the tumor tissue and therefore a higher oxygen constant, which makes the γ radiation more powerful in destroying the pathological cells. [49]

More recently, research has focused in positioning heating sources, of size ranging from macroscopic to the nanoscale, into the tumour body (interstitial techniques), so that they can act as mediators converting the electromagnetic energy into heat directly *in situ,* when exposed to an external electromagnetic field. According to the predominant component of the electromagnetic field, electric or magnetic, they are called *capacitive and inductive hyperthermia mediators*, respectively. Specifically, inductive magnetic mediators consist in a heat release by specific inductive mediators, placed in the tumour tissue, during the exposition to an alternate magnetic field of appropriate frequency and amplitude. In this way, heat is confined to the tumour region, saving healthy tissues which, being by nature free of inductive mediators, are transparent to the alternate magnetic field, because the electric component of the field is strongly reduced.

In the last decade, studies are focusing on the use of colloidal solutions of magnetic nanoparticles as their heat generation potential appears beneficial and they provide the opportunity of direct tumour targeting through blood circulation. This approach is called *magnetic fluid hyperthermia* .

The colloidal solutions of magnetic nanoparticles offer several advantages with respect to the macro- and microscopic crystals used in ferromagnetic implants:

- due to the reduced size they can be transported through the blood flow allowing for treating spread cancer and metastasis, as well as reaching small and surgically not addressable tumours;

- their introduction in tissues is potentially less invasive as it does not require a preliminary surgery, which would be feasible only in large and accessible tumours;

- their surface can be easily functionalized by grafting with stealth polymers and specific targeting molecules;

- due to the leaky and disorganized vasculature which characterizes tumour cells, magnetic nanoparticles naturally tend to preferentially accumulate in them;

- the use of an external magnetic field could help in addressing particles to a specific tissue.

The parameter commonly used for reporting the hyperthermic efficiency and used to compare the heating capacity of different magnetic nanoparticles is the *Specific Absorption Rate (SAR),* defined as the energy converted into heat per mass unit (in W/g) :

$$SAR = C \left(\frac{\Delta T}{\Delta t}\right) \cdot \left(\frac{1}{m}\right)$$

where *C* is the sample specific heat capacity, also called specific power loss, *ΔT/Δt* is the increase in temperature with time at a given magnetic nanoparticle mass concentration (*m*).

For classical high frequency irradiation by external antennas, the power deposition patterns lack selectivity. Another major difficulty in electromagnetic regional hyperthermia is the occurrence of local high temperatures ("hot spots") because of the inhomogeneities of electrical permeability and conductivity of the tissue, which cause variation of the SAR.

A better control of the energy is obtained for an irradiation of the tissue doped by a ferrofluid at a low-frequency magnetic wave (100÷400 KHz). For a given superparamagnetic material, the SAR is very precisely determined by the volume ratio of these crystals in the tissue.

Rosensweig theoretically proved a strong relationship between the SAR of this material and its magnetic relaxation

$$SAR = 4.1868 \cdot \pi \cdot \mu_0^2 \cdot \frac{\varphi \cdot M_s^2 \cdot V}{1000 \cdot K \cdot T} \cdot H_0^2 \nu \cdot \frac{2\pi \cdot \nu \pm \tau}{1 + (2\pi \cdot \nu \cdot \tau)^2}$$

where φ is the volume fraction of superparamagnetic material, ν is the frequency of the oscillating magnetic field, H_0 is the magnetic field strength and τ is the relaxation time.

The expression shows that if the irradiation magnetic field is uniform, the SAR only depends upon the nature and volume fraction of the superparamagnetic particles. [45]

Recently, several works in the literature showed that iron oxide nanoparticles of the same type of those used as contrast agents for MRI can produce significant amounts of heat even with small amplitudes of magnetic field (6÷15 kA/m). For magnetite and maghemite nanoparticles reported into the literature, the SAR values range between 10 and 200 W/g, according to the field parameters values used; in particular, it was shown both theoretically and experimentally that for frequencies of the order of few hundreds of kHz the maximum SAR is attained for size in the 15÷20 nm range for magnetite [50], 20÷25 nm for maghemite [51]. Alternatively to iron oxide, several systems have been investigated, mainly focusing on the enhancement of SAR via the magnetic moment. The investigated materials include pure metal as Co, metal alloys as FePt, core@shell systems as Fe_3O_4@Fe, Au@Fe_3O_4, Au@Co and doped ferrites. [52]

It should be pointed out that at present a direct comparison of the heat efficiency of the different NCs presented in the literature is not straight forward. This is due to the fact that standard conditions (experimental setup, magnetic field, frequency and intensity) have still not been defined. In particular, SAR values increase with the strength of the external field. Clinical in vivo studies, however, recommend that exposure to hyperthermia treatments takes place at fields with moderate strength ($H \cdot \nu$ in the range $10^8 \div 10^9$ A·m^{-1}·s^{-1}) and for limited time (~30 min).

Chapter 2

Heterostructures based on semiconducting domains

Recent advances on research in the field of functional nanomaterials have been focused on the design and fabrication of heterostructures, constituted by different nanometric-sized solid-state domains assembled together to form a unique nanosystem.[53] Being formed by domains of at least two materials such as crystalline and amorphous metals, insulators, conductors and semiconductors, or their combinations, heterostructures combine the individual properties of the constituent nanomaterials, and may exhibit advanced properties that can arise independent of the single-component materials. [54]

Within the framework of research on novel functional heterostructures, in this work nanocrystals made out of a semiconducting domain and a metal domain were investigated. In particular, the semiconducting domain is made out of cadmium chalcogenide core@shells with well-defined morphology (rod octapod) and the metal domain is nanocrystalline platinum. The aim of our investigation is to contribute to the controlled preparation of metal-semiconductor heterostructures with a well-defined shape, which are relevant as prospective photocatalysts in energy-related processes.

In particular, CdS-based nanocrystals have been particularly amenable to the realization of heterostructures with different shape, like branched nanocrystals, which appear well suited for realization of complex optoelectronic functions needed in photocatalysis. In fact, the catalytic properties of various types of colloidal nanocrystals have been ascribed to their shape, as their topology may favour multiple step relaxation pathways for optical excitations. Shape effects on the properties of semiconductors are actually quite evident, as discussed in Chapter 1, and result in clearly different optical features of rod- or wire-shaped semiconductor nanocrystals as compared to their dot-shaped analogues. [13]

In addition to shape, microstructural features with particular reference to those related to interfaces (defects, dangling bonds and potential barriers) should be carefully taken into account in the design of prospective photocatalysts, as they may hinder the extraction of photoexcitations and their energy from nanocrystals. A viable strategy to overcome such

limitations relies on the growth of heterostructures with junctions between domains of different materials at the nanometric scale.

In particular, the design of catalysts for efficient photoconversion has turned to semiconducting-noble metal heterostructures, which may prove to be especially valuable for solar water splitting, an application where several interfaces and vectorial charge transport are usually required. To this end, systems like Pt-CdS, PtNi-CdS, and PtCo-CdS where catalytic metals are paired with a semiconductor material within the same structure, have been recently proposed. [55] Doping has been shown to strongly affect the optical properties of semiconductor nanocrystals; furthermore, the storage and discharge properties of metal nanoparticles play an important role in dictating the photocatalytic performance of semiconductor-metal composite nanomaterials. Both electron and hole transfer across the interface with comparable rates are important in maintaining high photocatalytic efficiency and stability of the semiconductor assemblies. [27]

In particular, Alivisatos and coworkers have demonstrated the efficiency of heterostructures made out of core@shell nanorods consisting of a small CdSe quantum dot embedded in a CdS nanorod with a Pt catalyst grown on the tip, are effective catalysts for photocatalytic water splitting. [56]

In this research work, the design of semiconductor-metal heterostructures made out of a semiconductor CdSe@CdS core@shell domain and a platinum metal domain, which are prospective catalysts in the photocatalytic production of hydrogen by the water splitting reaction, have been investigated. In particular, two kind of core@shell chalcogenide nanocrystals, which were prepared by a high temperature colloidal route in the Nanochemistry division at the Italian Institute of Technology (Dr. L. Manna and coworkers) were selected: elongated dot@rods and branched dot@octapods.

Both conventional characterization structural and morphological physico-chemical techniques (X-Ray diffraction-XRD, Transmission Electron Microscopy-TEM) and advanced structural characterization (X-Ray Absorption Spectroscopy-XAFS) carried out in collaboration with Prof. A. Corrias and coworkers (University of Kent, UK), were used to gain a detailed description of the features of the core@shell heterostructures. The main results of this study are summarized in Paragraph 2.1.

The preformed core@shell nanoparticles were then used to prepare CdSe@CdS-Pt heterostructures by high temperature colloidal synthesis (Par. 2.2). In particular, while the metal-rod heterostructures, which have been already reported in the literature and extensively studied, were used to test the synthetic protocol, the octapods decorated with noble Pt metal have been fabricate for the first time in our group. With their branched yet very well-defined geometry, the CdSe@CdS octapods have offered us the opportunity to investigate systematically the synthetic parameters which enable to deposit the Pt tip at the desired site of the semiconductor domain with accuracy at the nanometric scale.

The obtained CdSe@CdS-Pt heterostuctures were explored by a multitechnique characterization carried out by XRD, TEM, elemental analysis (ICP-MS) and UV-Visible spectroscopy. Furthermore, in collaboration with the Photonics Group at the University of Cagliari (Prof. M. Saba and coworkers), we have made use of ultrafast optical spectroscopy to investigate the role of the deposition site of the Pt domain on the photophysical properties of the developed heterostructures.

The results on the CdSe@CdS-Pt octapods are reported in Paragraphs 2.3÷2.5, whereas Paragraph 2.6 is dedicated to final remarks and future prospectives on the application of these novel heterostructures.

2.1 Insights on the structure of dot@rod and dot@octapod CdSe@CdS semiconducting NCs

In this work, we have selected CdSe@CdS core@shell nanocrystals as semiconducting domain for the fabrication of heterostructures with prospective use in photocatalysis. A very high degree of sophistication has been reached in the synthesis of CdSe@CdS nanocrystals with controlled shape through high temperature colloidal routes, as described in Paragraph 1.1. [57]

In particular, protocols effective in achieving shape control, are based on a careful balance of the synthetic parameters affecting polymorphism and relative energy of crystal facets, such as the presence of a suitable seed, temperature and suitable coordinating surfactants.

The systems investigated in this work are CdSe@CdS rods and octapods, which were recently obtained through seed-mediated colloidal routes. [17,58]

The proposed mechanism for the formation of such core@shell nanosystems through seed-mediated colloidal approaches is depicted in Figure 2.1. In the case of dot@rods (a) the nanocrystals can be obtained making use of a CdSe dot in the wurtzite hexagonal polymorph as a seed for the growth of CdS in the same wurtzite polymorph, mediated by a mixture of hot surfactants suited for directing anisotropic growth, such as trioctylphosphine (TOP). The synthesis of the dot@octapods (b) is definitely less straightforward and includes the synthesis of $Cu_{2-x}Se$ nanocrystals in the cubic berzelianite phase, their conversion into CdSe nanocrystals in the sphalerite (zinc blende) polymorph by Cu/Cd cation exchange and the use of the so-obtained dots as seeds for the branched growth of eight CdS arms in the wurtzite form.
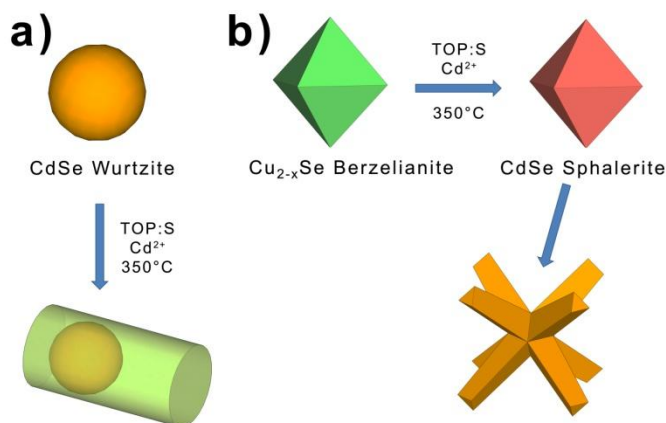

Fig. 2.1 Proposed mechanism of formation of dot@rod (a) and dot@octapod (b) starting from different polymorphs of the CdSe core.

While the mechanism underlying the formation of the dot@rods is validated by experimental support (being possible to fully characterize the initial CdSe wurtzite seeds) and the preparation protocols are well established, the mechanism of formation of the dot@octapods is currently a matter of debate with particular reference to the occurrence of the CdSe core in the zinc blende structure, which is highly unfavoured as detailed in Chapter 1, and to the role of cation exchange.

In this work we have investigated three samples made out of CdSe@CdS rods with different lengths (in the range 20-30 nm) which were grown from nearly monodisperse ~5 nm CdSe wurtzite seed, and one CdSe@CdS octapods obtained through a synthesis which proceeds via seeded growth starting from $Cu_{2-x}Se$ nanocrystals with size around 15 nm.

The samples, hereafter labeled as *rod 1, rod 2, rod 3* and *octa*, were characterized by XRD (Figure 2.2).
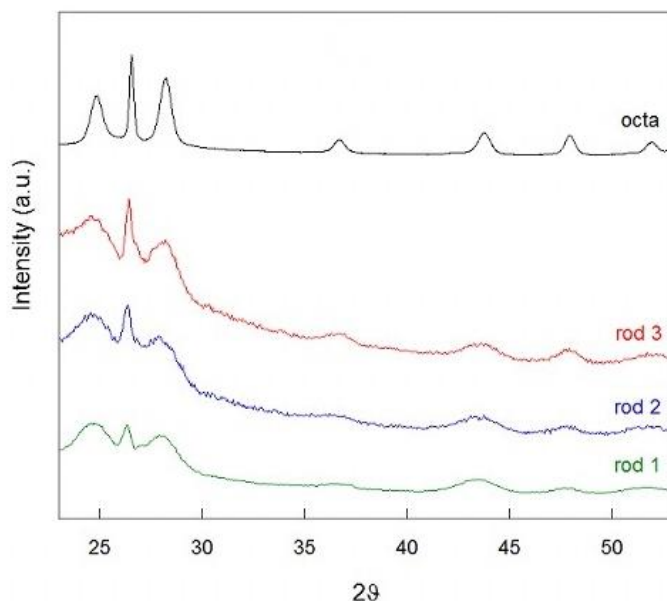

Fig.2.2 XRD pattern of the investigated CdSe@CdS samples: octapod nanocrystals and rods with different lenght.

For all the samples, XRD patterns show reflections which can be ascribed to the hexagonal (Space group P6₃mc) CdS wurtzite polymorph (PDF card 41-1049). As previously reported, [18] the relative intensity and the line broadening of the peaks clearly reflects the anisotropic growth of the nanocrystals: in particular, the 002 reflection, centred at $2\theta \sim 26.5°$, is sharper and more intense in comparison to the bulk wurtzite structure as a consequence of the nanocrystal growth along the *c* axis and its relative intensity increases in the order rod 1, rod 2, rod 3 and octa sample. These data suggest that the rod length increases going from sample rod 1 to rod 3, and that the arms in the octa sample are longer than the rod length. It is noteworthy that the CdSe phase cannot be detected by XRD, likely due to the low relative contribution from the selenide domains with respect to the sulfide ones. Also, the effect of line broadening on the diffraction profile due to nanocrystalline phases should be taken into account.

Figure 2.3 shows representative TEM images of the samples: nearly monodisperse octapod-shaped nanocrystals and rods with the same rod width and different length are observed. In particular, statistical analysis of the TEM images points out that the average arm width and length in the octa sample is 14.9 and 50.0 nm, respectively, and that the average width is 6 nm for all the rods, whereas the length varies from 21.5 nm, 27.7 nm and 30.1 nm going from the *rod 1, rod 2* and *rod 3* samples.
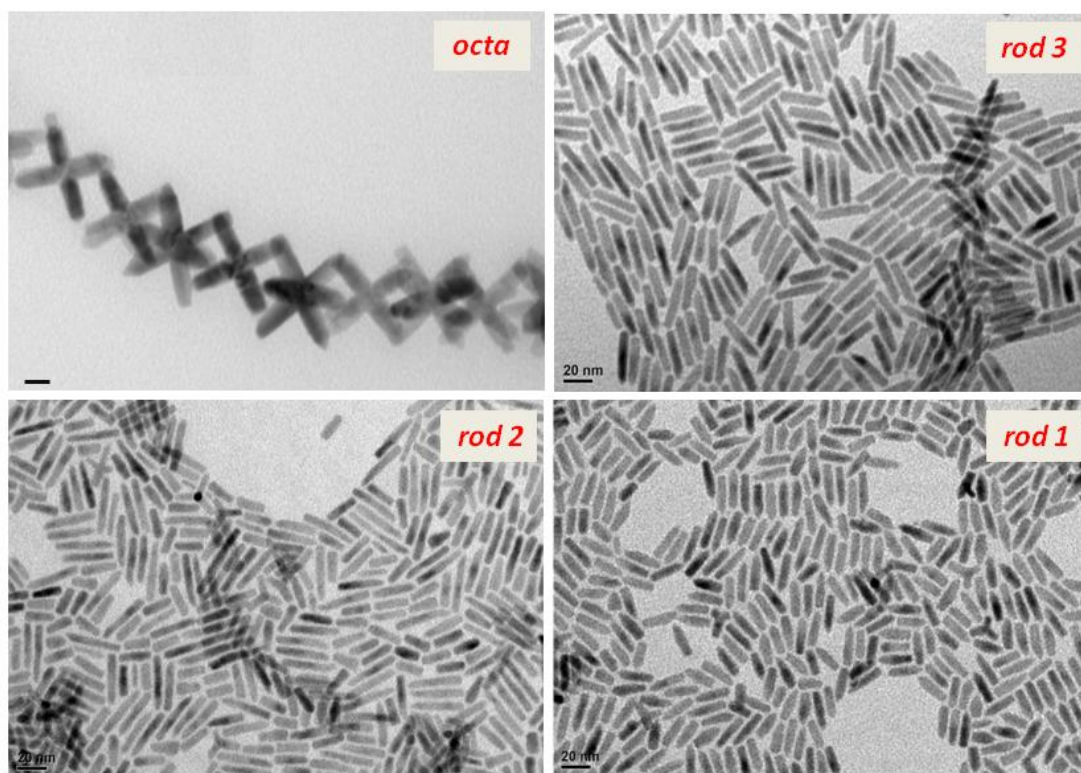
Fig.2.3 Representative TEM images of the investigated CdSe@CdS samples: octapod nanocrystals and rods with different length.

It is remarkable that the CdSe core can be barely imaged in the dot@rod nanocrystals as a slightly darker contrast close to one end of the rod, whereas no direct information can been inferred on the occurrence of the CdSe dot, being located at the core of the octapod structure. TEM observations point out that by evaporation on the TEM grid, octapods spontaneously tend to adopt an preferential position, with 4 arms lying on the grid substrate. This tendency has been recently exploited and has been demonstrated that monodisperse octapod-shaped nanocrystals self-assemble, in a suitable solution environment, on two sequential levels. First, linear chains of interlocked octapods are formed, and subsequently the chains spontaneously self-assemble into three-dimensional structures. This suggest the potential use of CdSe@CdS octapods for the development of complex and functional superstructures. [59]

UV-Visible investigation of the rod samples (Fig. 2.4, left) shows both the characteristic absorption edge at around 500 nm in wavelength corresponding to the optical bandgap of CdS and the weaker one at around 630 nm ascribable to CdSe.

In the octa sample, instead, the absorptions edge of the CdS around 500 nm is quite evident, whereas there is no evidence of the presence of CdSe. This effect is ascribed to the very low relative amount of CdSe with respect to CdS in the octa sample, as previously discussed for XRD results.

The emission peak, as obtained by photoluminescence spectra (Fig. 2.4, right) is centred around 630 nm in wavelength for all the CdSe@CdS rods, corresponding to emission from the CdSe core, as we will explain in the following Paragraph, while the octapod samples do not emit.
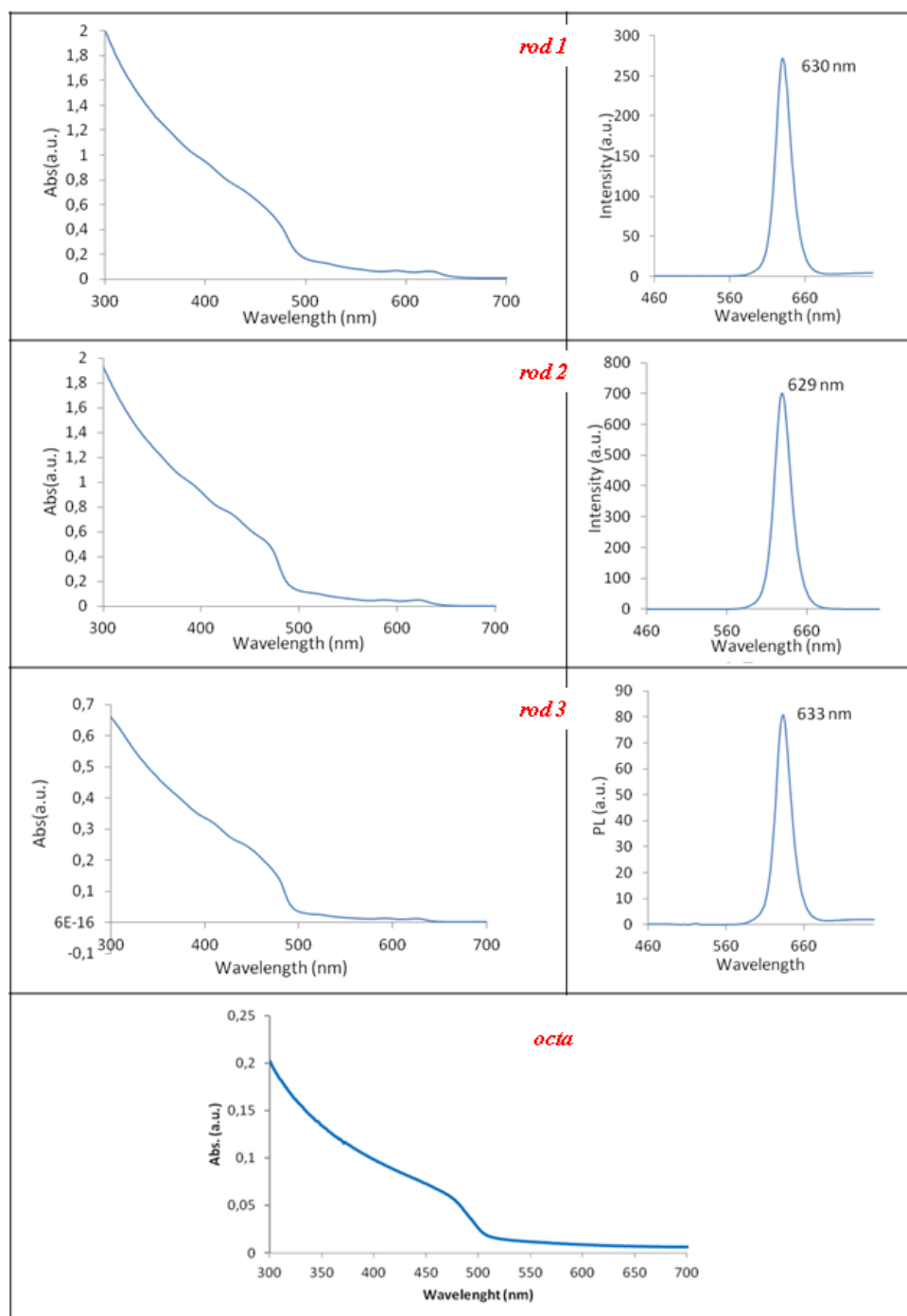
Fig. 2.4 Absorption (left) and photoluminescence (right) spectra of the investigated materials: from top to bottom rod 1, rod 2, rod 3 and octa.

In order to elucidate those structural features which were not provided by conventional characterization techniques, we have made use of X-ray absorption spectroscopy which is very suitable for the study of multicomponent, poorly crystalline materials, thanks to its high selectivity and sensitivity. In particular, by collecting the XAFS function at the absorbing edge of each different atom in the sample, one can investigate independently the local structural environment of each absorbing atom.

In this work, we have investigated for the first time core@shell CdSe@CdS nanocrystals by a multi-edge (at the Cd, S, Se, and Cu K-edges) *Extended X-Ray absorption spectroscopy* (EXAFS) study. [61]

EXAFS spectra at the B18 beamline of the DIAMOND synchrotron light source (Oxfordshire, UK), which covers a wide energy range (2.05÷35 keV) and is equipped with a double-crystal monochromator containing two pairs of crystals, Si(111) and Si(311), optimized for QEXAFS measurements. [62]

Spectra at the S (2472 eV), Cu K-edge (8979 eV), Cd (26711 eV), and Se (12658 eV) K-edges were collected at room temperature on *rod 1, rod 2, rod 3* and *octa* samples and on CdS, CdSe, CuCl reference compounds, and the detection mode (transmission, fluorescence, total electron yield) was selected based on the features of the investigated sample and/or edge.

Experimental conditions and samples object of study are presented in the Table 2.1. EXAFS data processing was carried out using the ATHENA software and the fit to scattering models in R-space was obtained by FEFF in Artemis. [63]

SAMPLE	EXAFS sample	Investigated Edges	Features
rod 1	Toluene suspension	Cd K-edge (T) S K-edge (TEY) Se K-edge (F)	dot size 4.9 nm rod length 21.5±2.6 nm rod diameter 6.0±0.6 nm
rod 2	Toluene suspension	Cd K-edge (T) S K-edge (TEY) Se K-edge (F)	dot size 4.9 nm; rod length 27.7±8.7 nm rod diameter 5.6±0.6 nm
rod 3	Toluene suspension	Cd K-edge (T) S K-edge (TEY) Se K-edge (F)	dot size 4.9 nm rod length 30.1±3.9 nm rod diameter 6.0±0.6 nm
octa	Toluene suspension	Cd K-edge (T) S K-edge (TEY) Se K-edge (F) Cu K-edge (F,T)	dot size 15 nm arm length 50.0±2.2 nm arm width 14.9±1.8 nm
CdS	Commercial powder	Cd K-edge (T) S K-edge (F)	Wurtzite polymorph
CdSe	Commercial powder	Cd K-edge (T) Se K-edge (T)	Wurtzite polymorph
CuCl	Commercial powder	Cu K-edge (T)	Sphalerite polymorph

Table 2.1. *Summary of the nanocrystals, reference compounds and related features. The EXAFS edges investigated the detection mode (T=transmission; TEY=total electron yield; F=fluorescence) are also given.*

For the sake of clarity, Figure 2.5 shows Fourier Transforms (FTs) of the experimental EXAFS function $k^2\chi(k)$ at the Cd, Se, S, and Cu K-edges for the reference compounds and for the rod 1 and octa samples.
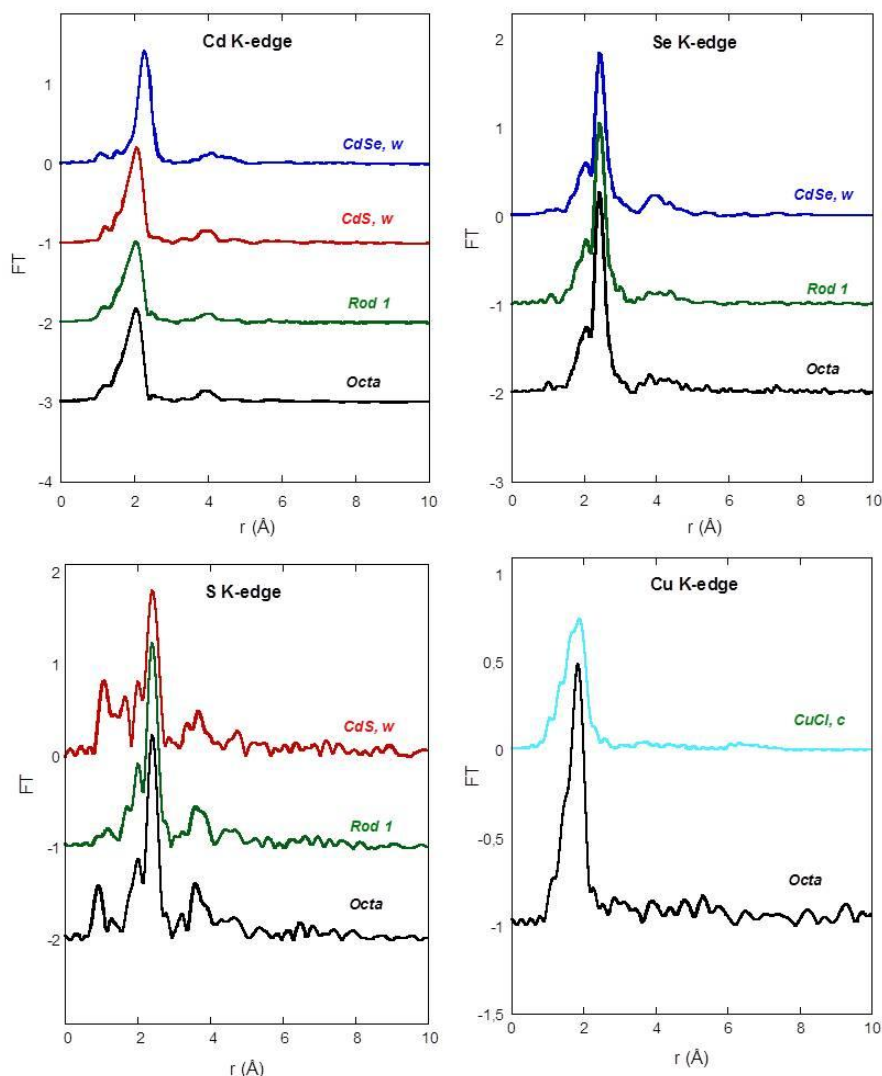
Figure 2.5 Fourier Transforms (FTs) of the experimental $k^2\chi(k)$ at the at the Cd, Se, S and Cu K-edges for the reference compounds and for the rod 1 and octa samples.

As previously stated, both the CdS and CdSe reference compounds are in the wurtzite polymorph due to poor stability of the cubic sphalerite phase belonging to Space Group F43m. Note that only the EXAFS results of the rod 1 sample are reported for the sake of clarity: all the EXAFS results on the rod 2 sample and rod 3 samples are identical to those of the rod 1 within the experimental error (except that in the case of rod 3 they were much noisier due to high dilution of the sample), thus suggesting that the structural features of CdSe@CdS rods are not at all influenced by the length of the rods.

In particular, inspection at the FTs at the Cd K-edge shows that all the samples exhibit well-defined peaks which reflect a highly structured environment. These data support the ability of the adopted synthetic procedure, i.e. the high temperature colloidal synthesis, in producing highly crystalline materials. The FTs of the samples are both quite close to the FT of the pure CdS, in agreement with the main component being CdS in the wurtzite structure both in the rods and in the octapods. On the other hand, the pure CdSe reference compound shows some relevant differences as compared to the pure CdS which are in agreement with the larger interatomic distances in the Cd-Se unit cell as compared to those in the Cd-S unit cell and to the different backscatter in the first shell.

It is interesting to note that the FT of the octa sample exhibits a closer resemblance to pure CdS with respect to the rod samples, and the differences in the features of the octa and rod samples can be ascribed to the contribution of the Cd-Se distances arising from the CdSe dot. The qualitative observations obtained on the samples at the investigated K-edges were used as a base to carry out the fitting of the data. The structural data, in terms of interatomic distances, coordination numbers, and Debye-Waller factors as obtained by best fitting parameters, indicate that Cd environment in the nanocrystals is very similar to that in pure wurtzite CdS with slight differences likely due to the CdSe core with a different environment in the rods and in the octapods. Quite remarkably, the nanocrystals are highly ordered also on their surfaces, since we did not observe a significant increase of the Debye-Waller factors due to increased structural disorder which is commonly associated to the atoms located on the surface of the nanoparticles.

Significant insights were also obtained by the EXAFS spectra at the Se K-edge: in particular, Figure 2.5 shows the FTs of the $k^2\chi(k)$ functions for the Rod and Octapod samples, together with the CdSe reference compound. The FT of pure CdSe wurtzite shows the main peak at R values around 2.4 Å (not corrected for phase shift), corresponding to the first shell, and a very broad less intense signal centered at 4 Å. The FTs of the samples at the Se K-edge are quite similar, and both the rod 1 and octa sample exhibit a more pronounced peak in correspondence to the first coordination shell. In particular, the FT of the Octa sample suggests a more ordered environment as compared to the rod and pure wurtzite CdS. Although EXAFS data of the CdSe sphalerite polymorph are not available, it should be pointed out that the main difference between the cubic sphalerite and the hexagonal wurtzite structures is that all the Se-Cd and Se-Se distances are all exactly the same in the cubic polymorph, whereas in the hexagonal polymorph there are two distinct (although similar) sets of Se-Cd and Se-Se distances. As a result, the sphalerite structure is slightly more ordered than the wurtzite structure and therefore the observed results suggest that the Se environment in the Octa sample is consistent with the more ordered structure of the sphalerite polymorph.

These results suggest the occurrence of a structural environment with higher symmetry in the octa sample, compatible with the sphalerite polymorph, which cannot be detected by XRD or TEM techniques and is in agreement with the seed-mediated mechanism of formation of the core@shell octapods depicted in Fig. 2.1.b.

EXAFS data at the S K-edge were measured on the rod, octapod and CdS wurtzite polymorph reference compound. Although noisier data with respect to the Cd and Se K-edges were obtained due to the experimental conditions required for data collection, comparison of the FTs clearly shows that the first shell is exactly the same in all samples, and further support that in all samples the sulfur structural environment matches with CdS in the wurtzite polymorph.

Finally, on the octapod samples, the Cu K-edge was also investigated, since a copper compound is used as a starting material to induce the formation of a selenide core in the blende structure. Note that data collected in transmission mode did not show any evidence of a Cu K-edge, pointing out the successful cation exchange of Cd(II)/Cu(I) during the synthetic protocol and that if any Cu is left, this must be below detection limit in this experimental conditions. However, the fluorescence detector was able to provide a much more powerful tool to detect even tiny traces of an element, and the FTs of the CuCl starting compound (having a cubic sphalerite structure) and of the Octa samples are reported in Figure 2.5. Although the curve for the Octa sample is quite noisy, as expected due to the very low Cu content, some structural information can be inferred. In particular, the

comparison of FT of the octapods with those of the CuCl compound in the sphalerite polymorph suggests that the copper environment in the Octa sample is not the same as in CuCl. In particular, while the main peak in the FTs is centered at approximately the same distance, which is consistent with the distance originating the oscillations being similar to the Cu-Cl distance in the first coordination shell, the magnitude of the FT peak is higher in the Octa sample compared with the CuCl, which also indicate that a heavier backscatter than Cl (such as Se) must be present. Our data indicate that in the Octa sample, while there is no trace at all of the initial CuCl used as a precursor, a tiny amount of the $Cu_{2-x}Se$ intermediate phase which has not undergone cation exchange and has not converted into CdSe is still present.

Overall, multi-technique physico-chemical characterization of core@shell chalcogenide nanocrystals enabled to elucidate the main structural and morphological features of the investigated samples. In particular, by adopting well-defined synthetic protocols based on seed-mediated high temperature colloidal routes, CdSe@CdS heterostructures with a highly controlled morphology, i.e. nearly monodisperse elongated dot@rods and dot@octapods were obtained. Dot@rod samples with the same diameter (6 nm) and different length (from around 20 to 30 nm) share very similar structural features, and exhibit tunable optical properties. Our findings are in agreement with the current view on these materials as being made of a highly crystalline CdSe wurtzite core and a highly passivated CdS wurtzite arm.

Concerning the octapod samples, while TEM and XRD provide valuable information on the nanocrystal morphology and size, no information on the features of the core and on the possible occurrence of impurities and/or secondary phases related to the complex synthetic procedure could be obtained by this techniques. We have therefore successfully exploited the potential of EXAFS in providing quantitative structural information on the local structure of individual atoms in multicomponent materials in terms of number and type of neighboring atoms around the selected absorbing atom, interatomic distances, and Debye-Waller factors. EXAFS results enabled us to support the occurrence of a sphalerite CdSe core that was almost impossible to assess with other techniques, and to gather more detailed information on the effectiveness of the Cu/Cd ion exchange. Our findings provide experimental support for the models on the growth of shape-controlled core@shell chalcogenide heterostructures proposed in Figure 2.1.

2.2 Pt-metal doped CdSe@CdS rod and octapod heterostructures

Heterostructures constituted by semiconducting domains combined with discrete nanoscale metal domains in controllable manner have emerged as new nanomaterials for photocatalytic and photovoltaic applications. In particular, as mentioned earlier, CdSe@CdS-Pt shaped rod nanocrystals have been prepared and successfully applied in the photocatalytic water splitting reaction. [56]

The electronic alignment of the band in pure CdSe@CdS rods after optical excitation consist of electrons, which are delocalized through the whole nanocrystal and holes, which diffuse and remain localized in the core of the CdSe; recombination occurs therefore more likely in CdSe (emitting at 630 nm) where the band gap is large with respect to that of CdS (Eg_{CdSe}=1.74 eV, Eg_{CdS}=2.42 eV).

In Pt tipped CdSe@CdS rods, instead, holes remain three-dimensionally confined to the CdSe, whereas the delocalized electrons are transferred to the metal Pt tip (Fig. 2.6). [56]

Hence, Pt catalyst grown on the tip provide the unique advantage of being able to control the separation distance between the photogenerated electron and hole; consequently, the electrons are by the way separated from the holes over three different components.
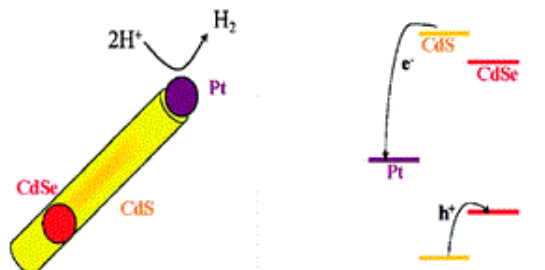

Fig.2.6 An illustration of the energy band diagram in CdSe@CdS-Pt heterostructures indicating that holes are confined to the CdSe while electrons are transferred to the Pt. [56]

Within the framework of this research work, we have used CdSe@CdS rod samples to set up the experimental synthetic and characterization procedures of hybrid semiconductor-metal heterostructures, with the aim to extend this approach to the deposition of Pt on more complex nanocrystals such as octapods.

Figure 2.7 shows representative images of the CdSe@CdS-Pt rod heterostructures synthesized in our laboratories by depositing platinum on top of a preformed rod sample.
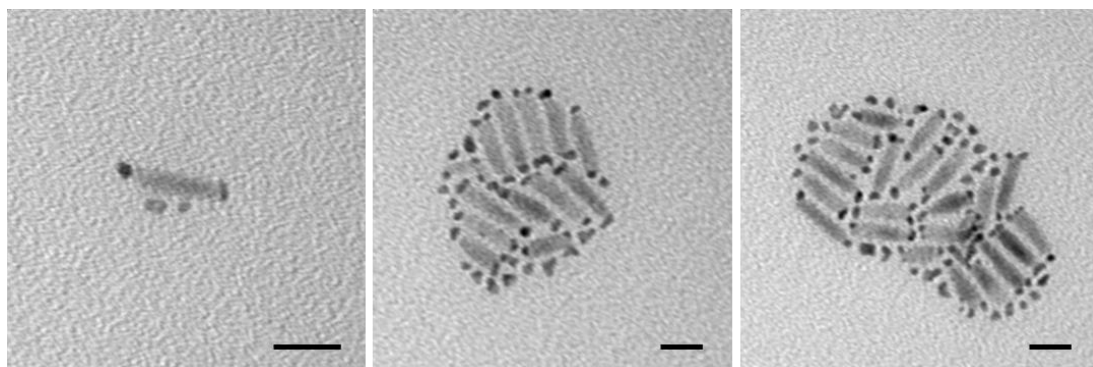

Fig.2.7 CdSe@CdS-Pt elongated heterostructures (scale bar is 20 nm)

Our results are in agreement with the data presented in the literature, which show that heterostructures with selective deposition of the second domain can be obtained by exploiting the different reactivity of the surfaces exposed in the rod structure.

In particular, the anisotropic wurtzite crystalline structure of the CdS shell on rods promotes selective growth of metal domains on different facets. The reactivity of the nanorods is higher at the tips than along the body of the rod due to the increased surface energy, which also leads to preferential growth along the <001> axis of the CdS rods. [55]

In this work, our attention has been mainly focused on the fabrication of semiconductor-metal heterostructures constituted of branched CdSe@CdS with octapod shape decorated with metal Pt tips, which have not been achieved so far.

The aim of the decoration procedure is to control the geometry of the attachment of Pt to the CdS surface, without varying the morphology of octapod nanocrystals nor that of Pt domains.

A major synthetic challenge for the design of tipped CdSe@CdS octapods relates to the possibility to achieve controlled deposition of Pt nanocrystals at selected sites of the three dimensional branched nanocrystals, due to the more complex morphology and kind of surfaces exposed by the semiconductor domain as compared to rods. The following

paragraphs will provide details on the synthetic procedure and characterization techniques used for the design of Pt-decorated CdSe@CdS octapods.

2.3 Synthesis of CdSe@CdS-Pt octapods

Recent advances in nanocrystal fabrication have managed to produce CdSe@CdS octapod nanocrystals realizing highly branched yet well defined nanostructures, as discussed in Chapter 1.

Our research has been focused on the fabrication of hybrid heterostructures constituted of branched CdSe@CdS semiconductors with octapod shape, decorated with metal Pt NCs. In particular, starting from the protocol described by Mokari and coworkers for CdSe@CdS-Pt dot@rod [64] we have developed a procedure for controlling the deposition of Pt nanocrystals at given sites of the octapod nanocrystals while preserving the same size of the Pt nanocrystals.

The deposition of platinum tips on the CdSe@CdS octapods was performed using Schlenk line procedures.

Among the different parameters which may affect the outcome of metal tip Pt deposition procedure, we have investigated the relative amount of semiconductor with respect to metal precursor, temperature and growth time, while keeping fixed the kind of precursors, surfactants and solvents as well as the amount of the latter two. Table 2.2 summarizes the chemicals used for the synthesis of the CdSe@CdS-Pt heterostructures.

SURFACTANTS	OLEIC ACID	$C_{18}H_{34}O_2$	>90%, Fluka
	OLEYLAMINE	$C_{18}H_{37}N$	70%, Sigma Aldrich
	1,2 HEXADECANEDIOL	$CH_3(CH_2)_{13}CHOHCH_2OH$	90%, Sigma Aldrich
SOLVENTS	DIPHENYL ETHER	$C_{12}H_{10}O$	Sigma Aldrich
	DICHLOROBENZENE	$C_6H_4Cl_2$	≥99%, Fluka
PRECURSOR	Pt(II)-acetylacetonate	$Pt(acac)_2$	≥99.99% Aldrich

Table 2.2 Chemicals reagents used for deposition of Pt metal domains on CdSe@CdS nanocrystals.

We found that the relative amount of octapods and platinum has a major influence on the deposition of platinum on the pre-formed semiconductor octapods and we found that the most reliable procedure is obtained by using always a stock suspension of octapod in toluene with a given concentration and varying the amount of platinum precursor dispersed in dichlorobenzene. For all the synthesis, a stock solution of preformed octapods in toluene was used having a concentration of 0.912 g mL^{-1}.

In a typical synthesis (Table 2.2, Fig. 2.8), 43 mg of 1,2-hexadecanediol (90%), 0.2 mL of oleylamine (70%), 0.2 mL of oleic acid (>90%) and 10 mL of diphenyl ether were mixed in a 25 mL three-neck-flask and first heated at 80 °C under vacuum for 30 min while refluxing, and then placed under flowing nitrogen and heated up to 200 °C. At this temperature, a mixture containing 1 mL of pre-formed CdSe@CdS octapod stock solution and platinum acetylacetonate (99.99%) in 1 mL of dichlorobenzene (>99%) was rapidly injected into the flask.
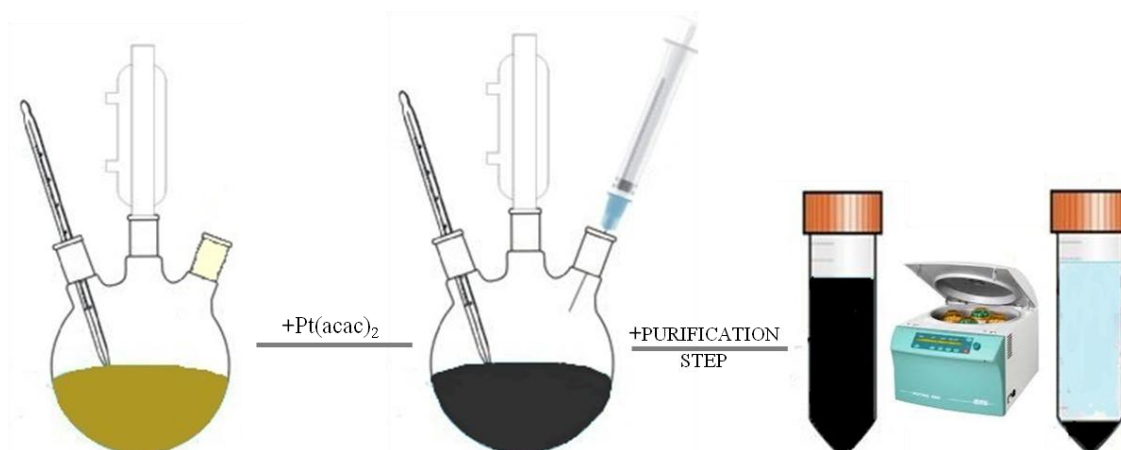
Fig. 2.8 Experimental steps involved in CdSe@CdS-Pt heterostructures colloidal synthesis at high temperature.

While the amount of octapods was kept fixed in all the synthesis, the amount of platinum precursor was varied in the range 0.2-1 mg. The formation of Pt tips is accompanied by a change in color from yellow to dark when relatively high concentrations of platinum precursor is used. After 30 min the reaction was removed from the heating bath and quenched by submerging the flask in an ice bath.

The CdSe@CdS-Pt heterostructures were collected and purified by three cycles of precipitation by adding an excess ethanol and centrifugating at 4000 rpm for 10 minutes, discarding the supernatant, and dispersing in toluene.

As a reference material, octapod were submitted to the same heat treatment without injecting the Pt precursor. The obtained sample, labeled "Pt-free octapods" was used to rule out the occurrence of physico-chemical transformations of the semiconductor domain due to the tipping procedure.

2.4 Structural and morphological properties of CdSe@CdS-Pt octapods

The prepared materials were investigated through a multi-technique approach in order to gain insights on the features of the synthesized heterostructures.

Figure 2.9.a shows representative images of the octapod sample heated under the conditions used for the tipping procedure except for the use of the Pt precursor (Pt-free octapod sample): it can be inferred that the size and shape of the nanocrystals is the same as the original octapods (see Figure 2.2 as a reference). Hence, it is deduced that the semiconducting domain is not affected by the reaction conditions used for the deposition of the metal domain.

In order to produce the CdSe@CdS-Pt heterostructures, the amount of platinum precursor used during the synthesis was carefully adjusted in order to favour heterogeneous nucleation of Pt on top of the octapods versus homogeneous nucleation, and to direct tip deposition at the desired site. In Figure 2.9.b-c TEM images of samples obtained by using increasing relative amounts of platinum and octapods (in particular 1 mg and 0.2 mg of Pt precursor per mL of octapod stock solution) are reported. In both samples, the amount of free platinum nanocrystals is negligible, indicating the success in avoiding homogeneous nucleation.
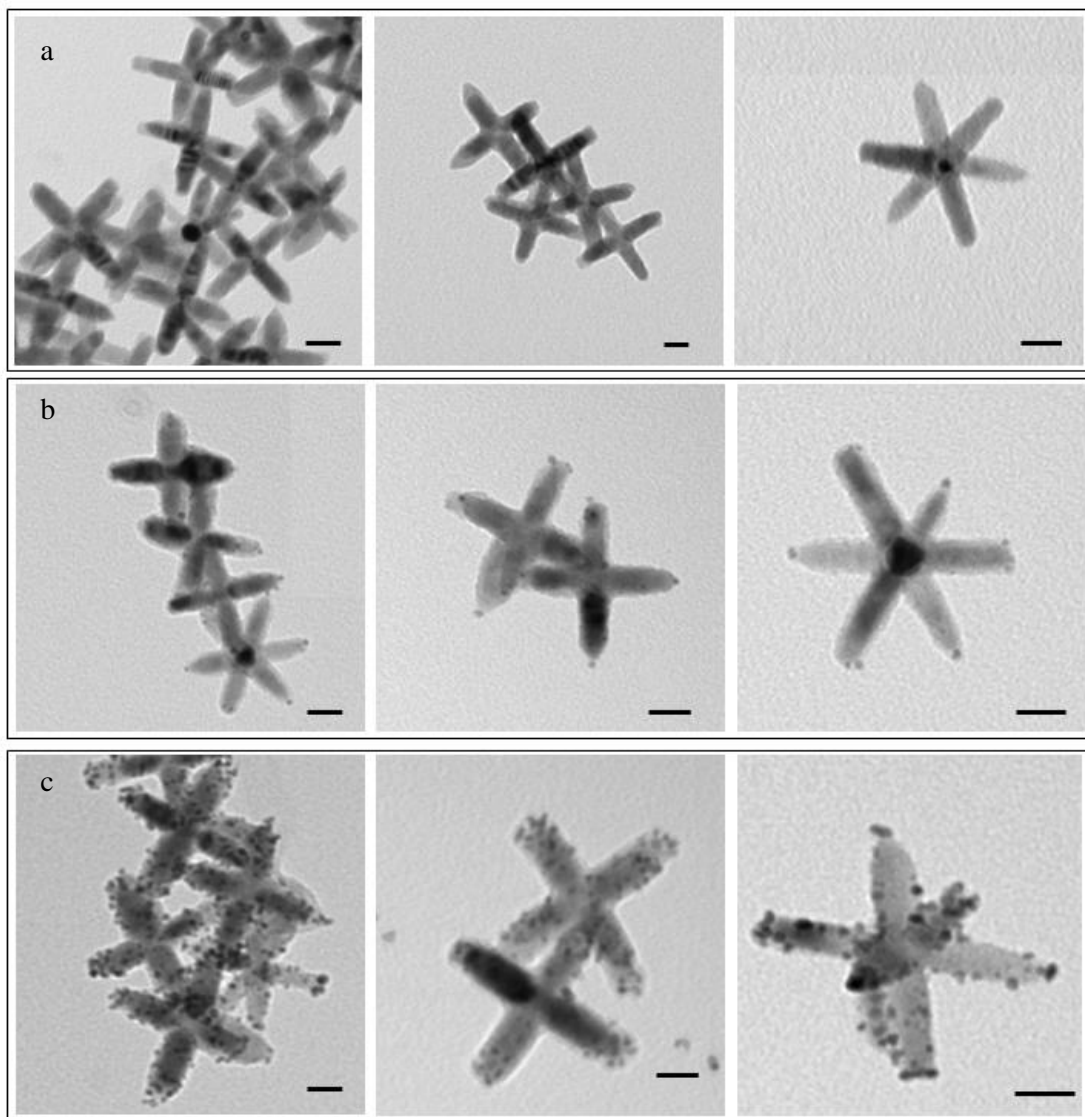
Fig. 2.9 TEM images of octapod nanocrystals prior to Pt deposition (a) and CdSe@CdS-Pt heterostructures tipped (b) and covered (c) by platinum. Scale bars are 20 nm for all micrographs.

A low Pt concentration, Pt deposition is directed preferentially on the tip of the octapods, as shown in Figure 2.9.b. Closer inspection at the CdSe@CdS-Pt heterostructures shows that at one end of an arm a single tip is deposited, whereas at the opposed end two tips are observed. This observation is in agreement with the described model on the formation and crystal structure of CdSe@CdS octapods. In fact, the octapod arms grow along the <001> axis of the wurtzite structure which is not centrosymmetric, and as a consequence the octapods are made out of pairs of opposed arms exhibiting a sharp edge and a flat end. These peculiar microstructural features reflect in the site of deposition of the Pt tips, so that the CdSe@CdS-Pt tipped heterostructures present one Pt nanocrystal on the sharp edge and two Pt nanocrystals at the edges of the flat end. In addition to the site of deposition onto the semiconductor domain, the developed procedure is successful in producing metal tips with nearly monodisperse size, of around 3.5 nm. This result is ascribed to the sudden decomposition of the platinum precursor, which results in single nucleation and controlled growth process.

When the amount of platinum precursor is increased up to five-fold, a different CdSe@CdS-Pt heterostructures morphology is obtained. In particular, as shown in Figure 2.9.c, the

heterostructures are made out of octapods which are covered on their outer surface by Pt nanoparticles. Closer look at the site of deposition of the platinum nanoparticles shows that, as expected due to their relatively higher reactivity, in addition to the surface of the octapod arms, the arm ends are always tipped. It is interesting to note that the average particle size of the metal domain in the Pt-tipped and Pt-covered heterostructures is the same.

We ascribe this result to the considerable length of the CdS arms relative to the metal particles, so that each tip may act as an isolated nucleation site in independent way. Increasing the amount of Pt relative to the concentration of CdS rods leads to simultaneous nucleation and growth of Pt nanoparticles along the body of the octapod in addition to the tips.

XRD patterns of the CdSe@CdS-Pt heterostructures were collected and are reported in Fig. 2.10 together with that of pure octapods as a reference (Pt-free octapods). It can be inferred that Pt-free is as pure octapod sample shown in Paragraph 2.1.

The patterns reflect the occurrence of anisotropic hexagonal CdS phase and peak broadening provides size estimates in agreement with what inferred directly from TEM images, an indication that nanocrystals are mainly single crystalline domains. In addition, the main reflection of the Pt structure (PDF card 4-802) can be observed in the Pt-covered octapods, with average nanocrystal size 3.5 nm.
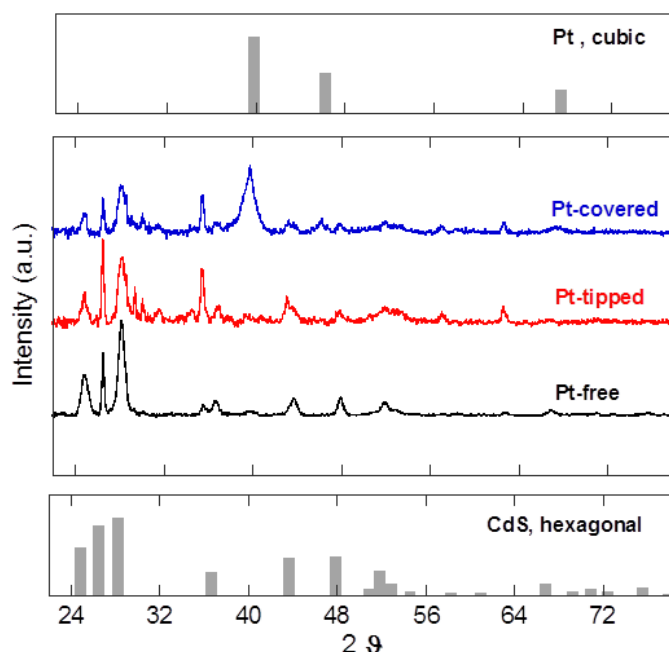

Fig.2.10 X-ray diffraction patterns of the Pt-free, Pt-tipped, and Pt-covered octapod nanocrystals. The diffraction peak position of the bulk CdS hexagonal and Pt cubic structures are reported on the bottom and on top, respectively, as a reference.
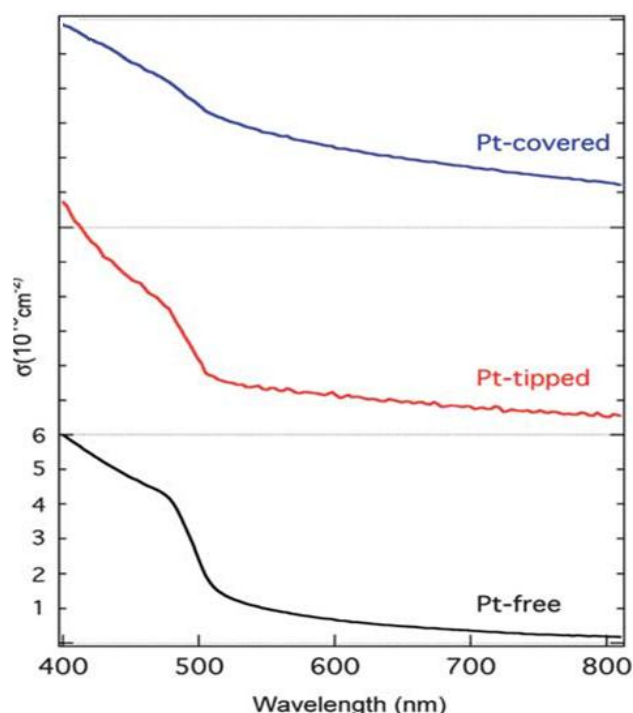
Fig.2.11 UV-Vis absorbance measured in a toluene dispersion of Pt-free, Pt-tipped and Pt-covered octapod nanocrystals.

Figure 2.11 shows the effects of Pt decoration on the optical absorption: spectra for Pt-free octapods are characterized by a sharp absorption edge around 500 nm in wavelength, corresponding to the optical bandgap of CdS, followed by a Rayleigh diffusion tail; knowing the concentration of nanocrystals in dispersion, we have determined the absorption cross section to be ~$6 \cdot 10^{-13}$ cm^2 at 400 nm.

When Pt is added, Rayleigh diffusion grows with the amount of Pt, as expected from plasmonic field enhancement effects, although clear plasmon resonance is observed. The absorption cross section does not appear to be significantly modified by the Pt decoration procedure; however, the limited quantities of Pt decorated nanocrystals obtained after purification procedures have prevented an accurate determination of the concentration of nanocrystal dispersions and therefore uncertainties of the order of 30% need to be considered for the quantitative assessment of the absorption cross section.

2.5 Charge separation in Pt-decorated CdSe@CdS octapod nanocrystals

The photophysics of Pt-decorated octapod nanocrystals has been studied by ultrafast optical spectroscopy, in particular femtosecond transient absorption, a technique sensitive to the dynamics of the excited state. [65]

The two main techniques that were used are *transient absorption spectroscopy* (also called "Pump Probe") and *time-resolved photoluminescence spectroscopy,* which allow one to investigate in a very precise way the main optical properties and dynamics of charge carriers of the nanocrystals.

In particular, transient absorption tracks photoexcited electrons, but is mostly blind to photoexcited holes whereas time-resolved photoluminescence is sensitive to the simultaneous presence of electrons and holes.

2.5.1 Transient absorption spectroscopy

The differential transmission signal induced by the pump laser pulses is almost exclusively attributed to photoexcited electrons, while holes do not contribute, due to the peculiar electronic level structure of CdSe and CdS nanocrystals, where hole states are closely spaced together and the states at the very top of the valence band are not coupled to optical transitions.

Care was taken to avoid nonlinear effects due to multiple excitation of each nanocrystal by each laser pulse. Characterization of the Pt-free octapod sample was performed in order to exclude that the Pt decoration procedure introduces surface trap states that can lead to similar photophysical signatures as electron capture by Pt domains.

The differential transmission traces (Fig.2.12.a) are shown as a function of the pump-probe delay, so they reproduce the temporal dynamics of photoexcited electrons in the nanocrystals: Pt tipping accelerates the electron decay with respect to Pt-free nanocrystals, meaning that electrons can be trapped at the tips in a time scale of few hundreds of ps; a fit to a single exponential decay without constant background gave characteristic times of 630±50 ps for Pt-free nanocrystals and 260±30 ps for Pt-tipped nanocrystals.
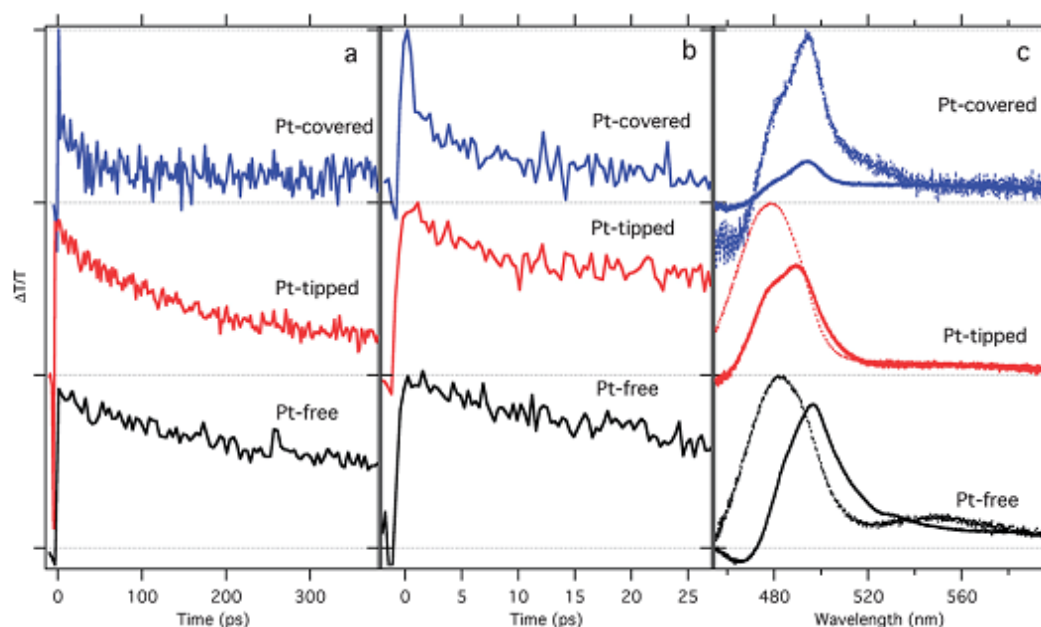

Fig.2.12 a) Decay of the spectrally-integrated differential transmission signal as a function of pump-probe delay for CdSe@CdS octapod nanocrystals with different Pt decorations; the spectral integration window is 460-520 nm; signal amplitudes are normalized and vertically displaced for clarity. b) Zoom of the initial decay. c) Corresponding differential transmission spectra; the dotted lines are the spectra at time delay equal zero (integrated over a 400 fs window), the continuous lines are the spectra integrated between 7 ps and 20 ps delay times.

When the nanocrystals are entirely covered by Pt, however, the electron capture becomes much faster and is almost complete in a ps timescale, as shown in the zoom of the initial decay (Fig. 2.12.b).

Differential trasmission spectra (Fig. 2.12.c) reveal the photophysical processes. In Pt-free octapods and in tipped octapods the differential transmission spectra show similar dynamics: at time zero, just after excitation with the pump pulse, the bleaching is centred at 480 nm in wavelength, which has been associated by Scotognella and coworkers [66] to the 1D electron state delocalized along the pod; after a short transient of ~1-2 ps, the bleaching shifts towards

the red and the corresponding peak moves to around 495 nm, a wavelength associated to the 0D electron state localized in the center of the nanocrystal.

Such dynamics is the signature of energy relaxation of photoexcited electrons from higher to lower energy states in the conduction band, accompanied by a spatial migration from the pods (1D states) toward the nanocrystal center (0D states). 0D states are localized not by a band potential, but mainly by a geometric effect, as the nanocrystal cross section is larger in the core than in the pods and the corresponding confining energy is lower. Therefore 0D states would exist even in a nanocrystals with CdS core and extend well within the CdS arms. Such localization is shallow, as the difference in energy between 0D and 1D states is around 70 meV, the effective mass for electrons is just 0.1 and thermal energy K_BT is at least 26 meV.

Relaxation is very similar in Pt-free and Pt-tipped nanocrystals because electron capture in tipped nanocrystals is a much slower process than energy relaxation, which is completed in ~1 ps. As a consequence, electron capture in Pt-tipped nanocrystals occurs from the 0D states, mostly localized in the center, which have little spatial overlap with the Pt domains located on the opposite side of the pods. As the localization of 0D states is mild, electron capture could be characterized as a tunneling through a shallow barrier.

The photoinduced absorption band at 460 nm is attributed to Stark effect, i.e. the electric field created upon the excitation of electrons and holes that have not a perfect spatially overlap. The Stark signal is expected to scale as a combination of first and second derivative of the absorption spectrum and is therefore more pronounced in the samples where the absorption features are sharper, i.e., in Pt-free octapods.

In Pt-covered nanocrystals, relaxation from 1D to 0D states does not occur, as the bleaching of the 0D state always dominates over the one corresponding to the 1D state, even immediately after excitation. Furthermore, combining the differential transmission with the absorbance spectra, we can calculate the peak in transient absorption signal ($\Delta\alpha/\alpha_0$) to be about 4 times lower in Pt-covered nanocrystals than in Pt- free and Pt-tipped ones, where instead the values are about the same. We interpret the observation as an indication that bleaching in Pt-covered nanocrystals is only due to the fraction of electrons that after excitation directly relax into the 0D state, without transiting by the 1D states; on the other hand, we infer that electrons in the 1D states are captured by Pt domains before relaxation occurs, while they are still hot. In other words, electron capture in Pt-covered nanocrystals is fast enough to compete with energy relaxation.

Since relaxation into the 1D states appears instantaneous in Pt-free nanocrystals, we also infer that electron capture in Pt-covered nanocrystals is faster even than the laser pump pulse duration.

2.5.2 Time-resolved photoluminescence spectroscopy

CdSe@CdS octapod nanocrystals are known as inefficient emitters, as opposed to other CdSe@CdS colloidal nanostructures, such as spherical core@shell and dot@rods. The low photoluminescence quantum yield has been ascribed so far to the peculiar synthesis technique, which involves cation exchange of the original Cu_2Se core to produce the CdSe seed for nucleation of the eight CdS arms, a procedure that may leave potential barriers and crystal defects at the CdSe@CdS interface, inhibiting the relaxation of holes into the CdSe core. As a consequence the optical emission from octapod nanocrystals does not occur from the CdSe core, but from the CdS arm, and is centred in wavelength around 480 nm, as shown in Fig. 2.13 a. The emission spectrum is slightly blueshifted in Pt-tipped and Pt-covered nanocrystals.

The photoluminescence of Pt-free octapod nanocrystals decays in~ 100 ps, a value close to the resolution of the used streak camera; since transient absorption indicates a longer lifetime for electrons, we attribute the photoluminescence decay to hole trapping at the CdS surface. The photoluminescence dynamics is different in Pt-tipped and Pt-covered nanocrystals, as the decay becomes longer. It has to be noted however that the longer photoluminescence decay is not accompanied by a higher quantum yield; in contrast the quantum yield stays below 1% in all samples and is about 3 times lower in Pt-tipped and Pt-covered nanocrystals than in the Pt-free ones. This observation is consistent with transient absorption showing that the lifetime of electrons inside the nanocrystals is shortened by the addition of Pt.
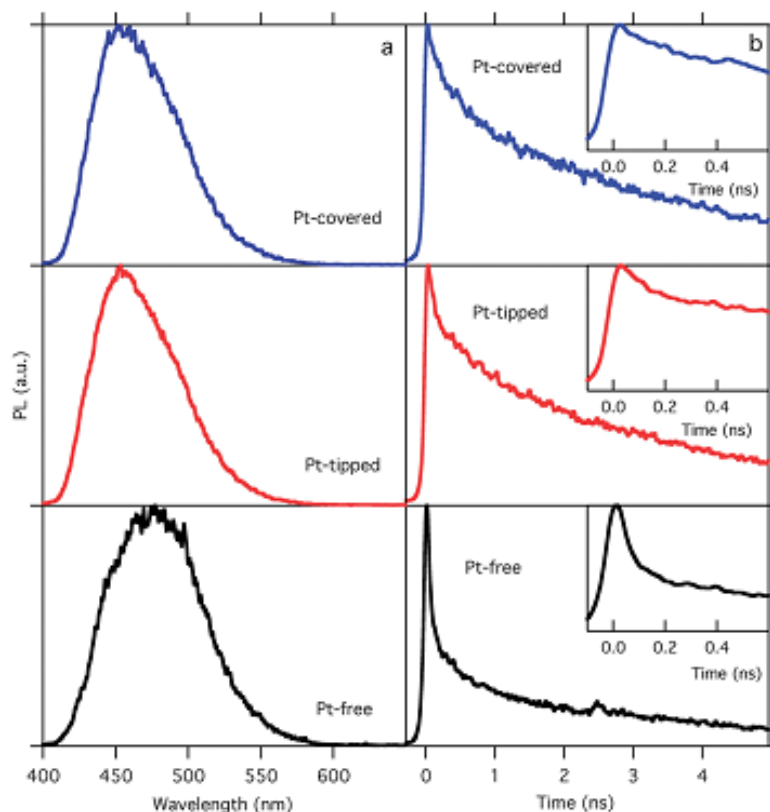

Figure 2.13: a) Photoluminescence spectra for octapod nanocrystals. b) Corresponding temporal decay of the normalized photoluminescence signal; spectral integration is done over the whole photoluminescence spectrum, 400-600 nm. Vertical displacements are for clarity. The insets show a magnification of the initial photoluminescence transient.

However, the timescales involving electron capture and photoluminescence decay are different by at least one order of magnitude, therefore the quantum yield value cannot be linked quantitatively to the electron capture rate. Electron capture in Pt-tipped and Pt-covered nanocrystals may have different rates, but after few hundred ps, the total number of electrons that have been captured and therefore subtracted from photoluminescence may be similar, resulting in a comparable PL quantum yield. We infer that the treatment employed for Pt decoration affects the hole surface traps, probably saturating the deepest ones and therefore slowing down the hole recombination. The above results were also supported by characterization of the photophysical behaviour under high excitation regime as detailed in reference 65.

2.6 Prospective application of CdSe@CdS-Pt octapods in photocatalysis

Large nanocrystals with a spatially controlled metal-semiconductor heterostructure represents a versatile playground for testing some of the photophysical processes relevant for solar photoconversion.

Photocatalysts based on CdSe@CdS heterostructured semiconductors are particularly suited due to their band alignment, with conduction bands almost aligned and the CdSe valence band at higher energy than the CdS one. In these systems, tuning of the microstructure and morphology provides a means to affect the relaxation paths of photoexcited electrons and holes, which are affected by surface and interface morphology. In particular, CdSe@CdS-based elongated nanocrystals decorated at the surface with noble metal domains, employing a variety of methods for nanocrystal decoration and resulting in different sizes, shapes and locations of the metal domains, have been pursued as photocatalysts for hydrogen production though the water splitting reaction. In the specific case of CdSe@CdS-Pt rods, it has been demonstrated that the optimal heterostructures for photocatalytic water splitting process are CdSe@CdS-Pt rods with metal tipping located at one end, specifically the end most far away from the CdSe seed. As previously explained, this is ascribed to the fact that in such structures holes are three-dimensionally confined to the CdSe, whereas the delocalized electrons are transferred to the metal tip.

By tuning the nanorod heterostructure length and the seed size, in 2010 Alivisatos and co. were able to significantly increase the activity for hydrogen production compared to that of unseeded rods. [56] This structure was found to be highly active for hydrogen production, with an apparent quantum yield of 20% at 450 nm, and was active under orange light illumination and demonstrated improved stability compared to unseeded CdS rods.

Based on the above findings, we prospect that the novel heterostructures developed in this work based on Pt-decorated CdSe@CdS octapods are very promising candidates for photocatalytic applications. In particular, we have demonstrated that the presence of Pt domain onto the semiconducting domain plays a key role in determining the capture of photoexcited electrons, i.e. the initial step of photocatalytic reactions. In addition, the peculiar shape of the developed heterostructures offers several distinctive advantages for photocatalytic applications, namely controlled charge separation and large absorption coefficients.

Even more important, the absorption cross section is very high, as much as $5 \cdot 10^{-12}$ cm^2 at 500 nm, meaning that under AM 1.5 solar illumination photoexcitations in each nanocrystal can be created at rates equal to 10^5 sec^{-1}.

However, based on the photophysical properties of the Pt-decorated CdSe@CdS octapods, it is unclear whether complete surface coverage or selective tipping of the octapods by Pt domains is the most promising nanocrystal architecture, likely due to a lack of direct comparison among heterostructures with the same composition and size enabling direct correlation between microscopic structure and optoelectronic function. Application of the developed CdSe@CdS-Pt octapods as catalysts in the photocatalytic water splitting reaction will offer the opportunity to investigate which scenario will optimize catalytic efficiency: either selective Pt tipping of octapods which provides control over the spatial separation between electrons and holes while minimizing the amount of noble metal employed; or non selective Pt coverage of octapods which leads to faster charge separation, but may be less efficient in catalyzing reactions or more prone to unwanted recombination paths leading to back reactions.

With this regard, it is expected that the octapod-based heterostructures should offer a significant improvement in the application of metal-semiconductor catalysts to the water splitting reaction and to the design of devices for hydrogen production. In fact, it is anticipated that the reaction could be carried out on top of nanocrystals previously deposited on a substrate by solvent evaporation, as pure octapods have been demonstrated to self-assemble in three dimensional structures. [59]

On the other hand, photocatalytic water splitting tests on CdSe@CdS-Pt rods have been conducted under pseudo-homogeneous conditions in water media. To this end, the hydrophobic tipped rods have been subjected to time-consuming and low-yield surface modification procedures in order to promote dispersability of the rods in aqueous environment.

Overall, the developed Pt-decorated CdSe@CdS octapod represent novel prospective photocatalysts with improved performances for applications relevant in energy and environmental fields such as hydrogen production through the water splitting reaction by exploiting sunlight.

Chapter 3

Heterostructures based on magnetic iron oxide

Magnetic nanoparticles have emerged as functional materials with a wide range of applications in health care (cancer therapy, targeted drug release, diagnosis), industrial chemistry (magnetically recoverable catalysts), photonics (light emission and modulation) and data storage (magnetic memories).[67]

Such versatility is prompted by the magnetic dynamics of particles at the nanoscale range, which differ substantially from those of the corresponding bulk magnets, as discussed in Chapter I.

A peculiar role is played by the magnetic iron oxide polymorphs, magnetite and maghemite (Fe_3O_4 and γ-Fe_2O_3 respectively) both taking place in the spinel ferrite structure, due to their natural occurrence both in the environment and biological systems. In fact, to date iron oxide nanoparticles are the only materials approved for in vivo use both by the European Medicine Agency and the U.S. Food and Drug Administration. [33]

In addition, magnetic iron oxide nanoparticles have attracted increasing attention due to their implication in the development of magnetic nanoparticles as tools for therapeutic and diagnostic biomedical applications, as described in Paragraph 1.3.3.

Recently, the focus of synthetic efforts has been directed towards the creation of new nanomaterials obtained by the assembly into secondary structures, which preserve superparamagnetic behaviour of the constituent nanoparticles building blocks.

These so called colloidal nanocrystal clusters (CNCs) [68] consist of single crystallites of 10 nm in size, which aggregate into secondary structures to form flowerlike systems; these resulting nearly spherical heterostructures have the overall diameter depending on the number of nanocrystals present, ranging from few tens to about a hundred of nm, as depicted in Figure 3.1.

The fabrication of nanoparticle clusters offers the advantage to address many challenges that are currently limiting the direct use of colloidal single nanoparticles in some applications. In particular, superparamagnetic nanoparticles suffer from the drawback of having relatively moderate values of overall magnetization due to two main effects: i) the relatively small

number of magnetic atoms associated to limited particle size which are imposed by the single domain limit; and ii) the relatively significant contribution from surface versus core atoms with their associated spin coating. As a consequence, small nanoparticles are difficult to effectively separate them from solution or control their movement in blood by using moderate magnetic fields, limiting their use in some practical applications such as separation and targeted delivery.

On the other hand, magnetic clusters exhibit at room temperature the superparamagnetic properties of the constituent primary nanoparticles and very high magnetization typical of large magnetic particles, as shown in Figure 3.1. [69]
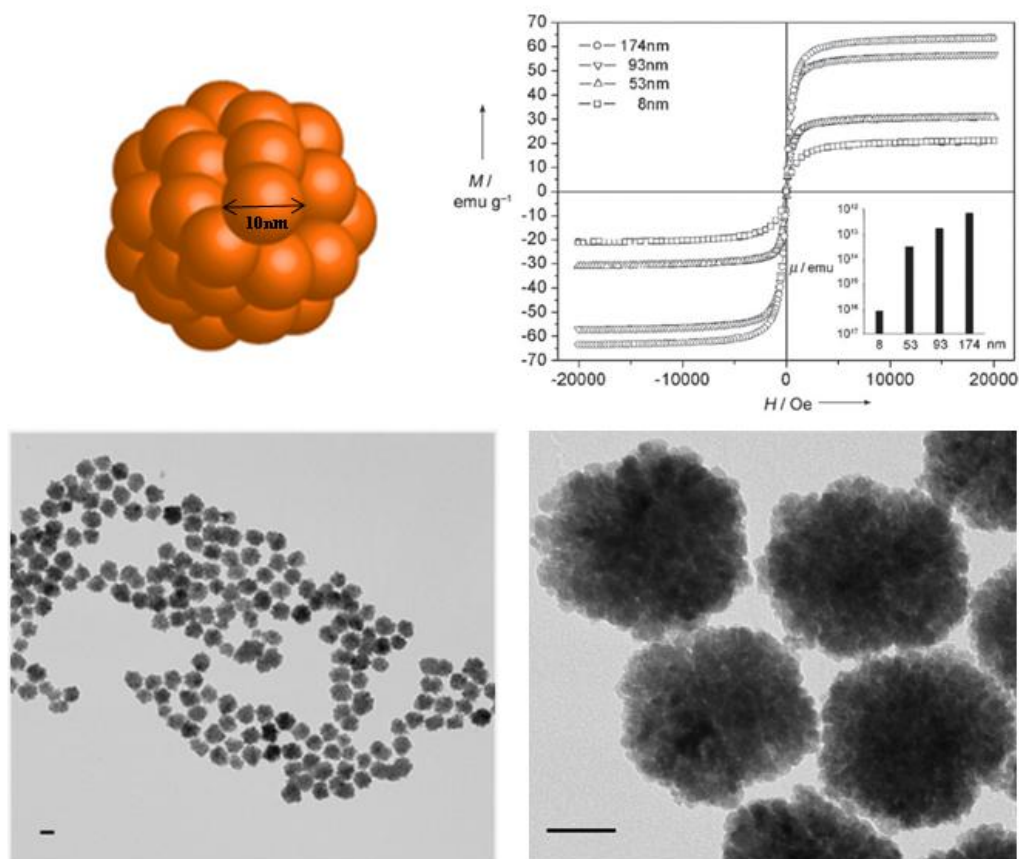

Fig 3.1 Schematic representation of a magnetic cluster and corresponding Magnetization vs field dependence after ref. 68 (top) and representative TEM images at different magnifications of Fe₃O₄ nanoclusters synthesized in our laboratories (bottom). Scale bars are 50 nm

Several robust approaches have been developed for synthesizing magnetic spinel ferrite clustering nanocrystals with tightly controlled size distribution, typically by organometallic processes at elevated temperatures in non polar solvents.[70] Additional steps of surface modification with hydrophilic material or lipid encapsulation are usually request to transfer the hydrophobic nanocrystals from apolar solvent to water for biological applications.[71]

In this work, we take advantage of the potential of clusters in engineering novel functional materials by combining into the secondary cluster structures primary nanoparticles with different functionality, and to investigate the potential occurrence of novel properties not present in the original constituents due to interactions between neighbouring nanoparticles.

In particular, we have made use of a high temperature hydrolysis procedure originally proposed by Yin and coworkers for the preparation of magnetite clusters, to explore the possibility to fine tune the functional properties of the magnetic clusters by varying its composition. In particular, we have doped the iron oxide clusters with noble metals (Au, Ag,

Pt) as well as magnetic species (Mn) with the aim to develop novel materials as biomedical tools.

Paragraph 3.1 will provide details on the procedure adopted for cluster preparation, whereas in the following paragraphs the results on the physico-chemical characterization and investigation of the potential use of the developed clusters in MRI and hyperthermia are presented.

3.1 Method of fabrication of magnetic nanoclusters based on iron oxide

Individual iron oxide magnetic nanoparticles can now be achieved with a high degree of control over size, shape and surface properties thanks to rapid progress in colloidal nanostructure synthesis. [15]

On the other hand, design of magnetic nanoclusters is intrinsically more complex due to the required control over both the parameters affecting the formation of primary nanoparticles and directing their assembly into the secondary cluster structure. Fabrication of magnetic nanoclusters typically occur according to two different approach: one "direct" process, which integrate the synthesis of nanoparticles and their aggregation into clusters in a single step, such as thermolysis, solvothermal and microwave methods; a second "multi-step" process, which first produce nanoparticles with desired size, shape and surface functionality and then assemble them into clusters of designed configurations, via methods such as solvent evaporation, electrostatic attraction or interfacial tension. While the first ones are more efficient at producing cluster nanostructures, the multi-step processes have the advantage of being more flexible and universal for organizing nanoparticles of a large variety of materials into nanoclusters with highly configurable structures. [69]

Here, we will describe in detail the one-step thermolysis approach used to synthesize doped ferrite nanoclusters investigated in this work.

In particular, the synthetic protocol was first proposed by Yin and coworkers for the fabrication of Fe_3O_4 nanoclusters and relies on thermolysis process in which the reagents (typically precursors, organic capping ligands and solvents) are mixed in liquid phase at high temperature.

The growth of these clustering nanoparticles by Yin approach follows the classic La Mer model, in which primary nanoparticles are favoured by a temporally discrete nucleation event (induced by thermolysis of the precursors) followed by slower controlled growth on the existing nuclei. [72] Further growth of nanocrystals is dominated by the well-known Ostwald ripening process in which small nanocrystals dissolve as a result of their high surface energy and the material is subsequently deposited again on the larger nanocrystals.

A key role is associated to the capping ligands, which bind to the nanoparticle surfaces, limit their growth and prevent interparticle agglomeration through steric interactions. In order to promote clusters formation, the appropriate concentration of capping ligands, which is not enough to protect the primary nanoparticles against aggregation but sufficient to stabilize the resulting 3D nanostructures, should be maintained. The formation of relatively large crystalline clusters proceeds through the 3D oriented attachment of primary nanoparticles.

As a high reaction temperature is required to directly synthesize nanocrystals with high crystallinity and narrow size distribution, suitable solvents and thermally stable capping ligands with suitable functional groups such as polyhydric alcohols and glycols must be used. In our work, we made use of Poly(acrylic acid), PAA, and Diethylene glycol, DEG, whose structural formula is depicted in Figure 3.2, as solvent and capping agent,

respectively. In particular, DEG is an hygroscopic liquid selected for its high boiling point (260 °C), being the high temperature a key parameter for high monodispersity of resulting clusters.
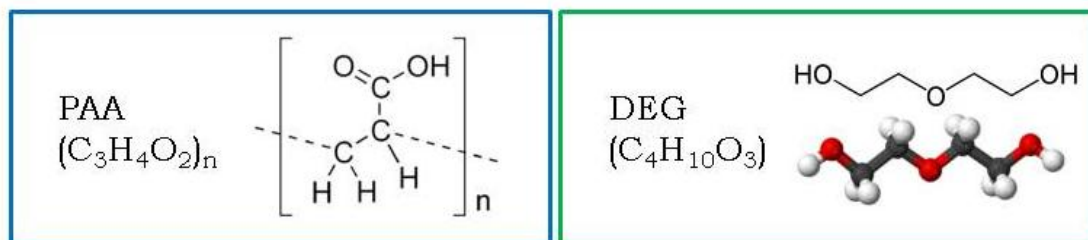

Fig. 3.2 Structural formula of PAA (left) and DEG (right).

In this work, we have developed a synthesis for the production of doped iron oxide magnetic clusters with metal or magnetic ions based on the original procedure proposed by Yin for pure magnetite.[68]

The overall preparation procedure is depicted in Figure 3.3 and can be described as follows: in a 25 mL two neck flask connected to a Schlenk line under N_2 flow, 50 mmol of sodium hydroxide (NaOH, anhydrous, >98%, Sigma Aldrich) are mixed in 20 mL of Diethylene glycol (DEG, 99.5%, Fisher Scientific) under vigorous stirring. This solution is heated first to 120 °C for 1 hour while refluxing, then cooled at 70 °C.

In a 50 mL flask, the metal precursors (0.8 mmol) and polyacrylic acid (PAA, 1800 g/mol, Sigma Aldrich) (8 mmol) are added in a 34 mL DEG and heated under N_2 flow up to 220 °C. When the temperature of the second solution is stabilized to 220 °C, rapidly 3.4 mL of the NaOH /DEG solution at 70°C are injected in a single shot.

Note that the used metal precursors are Iron (III) chloride (anhydrous, 99.99%, Sigma Aldrich), Pt II Chloride (98% Sigma Aldrich), silver nitrate (99.9%, Fisher Scientific), sodium tetrachloroaurate (III) dihydrate (99%, Sigma Aldrich).

A few minutes after injection, the sudden turn to black shows that the growth of magnetic nanoclusters has started (Fig. 3.3). After 1 hour the reaction was quenched and the solution cooled to room temperature.

The resulting product was purified one time upon ethanol addition to the reaction product at room temperature, separated by centrifugation at 6500 rpm for 15 min, the further times washed again and again with a mixture of milliq water and ethanol. Finally, the vial containing the sample was subjected to magnetic separation for 24 hours and the resulting magnetic nanoclusters could be dispersed in pure milliq water. The purification step is fundamental to obtain a fine product of synthesis because help to remove the robust surface coating of organic surfactant and to decrease the ionic strength, ensuring highly dispersibility in water.

Once they are cleaned, the nanoclusters can be dispersed in water and remain stable in solution for at least several months.
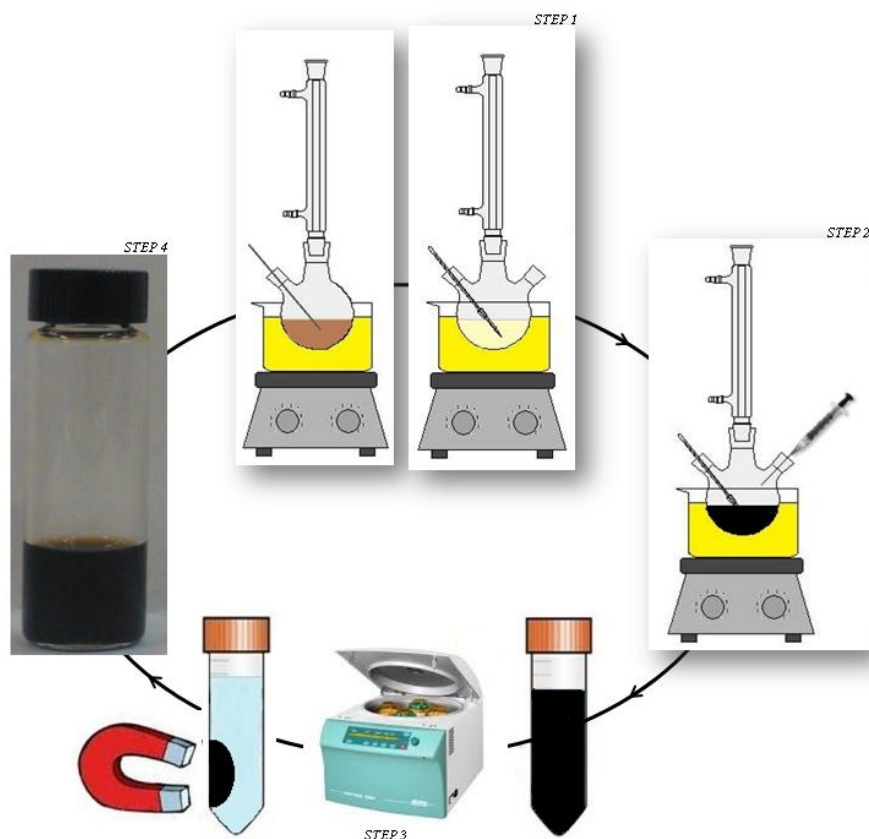
Figure 3.3 Synthetic scheme used to produce magnetic nanoclusters. Preparation of stock solution and main solution under inert atmosphere (step 1); fast injection of stock solution into the main solution by single shot (step 2); washing, purification step and magnetic separation (step 3); dispersion in deionized water of final product of reaction (step 4).

The mechanism of formation of nanoclusters by this approach has been rationalized for the case of pure iron oxide nanoparticles and assumes that introduction of sodium hydroxide into the hot mixture of DEG, PAA and metal precursors produces water molecules and increases the alkalinity of the reaction system, and both results promote the hydrolysis of the chloride. Under the reductive atmosphere provided by DEG at high temperature, $Fe(OH)_3$ partially transforms into $Fe(OH)_2$ and finally Fe_3O_4 particles are formed through dehydration. Under optimized conditions, such Fe_3O_4 nanocrystals spontaneously aggregate to form flowerlike three-dimensional clusters.

Direct formation of water-dispersible nanoparticles is a major advantage associated to this synthetic route, as opposed to colloidal routes which result in hydrophobic nanocrystals, and is of particular interest in view of prospective biomedical applications, as it is the scope of this work.

It should be pointed out that the macroscopic behaviour of all the synthesized materials suggests the occurrence of superparamagnetic properties: in the absence of an external magnetic field the nanoclusters dispersed well in solution; they readily respond when exposed to an external magnetic field, and this behaviour is reversible.

In the following paragraphs the characterization of the novel doped iron oxide-based magnetic nanoclusters will be presented.

3.2 Characterization of metal-iron oxide nanocluster heterostructures

The prepared metal-iron oxide heterostructures were characterized by a multitechnique approach, involving in particular the use of electron microscopies in order to gain insights on the morphology of the product obtained under the adopted conditions.

TEM investigation, reported in Figure 3.4, provided evidence that all the samples are made out of clusters with a round-like shape and quite homogeneous size, and that no isolated nanoparticles are observed. Closer inspection at the cluster morphology through imaging at higher magnification, points out the occurrence of darker spots within individual clusters, which can be ascribed to the occurrence of the metals. This effect is particularly evident in the Pt-Fe$_3$O$_4$ sample.

Statistical analysis of the TEM images was performed in order to obtain the size distribution data for the clusters, reported in Figure 3.4. It was found that while size distribution is similar for all the samples, the average cluster size is slightly smaller for the Pt-Fe$_3$O$_4$ sample (53 nm) than for the Ag-Fe$_3$O$_4$ sample (68 nm) and Au-Fe$_3$O$_4$ sample (75 nm).
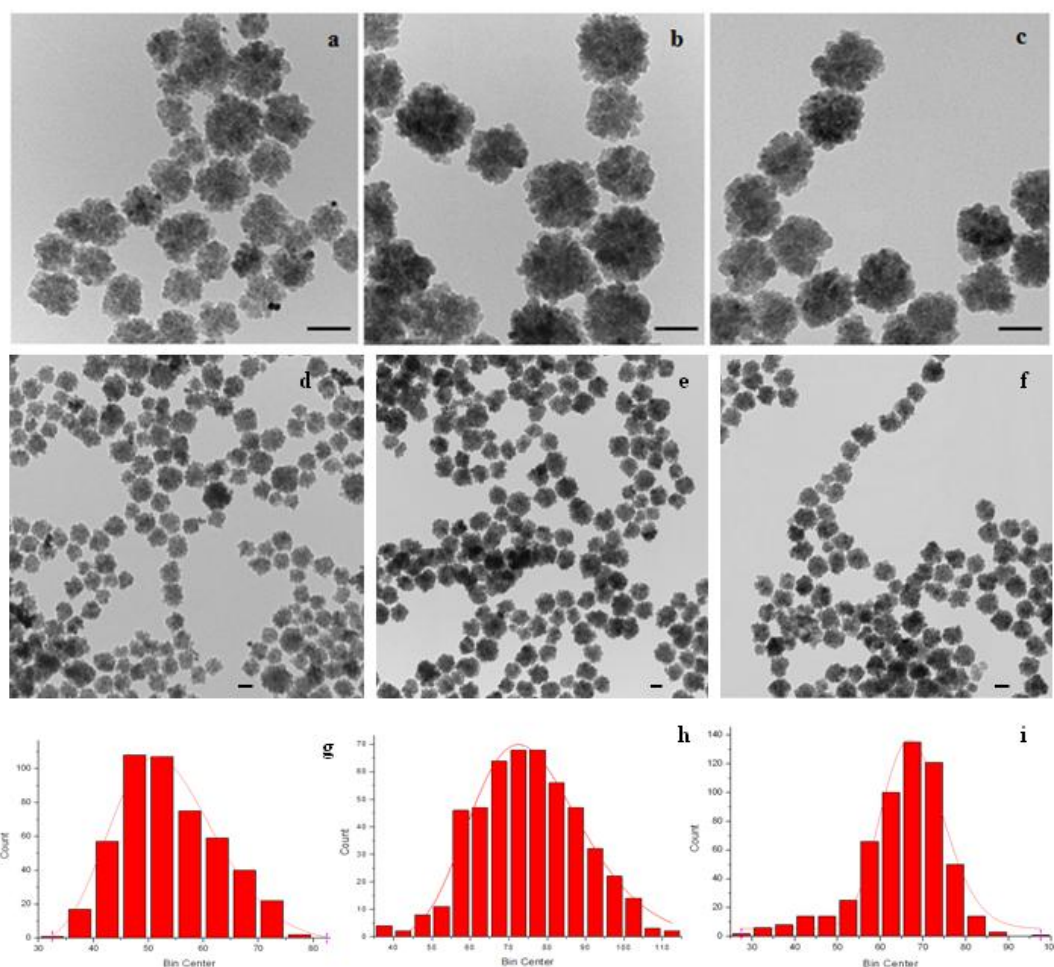

Fig 3.4. TEM micrographs of Pt-Fe$_3$O$_4$ (a,d) Au-Fe$_3$O$_4$ (b,e) Ag-Fe$_3$O$_4$ (c,f) metal doped nanoclusters. All scale bars are 50 nm. In the bottom, size distribution of Pt-Fe$_3$O$_4$ (g) Au- Fe$_3$O$_4$ (h) Ag-Fe$_3$O$_4$ (i) metal doped nanoclusters calculated by statistical analysis by TEM .

To gain further informations on the three-dimensional morphology of the clusters, the samples were characterized through scanning electron microscopy (SEM). As shown in Figure 3.5, SEM results support TEM data, i.e. all the samples show the occurrence of

flower-like rounded clusters with size in the range 40-90 nm and with average size which increase in the order Pt/Ag/Au. In the case of the Ag-Fe_3O_4 and Au-Fe_3O_4 samples, large particles were also observed (data not shown). SEM was also used to collect elemental mapping (see insets), which clearly indicates both the occurrence of Fe and of the noble metals in the clusters.
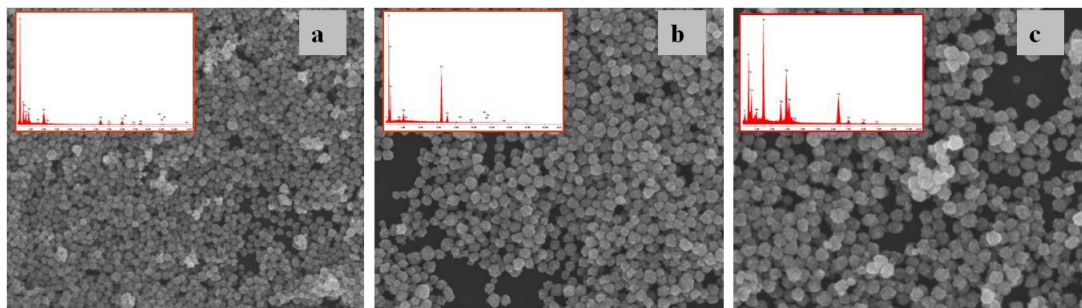

Fig.3.5 SEM images of Pt-Fe_3O_4, Au-Fe_3O_4, Ag-Fe_3O_4. In the inset, elemental mapping at the microstructural level by scanning electron microscopy (SEM) with energy dispersive X-ray spectrometry (EDS)

To obtain quantitative information of the composition of the clusters, chemical analysis was performed by means of ICP-MS. The results further support that noble metals have been incorporated into the clusters and provide the following compositional data, expressed as a mass ratio between iron and noble metal: 4.5 (Pt-Fe_3O_4); 9.7 (Au-Fe_3O_4) and 14.8 (Ag-Fe_3O_4).

To gain insights on the location of the metals in the heterostructures, scanning transmission electron microscopy (STEM) characterization was performed, as shown in Figure 3.6. In these images, the bright contrast can be ascribed to both thickness and compositional effects. The occurrence of bright spots, with particular reference to the Pt-Fe_3O_4 sample, can be reasonably ascribed to noble metal nanoparticles with comparable size to the iron oxide primary particles, which are randomly distributed within the clusters.
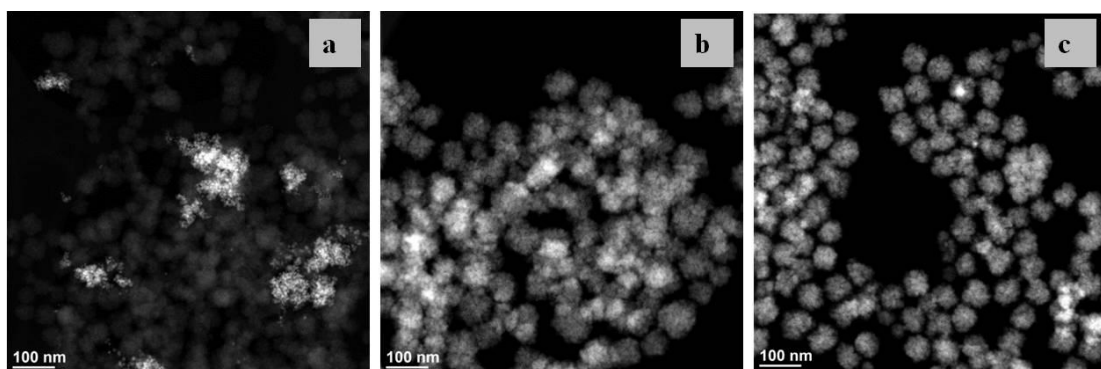

Fig 3.6 STEM images of a) Pt-Fe_3O_4, b) Au-Fe_3O_4, c) Ag-Fe_3O_4 metal doped nanoclusters

The structure of the clusters was investigated by XRD and compared to pure iron oxide clusters prepared as a reference (Fig. 3.7). XRD patterns of all samples exhibit the typical reflections of the iron oxide spinel structure (PDF card 19-0629). In the noble metal-iron oxide clusters, additional diffraction peaks can be observed which can be ascribed to the expected metal phase, i.e. fcc-Pt (PDF card 4-802), fcc-Au (PDF card 4-784) and fcc-Ag (PDF card 4-783).

Line broadening, however, points out that in the case of Au-Fe$_3$O$_4$ and Ag-Fe$_3$O$_4$ nanoclusters a contribution from very large metal crystals is also present. In particular, the average crystal size of primary iron oxide and metal nanocrystals within the clusters were calculated by the Debye-Scherrer formula. The crystal size of primary iron oxide particles calculated from the (311) peak was 10 nm for pure Fe$_3$O$_4$ and 11.5 nm for Pt-Fe$_3$O$_4$, 13.8 nm for Au-Fe$_3$O$_4$ and 11.8 nm for Ag-Fe$_3$O$_4$ nanoclusters. Meaning that the size of constituent iron oxide nanocrystals grows therefore with the same trend as the overall cluster size. On the other hand, the average crystal size of the metal domains is 9 nm for Pt and larger than 100 nm for Au and Ag.
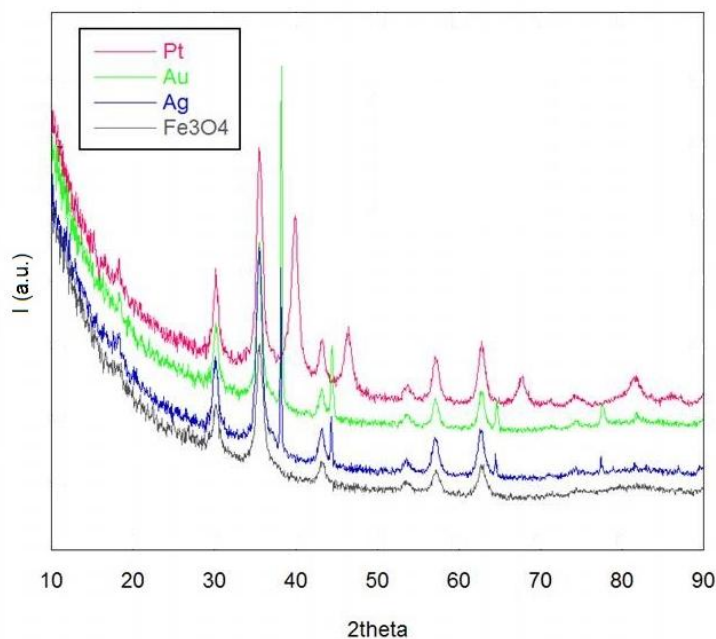

Fig 3.7. X-Ray powder diffraction pattern for Pt-Fe$_3$O$_4$ (pink), Au-Fe$_3$O$_4$ (green), Ag-Fe$_3$O$_4$ (blue) metal doped nanoclusters compared with pure magnetite nanoclusters synthesised with the same approach. The peaks more intense are zoomed in the inset: for Pt at 39.91°, Au at 38.22° and Ag at 38.14°

An important feature of the developed heterostructures relates to their high dispersibility in water. Further insights on the features of the metal-Fe$_3$O$_4$ were obtained by DLS measurements (see Figure 3.8). The average hydrodynamic diameter is 65 nm, 80 nm and 77 nm for the Pt-Fe$_3$O$_4$, Au-Fe$_3$O$_4$ and Ag-Fe$_3$O$_4$ respectively, in agreement with TEM data; furthermore, the polydispersity index (PDI) has been always below 0.2 value, ensuring high monodispersity of resulting heterostructures.
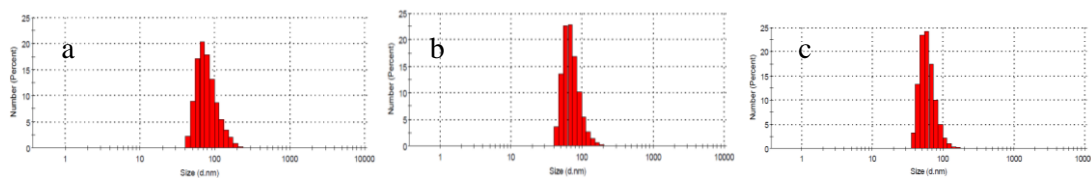

Fig.3.8. Size distribution calculated by DLS respectively for a) Pt-Fe$_3$O$_4$ b) Au- Fe$_3$O$_4$, c) Ag-Fe$_3$O$_4$ metal doped nanoclusters.

The multitechnique physico-chemical characterization performed on the cluster heterostructures clearly demonstrates that the used procedure is effective in incorporating metal nanoparticles within the cluster of iron oxide nanoparticles, although in the case of gold and silver larger metal nanocrystals are also formed. The main features of the developed materials are summarized in Table 3.1.

56

SAMPLE	ICP-MS				DLS	TEM	XRD
	Fe (g/L)	Fe%	Pt, Au,Ag (g/L)	Pt,Au, Ag %	SIZE (nm)	SIZE (nm)	SIZE (nm)
Fe_3O_4	4.23	/	/	/	84±28 (PDI 0.12)	68±10 (330 counts)	10
$Pt@Fe_3O_4$	5.436	82	1.2	18	81±28 (PDI 0.21)	53±9 (488 counts)	12
$Au@Fe_3O_4$	2.166	91	0.22	9	82±22 (PDI 0.07)	75±14 (494counts)	14
$Ag@Fe_3O_4$	3.281	94	0.22	6	67±17 (PDI 0.07)	68±10 (559 counts)	12

Table 3.1 Report of the main compositional and morphological data of metal-nanoclusters heterostructures.

3.3 Application of Pt-Fe₃O₄ cluster heterostructures

The ability to selectively arrange nanosized domains of different materials into a single hybrid nanoparticle offers an intriguing route to engineer nanomaterials with multiple functionalities or the enhanced properties of one domain. Recently, several groups have devised innovative syntheses of heterostructures through which they have been able to group inorganic nanomaterials with different properties in the same particle.

For example, on core@shell nanostructures prepared by selectively doping ferrite phases, the coupling between the magnetically soft shell and magnetically hard core led to unprecedented hyperthermic potency, which could potentially improve magnetically based cancer therapy. However, doping nanoparticles with potentially toxic metals raises important concerns regarding their fate in the organism.

On the other hand, iron oxide as well as noble metals are considered to have limited adverse effects on human health and are therefore preferred for biomedical applications.[73]

The metal-Fe_3O_4 cluster heterostructures developed in this work are promising tools for application in biomedicine, owing also to their dispersibility at relative high concentrations in water. In particular, in collaboration with the group of Dr T. Pellegrino at IIT in Genova, we have test the potential of the Pt-Fe_3O_4 nanocluster, which shows the most controlled microstructural features, as a contrast agent for diagnosis through MRI. To this end, the longitudinal and transverse ^1H relaxation rates were measured at different fields used in medical imagers, i.e. 0.5 T, 1 T and 1.5 T (Fig.3.9).
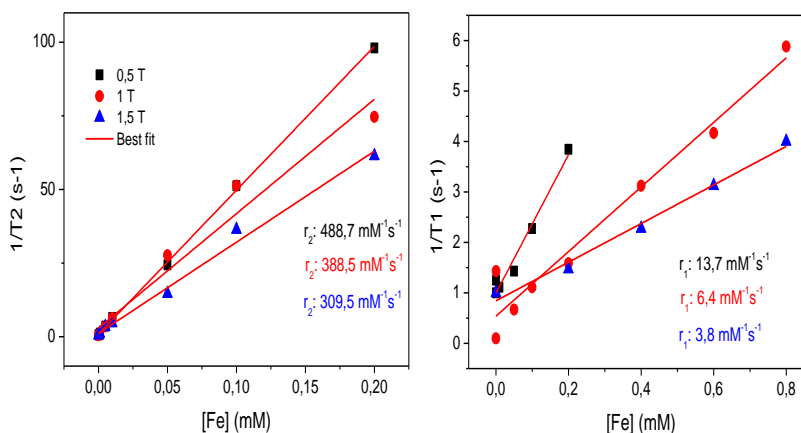

Fig. 3.9 Relaxivity data of Pt-Fe₃O₄ magnetic nanoclusters

SAMPLE	r_1 (mM^{-1}s^{-1})			r_2 (mM^{-1}s^{-1})			r_2/r_1		
	0.5 T	1 T	1.5 T	0.5 T	1 T	1.5 T	0.5 T	1 T	1.5 T
Pt-Fe$_3$O$_4$	14	6.4	4	489	389	310	35	60	78
Fe$_3$O$_4$	8.3	4.7	3.7	433	275	161	52	58	43.5

Table 3.2 The comparison between relaxivity data of pure Fe$_3$O$_4$ and Pt-Fe$_3$O$_4$ magnetic nanoclusters

The relaxation rates are summarized in Table 3.2 and compared to pure Fe$_3$O$_4$ cluster prepared as a reference. The obtained data indicate that the Pt-Fe$_3$O$_4$ nanoclusters improve proton relaxation rates, and in particular induce both higher longitudinal and transverse relaxation rates as compared to pure Fe$_3$O$_4$ nanoclusters. As expected, the superparamagnetic clusters mainly increase the transverse relaxation rate and are expected to behave as negative contrast agents, i.e. to enhance the dark signal of the MR images. The transverse relaxation rate is larger for the Pt-Fe$_3$O$_4$ nanoclusters with respect to pure Fe$_3$O$_4$ nanoclusters at all the investigated field values; in particular, at high fields doping the Fe$_3$O$_4$ nanoclusters produces nearly a two-fold improvement of the efficiency. The relative ratio between the transverse and longitudinal relaxation rates is also reported in Table 3.2, as this parameter has been often associated to the image contrast efficiency of a contrast agent. By taking a look at the r_2/r_1 values for the doped and pure Fe$_3$O$_4$ nanoclusters, it can be pointed out that at low fields the un-doped clusters exhibit higher values, whereas at high fields the doped clusters are likely to have a much better contrast efficiency. These results reveal that the introduction of a relatively limited amount of Pt nanoparticles within the iron oxide clusters significantly affects the relaxometric properties of the resulting cluster.

Superparamagnetic Fe$_3$O$_4$ nanoparticles are perfect examples of so-called *theranostic agents* because of their ability to be used both in diagnostic imaging techniques and as therapeutic tools.[74] In particular, as discussed in Paragraph 1.3.3, when submitted to an alternating field, magnetic nanoparticles may act as heat mediators that can be used for hyperthermic cancer treatment, for thermally activated drug release or for remote activation of cell functions.[75]

Within this framework we have investigated the ability of the synthesized Pt-Fe$_3$O$_4$ nanoclusters to enhance the heating power measured by the specific absorption rate, SAR. Figure 3.10 shows the SAR values measured for the Pt-Fe$_3$O$_4$ nanoclusters.
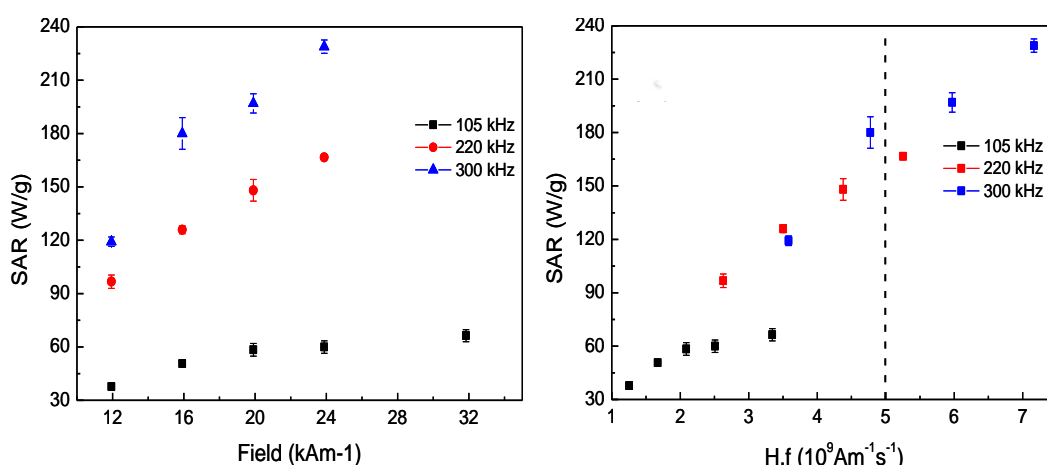

Figure 3.10 SAR values for the Pt-Fe$_3$O$_4$ nanoclusters

It was found that at the conditions suggested for clinical therapy (H·ν ~ 5 ·10^9 A·m^{-1}·s^{-1}) the SAR value in Pt-Fe$_3$O$_4$ nanoclusters is 230 W/g, as compared to 150 W/g for pure Fe$_3$O$_4$ nanoclusters.

These results indicate that the design of Pt-Fe_3O_4 nanocluster heterostructures has enabled to prepare novel theranostic tools for biomedical imaging and therapy.

Finally, it should be pointed out that noble metal-iron oxide heterostructures may have great potential also in many diverse fields.

For example, gold-decorated magnetic nanoparticle clusters, in a range of possible sizes from 20 to 150 nm, were used for generation of "hot spots" to significantly enhance the Raman scattering from analytes, because of the assembly of plasmonic nanoparticles into secondary structures that may induce near field electromagnetic coupling of surface plasmons between adjacent particles. Also, detailed NMR relaxation analysis demonstrates that the effect of the gold NPs on the interaction between bulk solvent and the magnetic moments of the cluster is minimal and that the clusters remain superparamagnetic in nature.[69,76]

In addition, superparamagnetic iron oxide nanoclusters can be directly employed for constructing colloidal photonic crystals, that is, crystalline lattices in which a photonic band gap appears as the result of cooperative scattering of light from an ordered array of dielectric particles.[77] Photonic crystals properties based on nanostructured materials show highly tunable stop bands that can be moved across the entire visible spectral region owing to the highly charged polyacrylate-capped surfaces and the strong interaction of the magnetite clusters with a magnetic field. Yin and co.[78] employ simple and inexpensive synthetic methods and yields photonic crystals with wide and reversible tunability, and an instant response to external magnetic fields interesting for their promise in optoelectronic applications (lasers, sensors).

With this aim, our approach to assembly noble metal nanoparticles and magnetic iron oxide into the same heterostructure, that led to iron oxide nanoclusters decorated with platinum, gold and silver, may open up the possibility to investigate new properties for a technological application in optical devices. Noble metal nanoparticles are an excellent candidate for this study because they are easily detectable by optical spectroscopy and can be used as a model system for other inorganic nanoparticles. As a result, the combined effect of these two domains could lead to enhance plasmonic and chemical functionality to the resulting heterostructures and improve the physical robustness and processability of the suspensions. Also, the fast and reversible response suggests great potential of these photonic materials in applications such as displays and sensors.

3.4 Characterization of Mn-doped magnetic iron oxide nanoclusters

As an alternative route to tune the properties of pure Fe_3O_4 nanoclusters, doping with magnetic species such as manganese was attempted.

The spinel structure of Fe_3O_4 (which may be regarded as $FeO \cdot Fe_2O_3$), as detailed in Paragraph 1.2.2 is also shared by several substituted magnetic ferrites with general formula MFe_2O_4, where M can be a divalent ion such as Mn, Zn, Ni, Co. The similar crystallochemistry of the ferrites with different ion doping, and the ease of formation of both stoichiometric and non-stoichiometric ferrites, opens up the possibility to make the preparation of magnetic clusters a versatile route for the fabrication of materials with tunable composition and magnetic properties.

In this work we have focused on Mn-doping as this ion is relatively less toxic in view of biomedical applications. In order to investigate the properties of the $Mn_xFe_{3-x}O_4$ clusters, the composition of the nanoclusters was controlled by varying the ratio of $MnCl_2/FeCl_3$

precursors, while the PAA amount, the reaction volume and overall ion concentration was kept fixed for all experiments.

Following the synthetic procedure of synthesis reported in Paragraph 3.1, samples with different Fe:Mn ratio were prepared. In all synthesis, however, substoichiometric amounts of Mn were adopted, as our aim was to develop new magnetic tools for biomedicine and therefore to investigate the minimum doping required for a significant modulation of the magnetic properties with minimal effect on particle toxicity.

In particular, Table 3.2 reports the data on three selected samples which cover the range of investigated relative amounts of Fe and Mn precursors, together with the chemical analysis results as obtained by ICP-MS. These analysis supports that manganese doping was effectively achieved, and in particular the amount of manganese was varied from a low doping (3%), medium doping (6%), high doping (13%).

Sample	$(Fe:Mn)_{TH}$	% Mn_{EXP}	$<d>_{XRD}$ (nm)	$<D>_{TEM}$ (nm)	$<D_H>_{DLS}$ (nm)
FeMn_L	8	3	11	67± 8	68± 18
FeMn_M	15	6	12	72±12	111± 58
FeMn_H	18	13	11	135 23	118± 28

Table 3.2 Chemico-physical properties of $Mn_xFe_{3-x}O_4$ clusters synthesized with low, medium and high relative Mn doping: theoretical Fe:Mn ratio based on the amount of starting precursors; experimental Mn content as obtained by ICP-MS; average crystal size of the primary nanocrystal calculated from XRD, average size of the clusters determined by TEM and hydrodynamic size of the clusters obtained by DLS and averaged by number.

XRD was used to investigate the structure of the synthesized materials, as reported in Figure 3.11 for the $Mn_xFe_{3-x}O_4$ clusters synthesized with low, medium and high relative Mn doping. All the samples exhibit reflections which can be attributed to the spinel ferrite phase. The broadening of the peak profile is in agreement with the occurrence of nanocrystalline primary particles. In particular, average size calculation from the Debye-Sherrer formula provides average crystal size in the range 11-12 nm, as summarized in Table 3.2.
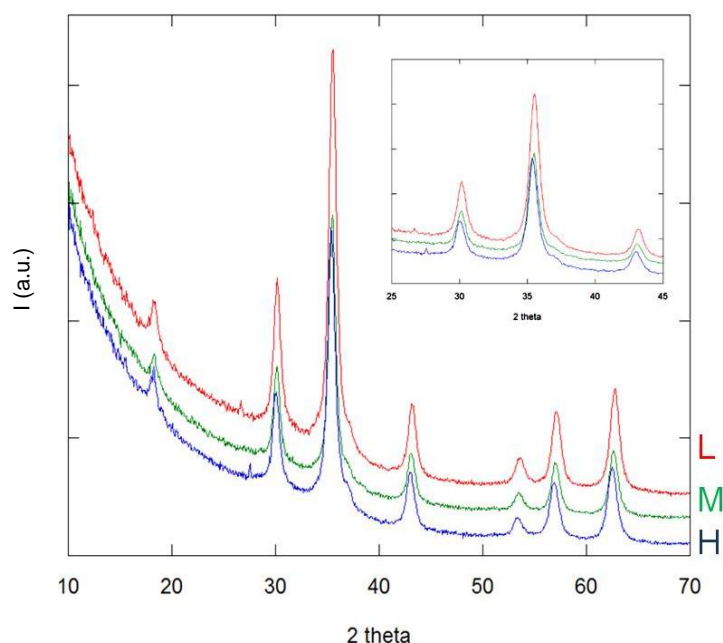
FIG 3.11 XRD patterns of the $Mn_xFe_{3-x}O_4$ clusters synthesized with low (red), medium (green) and high relative (blue) Mn doping. In the inset it is possible observe that the patterns are shifted slightly to lower angles by increasing amount of Mn doping in the composition.

The position of the diffraction peaks is slightly different for the samples with different degree of Mn doping and from the stoichiometric crystalline $MnFe_2O_4$. In particular, X-Ray diffraction data of $Mn_xFe_{3-x}O_4$ samples show a pattern that has peak positions intermediate between the pure magnetite Fe_3O_4 (PDF card 19-0629) and the stoichiometric $MnFe_2O_4$ (PDF card 10-0319): in particular, as shown in the simulated XRD patterns of Fe_3O_4 and stoichiometric $MnFe_2O_4$ calculated from the corresponding PDF cards reported in Figure 3.12, peak positions are shifted at lower angular values in the case of $MnFe_2O_4$.
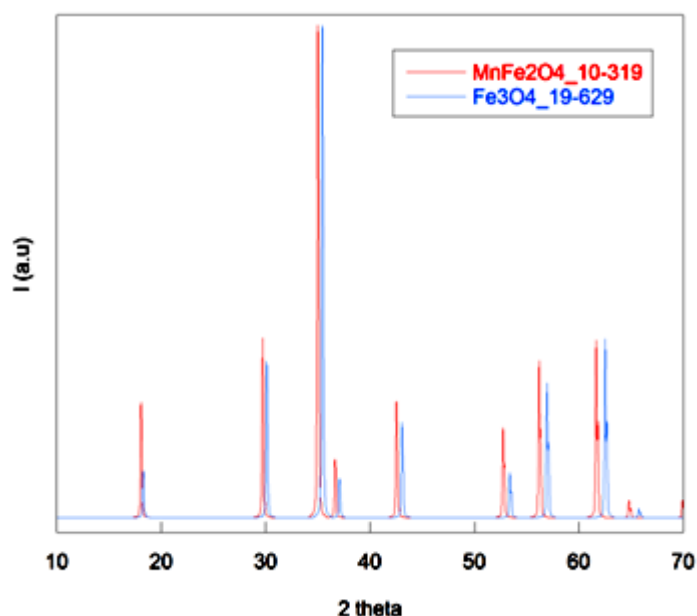

Fig 3.12 Simulated pattern for Manganese Ferrite (card 10-319) and Iron oxide (card 19-629)

In agreement with the expected trend, the patterns of $Mn_xFe_{3-x}O_4$ samples are shifted slightly to increasingly lower angles for samples with increasing amount of Mn doping in the composition.

XRD data support therefore the formation of substoichiometric nanocrystalline primary particles made out of manganese ferrite. In should be pointed out, however, that XRD cannot provide final conclusions on the location and oxidation state of Mn, which requires the use of spectroscopic techniques such as X-ray absorption spectroscopy. To this end, a proposal for EXAFS characterization of these doped cluster has been submitted.

The synthesized clusters are highly dispersible in aqueous media and were characterized by DLS to determine the hydrodynamic cluster diameter. As reported in Table 3.2, it was found that the size of the cluster is significantly different for the samples with different Mn content. It should be pointed out that (data not shown) the hydrodynamic diameter was found to vary in a non linear way with the degree of Mn doping, and the role of the purification steps in inducing some size sorting effect cannot be ruled out. Therefore, the variation of the cluster size cannot be ascribed unambiguously to the effect of Mn doping.

TEM images of the $Mn_xFe_{3-x}O_4$ samples, reported in Fig 3.13 shows that the samples preserve the flower-like round morphology of the pure iron oxide clusters. In addition, cluster size analysis performed through statistical analysis of the images clearly shows that the average cluster size differs significantly in the samples with different Mn doping, in agreement with DLS results, as summarized in Table 3.2.
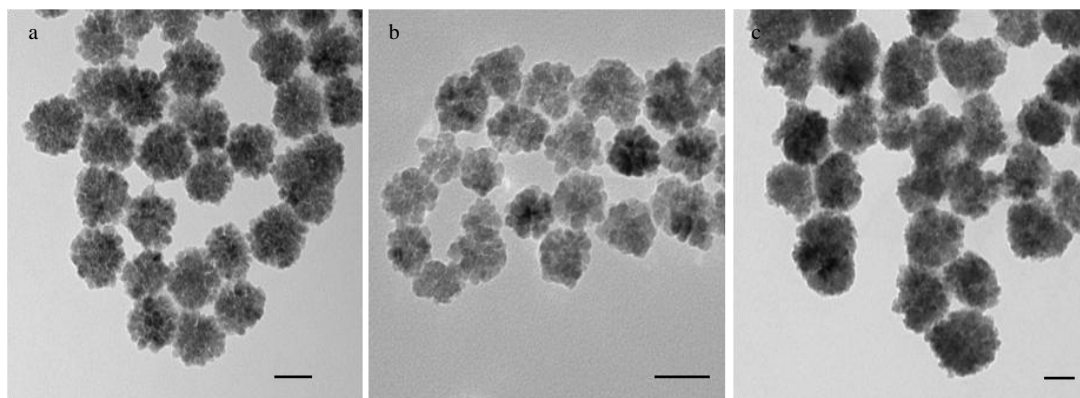

Fig.3.13 Representative TEMs of Mn$_x$Fe$_{3-x}$O$_4$ samples with low (a), medium (b) and high doping (c).

Further investigation by High resolution TEM (HR-TEM) indicates that the arrangement of the Mn-doped nanoparticles is very similar to the secondary structure reported for pure Fe_3O_4.

In particular, as shown in Fig 3.14 the primary nanocrystals tend to join together with a common crystallographic orientation to form the cluster, which reflects in the continuity of the crystal lattice at the grain interfaces can be clearly observed.

In particular, HR-TEM images of each sample clearly show superlattice fringes, suggesting that the nanoparticles were rearranged into a monocrystalline face centered cubic (fcc) structure (fcc) after annealing, oriented along the [001] zone axis. This suggests that individual cores have rotated during the ripening phase at high temperature to share the same crystal orientation, minimizing their surface energy. [75]
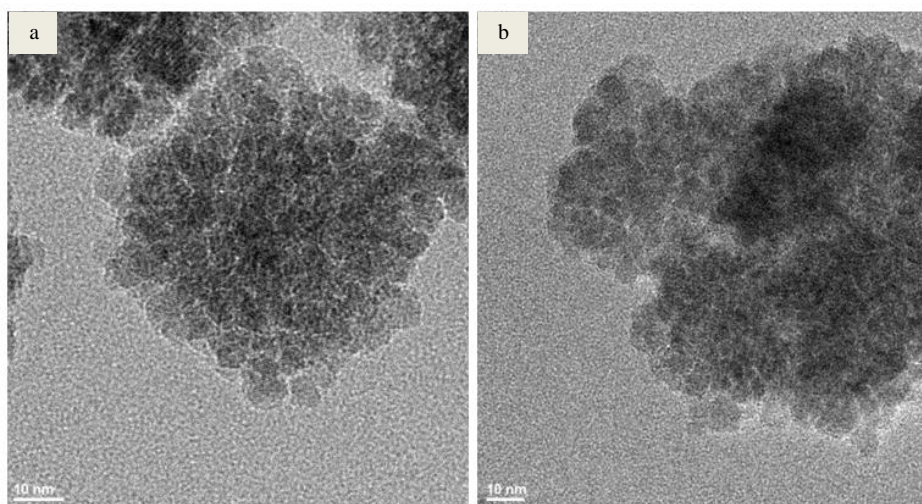
Fig. 3.14 HRTEM images of $Mn_xFe_{3-x}O_4$ clusters with medium doping (b) compared with pure Fe_3O_4 (a) cluster nanoparticles.

Finally, it should be pointed out that EDX was used to obtain compositional information al the nanoscale. EDX results were in perfect agreement with ICP-MS data, suggesting compositional homogeneity of the clusters.

The physico-chemical features of the synthesized clusters indicate that the adopted procedure is a successful strategy to tune the composition and properties of magnetic clusters by controlled doping. Due to the rich chemistry of spinel ferrites, we anticipate that this method could represent a versatile route for the design of substituted ferrites with tunable properties.

3.5 Prospective application of Mn-doped magnetic nanoclusters in biomedicine

The physico-chemical features of the prepared $Mn_xFe_{3-x}O_4$ nanoclusters suggest that they may act as valuable tools for biomedical applications. In particular, a significant advantage of the adopted procedure is that water-dispersible clusters are obtained in high yield, without the need of time consuming phase transfer steps. This aspect is of particular relevance in view of application in magnetic hyperthermia, which requires relatively concentrated (5 mg/mL) dispersion of magnetic nanoparticles.

In this work, we have made use of SQUID magnetometry, ^{1}H relaxometry and SAR measurements to investigate the potential of the developed $Mn_xFe_{3-x}O_4$ nanoclusters in diagnosis through MRI and therapeutics magnetic fluid hyperthermia.

Magnetic measurements on all $Mn_xFe_{3-x}O_4$ nanoclusters indicate that the particles are superparamagnetic at room temperature, meaning that the thermal energy can overcome the anisotropy energy barrier of a single particle and the net magnetization of the particle assemblies in the absence of an external field is zero.

It was also found that all the samples are able to enhance the nuclear relaxation rates; these samples shown to be potentially active both as MRI contrast agents and heat mediators in magnetic hyperthermia. At present, however, it is not possible to establish a direct correlation between the functional properties of $Mn_xFe_{3-x}O_4$ nanoclusters and the Mn content, as a concomitant variation of the cluster size which may also affect the relaxometric and hyperthermic properties is observed.

The best SAR values and relaxometric properties were obtained for the sample with a Mn doping of 11% as respectively shown in Table 3.4 and 3.5. In addition, the main features of the best Mn-doped iron oxide cluster are summarized in Table 3.3

% Mn exp	$<d>_{XRD}$ nm	$<D>_{TEM}$ nm	$<D_H>_{DLS}$ nm	M_{sat}@310 K emu/g	M_r@310 K emu/g	M_r/M_{sat}	Hc @310 K Oe
11	14	50±6	43±11	33	6	0.2	29

Table 3.3 Chemical, morphological and magnetic features of the most promising $Mn_xFe_{3-x}O_4$ sample with 11% in Mn

In particular, the sample is made out of relatively small clusters (40÷50 nm) with primary nanocrystals of around 14 nm. The magnetic properties, with particular reference to the zero field cooled (ZFC/FC) curves indicate that the sample is superparamagnetic. The hysteresis curves at body temperature are in accordance with literature data for soft magnets with crystallites in the 10÷15 nm range, where lower saturation magnetization values with respect to the bulk can be expected. [79]

Coercive fields H_C are smaller in comparison to reference values, and this effect can be attributed to the occurrence of interactions.

The hyperthermic behaviour of the sample was evaluated by determining their SAR at different applied fields. As expected, the SAR values increase with the frequency and field values. In all cases, however the SAR values are extremely high as compared to the heat mediators proposed so far in the literature.

FREQ. (KHz)	300				220				105			
FIELD (KAm-1)	24	20	16	12	24	20	16	12	24	20	16	12
SAR for $Mn_xFe_{3-x}O4$	390±10	385±9	352±5	261±7	287±6	253±4	233±5	179±7	112±4	103±5	95±4	71±4
SAR for Fe_3O_4	149±4	133±6	109±4	100±7	90±3	84±4	74±2	69±4	45±4	40±2	26±2	21±3

Table 3.4 SAR values of the most promising $Mn_xFe_{3-x}O_4$ sample with 11% in Mn compared to Fe_3O_4 sample synthesized with the same procedure

SAMPLE	r_1 (mM^{-1}s^{-1})			r_2 (mM^{-1}s^{-1})			r_2/r_1		
	0.5 T	1 T	1.5 T	0.5 T	1 T	1.5 T	0.5 T	1 T	1.5 T
$Mn_xFe_{3-x}O_4$	30	15	8.4	629	623	603	21	42	80
Fe_3O_4	8.3	4.7	3.7	433.5	275	161	52	58	44

Table 3.5 Relaxivity data of the most promising $Mn_xFe_{3-x}O_4$ sample with 11% in Mn compared to Fe_3O_4 sample synthesised with the same procedure

The preliminary results obtained on the developed $Mn_xFe_{3-x}O_4$ nanoclusters demonstrate that ion doping is an effective strategy for tuning the features of iron oxide-based magnetic clusters. Thanks to the wide range of magnetic ferrites available, this procedure could enable the fabrication of a wide range of novel magnetic nanomaterials.

Conclusions and future challenges

This work deals with the design, synthesis and physico-chemical characterization of functional inorganic nanocrystalline heterostructures for prospective use in energy and biomedicine.

Materials synthesis has been performed by bottom-up chemical routes in solution at high temperature which ensure high crystallinity, such as colloidal synthesis and forced hydrolysis, assisted by the use of coordinating species. Materials characterization has been performed by a multi-technique approach including XRD, TEM, EXAFS, UV-Vis spectroscopy, chemical analysis and DLS.

A relevant part of the work has been devoted to the design of heterostructures which combine a semiconducting and a metal domain, to be used as prospective photocatalysts for hydrogen production through the water splitting reaction. Recently developed branched nanocrystals made out of a CdSe core in the sphalerite polymorph and eight arms of CdS in the wurtzite polymorph departing from it were selected as semiconductor domain, and insights on the structural features of these nanocrystals which could not be obtained by conventional characterization were achieved by X-ray absorption spectroscopy. The formation of CdSe@CdS-Pt heterostructures has been successfully achieved, and in particular the experimental conditions for directing the deposition of metal tips selectively at the octapod tips or unselectively on the octapod surface have been established. Our results contribute to the understanding of the design of heterostructures based on domains with complex morphology. In addition, the developed materials can be used as model systems to investigate the dynamics of charge carriers in the metal-semiconductor heterostructures in view of application in photocatalysis. Photophysical characterization of CdSe@CdS-Pt octapod nanocrystals, both selectively tipped and unselectively covered, indicates that electron capture by Pt tips occurs in 200 ps, providing just a perturbation to the excited state dynamics, while in Pt covered nanocrystals electron capture is much faster,~ 1 ps and competes with energy relaxation and Auger recombination, causing the capture of hot electrons. Injection of multiple excitons in each nanocrystals results in the simultaneous charge separation by Pt domains of tens of electrons available for chemical reactions. The promising photophysical features of the synthesized heterostructures suggest successful application of CdSe@CdS-Pt octapods in the photocatalytic water splitting reaction. To this end, based on the tendency of pure CdSe@CdS octapods to spontaneously self-assemble into three-dimensional superstructures, we expect that CdSe@CdS-Pt heterostructures could be successfully deposited on substrates to create nano-sized metal-semiconductor film devices on a scale compatible with practical applications.

Another major topic of this research has been the design of three-dimensional clusters obtained by assembly of primary superparamagnetic iron oxide nanoparticles where controlled doping through either magnetic ions or noble metals could be introduced. Manganese doping of the iron oxide cluster was successfully achieved, and it was demonstrated that this resulted in enhanced efficiency as contrast agent for MRI as well as

improved heat mediator ability for magnetic hyperthermia, as compared to pure iron oxide clusters. Due to the rich chemistry of spinel ferrites, we anticipate that the obtained results could be extended to the fabrication of other doped ferrites, such as $CoFe_2O_4$, $NiFe_2O_4$, $ZnFe_2O_4$, enabling therefore to fine-tune the magnetic behaviour of the resulting cluster. As an alternative approach to obtain magnetic clusters with tuneable properties, clusters made out of two different kind of primary particles, such as magnetic iron oxide and a noble metal such as Au, Ag or Pt, was proposed for the first time. The proposed synthesis provides new materials as tools for biomedical use in MRI and hyperthermia treatment, and open the way to the design of novel heterostructures based on clusters made out of primary particles with different functionalities. It is expected that such clusters may find application in many fields beyond biomedical use investigated in this work, as they may effectively address practical issues that cannot be achieved through individual nanoparticles.

Overall, the research on advanced versatile protocols presented in this work contributes to fabricate functional materials and to elucidate the structure-properties relationship at the nanoscale through structural, morphological and physico-chemical characterization, providing the basis for the rational design of novel functional nanostructures for energy and life science applications.

Appendix

Instrumentation

A multi-technique approach was used in order to investigate the structural and morphological features, as well as the physical properties of semiconducting and magnetic nanoparticles and heterostructures synthesized in this work.

Conventional techniques of characterization were performed either at the Department of Chemical or at the Department of Physics of the University of Cagliari (TEM, XRD, ICP-MS, DLS, UV-Vis, ultrafast optical spectroscopy). HR-TEM, magnetic investigation, relaxometry and SAR measurements were acquired at the "Istituto Italiano di Tecnologia" (Genova, IT) during a research visit under the supervision of Dr. Andrea Falqui and Dr. Teresa Pellegrino.

In order to obtain quantitative structural information on the local structure of individual atoms in the semiconducting CdSe@CdS nanocrystals, advanced characterization, i.e. extended X-ray absorption fine structure (EXAFS) measurements were collected on the B18 beamline of the DIAMOND synchrotron light source (Oxfordshire, UK) under the supervision of Prof. Anna Corrias.

In the following, the basic principles underlying the characterization techniques and the experimental conditions used to investigate the nanostructures synthesised in our laboratories, are summarized.

TRANSMISSION ELECTRON MICROSCOPY

Images of semiconductor and magnetic nanoparticles were collected by Transmission Electron Microscopy (TEM) using an Hitachi H-7000 microscope equipped with a W thermoionic electron source operating at 125 kV and an AMT DVC (2048x2048 pixel) CCD Camera. Samples for TEM analysis were prepared by depositing a drop of diluted nanocrystals solution onto 200 mesh carbon-coated copper grid and then allowing the solvent to evaporate at room temperature. Also, in order to promote the removal of organic capping the grids were heated to 140 °C for 30 min before imaging.

The average sizes and size distribution of the various NCs samples were determined by analysing the images recorded with ImageJ software.[80]

The mean diameter and size distribution of each sample were obtained from a statistical analysis over about 100÷300 nanoparticles.

Basic principles of TEM

Transmission electron microscopy (TEM) is a microscopy technique which makes use of an electronic beam, which directly illuminates a sample in transmission mode and generates an image. The direct imaging capability of the TEM with resolution at the nanometric scale is particularly useful for nanomaterials with no-spherical shapes allowing a direct measure of aspect ratio. On the other hand, the intrinsic limitation of TEM is that two dimensional projections of three dimensional objects are obtained. [81]

The ability of TEM to investigate objects with size in the order of nanometre relies to the small De Broglie wavelength of electrons. More specifically, the electron beam is transmitted through an ultra-thin specimen (maximum thickness 200 nm), interacting with the specimen as it passes through. Depending on the density of the specimen, some of the electrons are scattered. At the bottom of the microscope the unscattered electrons hit a fluorescent screen, which gives rise to a 2D image of the specimen with its different parts displayed in varied darkness according to their density. The image can be recorded on a layer of photographic film, or by a digital camera.
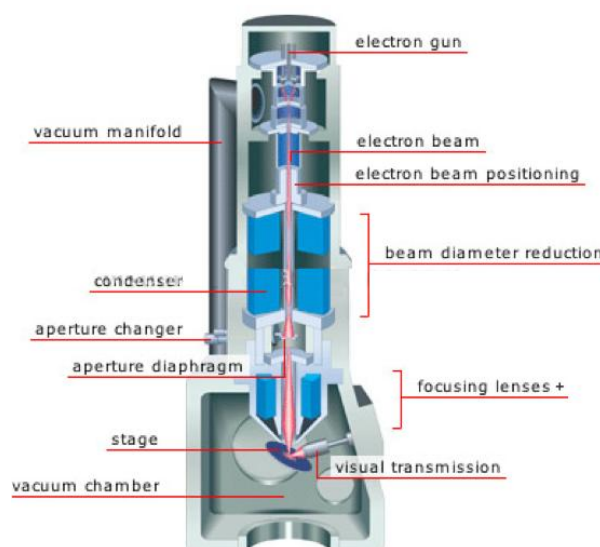

Fig. I Schematic representation of the main components and configuration of a Transmission Electron Microscope.

The basic steps involved in TEMs (Fig.I) are listed below:
- a stream of electrons is formed and accelerated toward the specimen using a positive electrical potential;
- this stream is confined and focused using metal apertures and magnetic lenses into a thin, focused, monochromatic beam;
- this beam is focused onto the sample using a magnetic lens;
- interactions occur inside the irradiated sample, affecting the electron beam: these interactions and effects are detected and transformed into an image.

Using different observation modes, two kind of interaction can be analyzed:
- the *bright field mode* detects unscattered electrons which are transmitted through the thin specimen without any interaction occurring inside the specimen. The transmission of

unscattered electrons is inversely proportional to the specimen thickness. Moreover, denser areas of the sample or area containing heavier atoms will appear darker.

- electrons that are scattered by atoms in the specimen in an elastic fashion can be detected using *dark field* mode. These scattered electrons are transmitted through the remaining portions of the specimen.

All electrons are scattered according to Bragg's law described below:

$$2d_{hkl} \sin \theta = n\lambda$$

where d_{hkl} is the distance between the reticular planes; *h,k,l*, are Miller's indexes of the considered planes and θ is the incident angle.

All incident electrons of the monochromatic beam that are scattered by the same atomic spacing will be scattered by the same angle. These scattered electrons can be collected using magnetic lenses to form a pattern of spots; each spot corresponding to a specific atomic spacing (a plane). This pattern can then yield information about the orientation, atomic arrangements and phases present in the area being examined. If the sample is polycrystalline the image appears with concentric ring, whereas if the material is amorphous haloes are observed.

X-RAY POWDER DIFFRACTION

Powder X-Ray Diffraction (XRD) measurements of semiconductor and magnetic nanoparticles were carried out using a Panalytical Empyrean diffractometer equipped with a X'Celerator linear detector, using Cu Kα radiation operating at 40 kV/40 mA and a monochromator on the diffracted beam. The scans were collected under sample spinning operating in θ–2θ Bragg-Brentano geometry within the range of 10°-90° (2θ) using a step size of 0.05 sec per step. Samples for XRD measurements were prepared by depositing some drops of concentrated colloidal dispersion in solution on a low background Si sample holder and then allowing the solvent to evaporate at room temperature.

Phase identification was performed according to the Powder Diffraction File Database [82] and the determination of the mean crystallite diameter was estimated on the more intense peak using the Scherrer's equation. The instrumental broadening was estimated through a LaB_6 reference sample.

Basic principles of XRD

X-ray powder diffraction is the most relevant technique to obtain structural information about crystalline samples, in terms of the crystallographic structure, crystallite size (grain size) and preferred orientation in polycrystalline or powdered solid samples. It is based on the elastic scattering of X-rays from structures that have long range order.

The most simple and known description of the phenomenon is given by the Bragg's Law, previously mentioned.
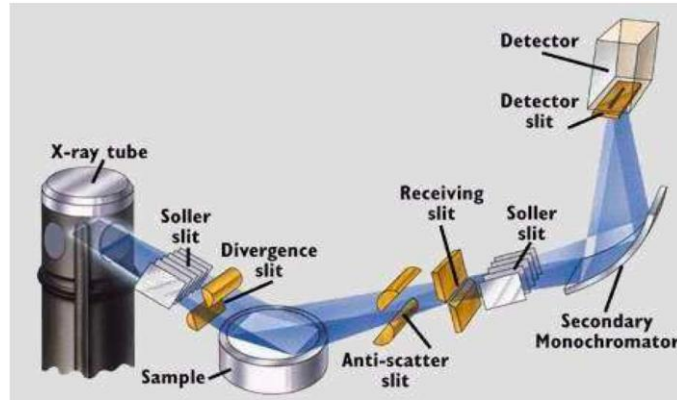
Fig. II Schematic representation of the main components and configuration of a X-ray diffract meter

According to this interpretation, X-rays are scattered by semi-reflective atomic planes and constructive interference is observed when path-length of rays reflected by successive planes differ for a integer multiple of the wavelength.

As depicted in Fig. II, the main component are the following:

- A radiation source: generally electrons are boiled off of a cathode (usually a tungsten filament) and accelerated through a strong electric potential of ~ 50 kV; having reached a high speed, the electrons collide with a metal plate (anode), emitting bremsstrahlung radiation and some strong spectral lines corresponding to the excitation of inner-shell. The most common metal used is copper, which can be kept cool easily, due to its high thermal conductivity and which produces strong K_α and lines. The K_β line is sometimes suppressed with a thin (~ 10 μm) nickel foil.

- a sample stage.

- a detector of the intensity of scattered rays.

Moreover, the geometry of the diffractometer is very important and can be of two kind: the θ-θ or the θ-2θ. In the θ-θ the radiation source and the detector system move forming a θ angle respect to the sample that is fixed and horizontally placed. In the θ-2θ (most used) the radiation source is fixed while the sample and the detector moves (the detector moves with an angle θ and consequentially the detector with an angle 2θ. The intensity of the diffracted peak is determined by the electronic density in the reticular plane. Information about the nanocrystals can be obtained from the diffraction pattern through:

- the position of the peaks, which is determined by the size and the shape of the elementary cell of the material

- the width of the peak, measured as the width at the medium height, which is inversely proportional to the size of coherent domains of diffraction and increases in the presence of lattice deformations and defects of reticules. In the absence of deformations and defects the size of crystallite can be determined by the Scherrer's law:

$$< d >= \frac{K \cdot \lambda}{B \cdot \cos\theta}$$

where $<d>$ is the mean crystallite size (Å), λ is the wavelength of the incident X-Ray (1.54178 Å), K is a constant equal to 0.9, B is the width at the medium height (FWHM) of the peak (in radians) and θ is the angle at which the peak lies.

Note that B is the experimental peak width corrected for instrumental broadening.

DYNAMIC LIGHT SCATTERING (DLS)

Dynamic light measurements on magnetic nanoclusters dispersed in water were performed on a Zetasizer Nano ZSP (Malvern Instrument) equipped with a 4 mW He-Ne laser operating at 633 nm. The measurements were conducted with a disposable cuvettes (DTS0012) for each sample setting 1.33 as the dispersant refractive index at 25°C. The data analysis was performed with 173° backscatter (NIBS default) as angle of detection, the measurement duration was set automatic and the measurements have been repeated three times.

In order to obtain accurate measurement samples optically clear are required. For this reason, if necessary, 3 µL of sample were diluted in 1 ml of milliQ water.

Basic principles of DLS

This technique was used to gain information about the hydrodynamic size and stability and aggregation state of the colloidal nanoparticles.

The particle size measured in a (DLS) instrument is the diameter of the sphere that diffuses at the same speed as the particle being measured; for this reason, with this technique it is possible to estimate the size of the overall nanoparticles considering also the thickness of the organic shell and it is possible recognize the presence of aggregates in colloidal dispersion.

Fluctuations in the scattered light intensity, due to the Brownian motion of the particles (defined as "the random movement of particles in a liquid due to the bombardment by the molecules that surround them"), are used to determine the particle diffusion coefficient which is then related to its hydrodynamic radius via the Stokes Einstein relationship. [83]

The particles in a liquid move about randomly and their speed of movement is used to determine the size of the particle. It is known that small particles move or diffuse more quickly in a liquid than larger particles. This movement is carrying on all the time. So if we take two 'pictures' of the sample separated by a short interval of time we can see how much the particles have moved and therefore calculate their size.

If there has been a minimal particle movement between the two 'pictures' the particles in the sample can be inferred as large; similarly if there has been a large amount of movement between the two 'pictures', then the particles in the sample can be inferred as small.

Using this knowledge and the relationship between diffusion speed and size, the size can be determined.

DLS has a broad working concentration and size range of $\sim 10^8 \div 10^{12}$ particles/mL and 10-1000 nm, respectively; however, its sixth power dependence on scattering versus particle size means that wide nanoparticle size distributions can obscure the presence of smaller materials in the sample.

A typical DLS system includes six main components. A laser provide a light source to illuminate the sample contained in a cell. A detector is used to measure the scattered light. An attenuator is placed between the laser and the cell in order to maintain the scattering light within the specific range and to obtain a successful measurement. The scattering intensity signal is passed to a digital signal processing board called a correlator, which compares the scattering intensity at successive time intervals to derive the rate at which the intensity is varying and passes this information to a computer, for data analysis.

X-RAY ABSORPTION SPECTROSCOPY

EXAFS measurements were collected on semiconductor CdSe@CdS rod and octapod, on CdS, CdSe and CuCl reference compounds on the B18 beamline of the DIAMOND

synchrotron (Oxfordshire, UK), which covers a wide energy range (2.05 to 35 keV) and is equipped with a double-crystal monochromator containing two pairs of crystals, Si(111) and Si(311), optimized for QEXAFS measurements. [63]

Spectra were acquired at the S (2472 eV), Cu K-edge (8979 eV), Cd (26711 eV), and Se (12658 eV) K-edges

At the S K-edge, data collection is performed under vacuum because of the low energy of the X-rays, using two different detectors: a fluorescence detector (for the CdS standard compound), and a Total Electron Yield (TEY) detector (for all the samples). Samples were deposited from the toluene dispersion either on aluminum foil or on carbon sticky tape and let dry. At the Cu K-edge data were collected on the CuCl standard compound in transmission mode and on the Octa sample both in transmission and fluorescence mode.

At the Cd K-edge data on samples and standard compounds were all collected in transmission mode. The CdS and CdSe samples were measured as pellets made out mixing the standard compounds with polyvinylpyrrolidone, so to have a suitable and highly uniform optical thickness, while the suspensions of the CdSe@CdS in toluene were measured using cells for liquids with kapton windows.

At the Se K-edge data were collected in transmission mode on the CdSe pellet and in fluorescence mode on the cells for liquids containing the suspensions of the CdSe@CdS in toluene.

The EXAFS data processing was carried out using the ATHENA software and the fit to scattering models in R-space was obtained by FEFF in Artemis.[63]

Basic principles of EXAFS

X-ray Absorption Spectroscopy explores variations in the absorption coefficient of a material with photon energy. [84] The interaction of X-rays with matter consists in different processes (i.e. scattering, absorption): for high energy X-rays (over 1000 eV), the dominant process is the photoelectric effect, which consist in the ejection of a core electron after photon absorption.

The intensity of X-rays passing through a material is attenuated according to the Lambert-Beer law

$$I = I_0 e^{-\mu t}$$

where I is the intensity of the transmitted beam, t the material thickness and I_0 the incident beam intensity. The absorption coefficient μ depends both on material properties and photon energy (E) and decreases gradually as photon energy increases, until a critical wavelength is reached where the absorption coefficient value increases abruptly. This discontinuity in the absorption coefficient corresponds to the ejection of a core electron from an atom and it is called absorption edge. The energy corresponding to the edge (E_0) is element specific, since it corresponds to the binding energy of the photoelectron. A further decrease in λ causes a decrease in μ, but at a somewhat different rate, until another adsorption edge is reached. For isolated atoms, the absorption coefficient decreases monotonically as a function of energy beyond the edge. When the absorption process occurs in a molecule or in condensed matter, the ejected photoelectron interacts with atoms in the immediate neighbourhood, resulting in a modulation of the absorption coefficient beyond the edge. It is possible to roughly divide the absorption spectrum in two regions (Fig. III), based on the energy gap between the absorption edge and the incoming photon ($E-E_0$) corresponding to the kinetic energy of the ejected photoelectron, according to different interaction regimes with the surrounding atoms:

1) XANES (*X-ray Absorption Near Edge Structure*): the low side of the absorption spectrum, from 0 to 60÷100 eV above E_0. In this region the electron ejected by the absorber atom in the photoionization process has a low kinetic energy; as a consequence, it is strongly scattered by neighbouring atoms to multiple scattering process. This region yields information about symmetries and chemical state.

2) EXAFS (*Extended X-ray Absorption Fine Structure*): form 60÷100 to 1000 eV above the edge. The ejected electrons are weakly scattered, so that only single scattering processes are generally relevant. The term EXAFS refers to the oscillations in this spectral region originated by destructive and constructive interference effects that occur between the electron wave outgoing from the adsorbing atom and the backscattered waves of its neighbours. This region provides several kinds of structural information, like coordination numbers, inter-atomic distances, crystalline disorder and Debye-Waller factors for the pair correlation functions involving the absorber and the backscattered atom.
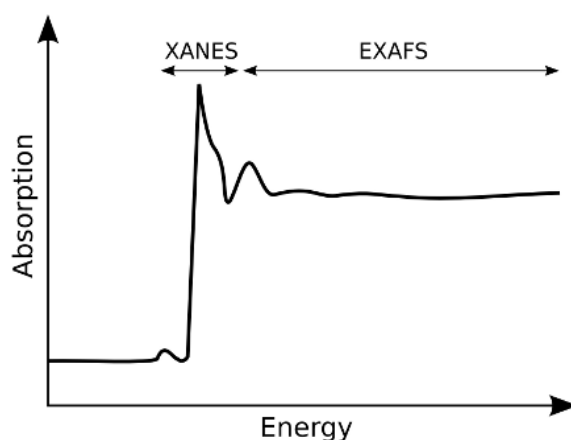

Fig. III Schematic illustration of an X-ray absorption spectrum, showing the structured absorption attributable both to the XANES and to the EXAFS.

The discussion and interpretation of the XANES spectral region requires heavy and complicated multiple scattering calculations. On the other hand, EXAFS oscillations are due to single electron scattering process and can be handled with a simpler mathematic treatment.

The important advantage of XAFS is its selectivity toward each atomic species and its sensitivity to short-range order only. In fact, XAFS probes the local structure around the absorbing atom, the mean free path of the photoelectron being limited to about 10 Å. For these reasons, the typical applications of XAFS spectroscopy include studies on polyatomic materials (since different atomic species can be selected), amorphous materials (which are studied by comparison to the corresponding crystalline sample) and materials containing clusters embedded in a matrix constituted by different atomic species.

Whit particular reference on EXAFS, it is well known that the probability for a core electron to absorb an X-ray photon depends on the initial and final energy states. Above the edge, the final state can be described by an outgoing spherical wave, originated in correspondence of the absorbing atom. This wave can be scattered by neighbouring atoms, resulting in an interference pattern. The final state depends on the phases of both waves (outgoing and scattered), which in turn will depend on the electron wavevector (k) or equivalently on the ejection energy. Hence the exact position of neighbouring atoms can affect the probability of exciting a core electron and gives rise to the oscillatory behaviour of the absorption coefficient as a function of photoelectron energy.

Mathematically, the interference term arising from scattering by a single neighbour atom can be expressed as *A(k)sin(2kr+φ(k))* where *k* is the modulus of the wavevector, *r* is the distance between absorbing and neighbour atom and *φ(k)* represents the total photoelectron phase-shift and depends on both photoabsorber and scattering atoms. *A(k)* is the backscattering amplitude and is mainly a characteristic of the scattering atom. The total EXAFS signal consists in the superposition of individual pair-wise contributions from all the neighbouring atoms. These can be grouped into coordination shells composed of atoms found at similar distance from the absorbing atom.

The EXAFS oscillations *χ(k)* are given by:

$$\chi(k) = \sum_j S_0^2(k) \frac{N_j}{kr_j^2} e^{-\sigma_j^2 k^e} e^{-2\frac{r_j}{\lambda_j(k)}} A_j(k) \sin\left[akr_j + \varphi_j(k)\right]..$$

where $k = \sqrt{\frac{2m}{\hbar^2}(E - E_0)}$ is the photoelectron wavevector modulus; *j* is the coordination shell index; *r* is the distance between the adsorbing atom and a neighbour; *N* is the number of identical atoms in the same coordination shell; *A(k)* is the backscattering amplitude; σ is the total Debye-Waller factor (including static and dynamic contributions); *φ(k)* is the total phase shift; *λ(k)* is the photoelectron mean free path; $S_0^2(k)$ is the amplitude reduction due to many-body effect; *E* is the photon energy; *m* is the electron mass; *E₀* is the threshold energy.

The structural parameters involved in the EXAFS equations are the coordination number (*N*), the interatomic distance (*r*) and the Debye- Waller factor (σ). The latter includes two contributions: one a dynamic one, arising from atomic vibration, and a static one, which is caused by structural disorder in a given coordination shell. Those structural parameters are generally obtained by fitting the experimental EXAFS curve profile with the theoretical equation of *χ(k)* described above.

UV-VISIBLE SPECTROPHOTOMETRY

UV-Visible absorption spectra were recorded in the range 300÷800 nm on a UV-Vis Varian Cary 50 Spectrophotometer equipped with a Xenon flash lamp and a Si-based detector. Spectra of all semiconductor sample dispersed in toluene were recorded in a quartz cuvette with a 1 cm path length, whereas for magnetic cluster samples dispersed in water was used a plastic disposable cuvette.

Basic principles of UV-visible

Lambert's Law states that each layer of equal thickness of an absorbing medium absorbs an equal fraction of the radiant energy that traverses it.

The fraction of radiant energy transmitted by a given thickness of the absorbing medium is independent of the intensity of the incident radiation, provided that the radiation does not alter the physical or chemical state of the medium.

The Beer-Lambert Law states that the concentration *C* of a substance in solution is directly proportional to the absorbance *A* of the solution.

$$A = \varepsilon\, C\, d$$

When monochromatic radiation passes through a homogeneous solution in a cell of thickness *d*, the intensity of the emitted radiation depends upon the concentration C of the

solution. Absorbance in older literature is sometimes referred to as *extinction* or *optical density.*

The UV-Vis spectrophotometer [85] measures the intensity of light passing through a sample (I), and compares it to the intensity of light before it passes through the sample (I_o). The ratio I/I o is called the transmittance, and is usually expressed as a percentage (%T).

The main components of a spectrophotometer (Fig. IV) are a light source, a holder for the sample, a diffraction grating in a monochromator or a prism to separate the different wavelengths of light, and a detector.
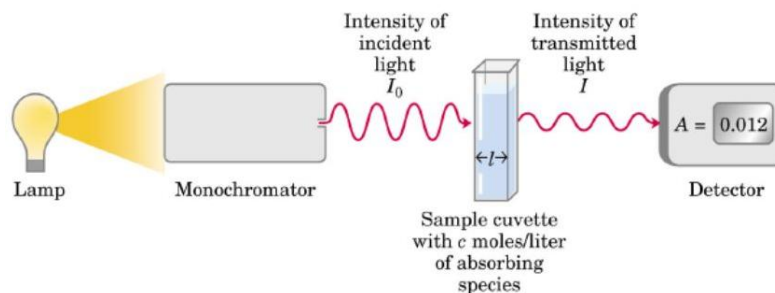
Fig. IV Schematic representation of the main components and configuration of a UV-vis spectrophotometer

The radiation source is often a Tungsten filament (300-2500 nm), a deuterium arc lamp, which is continuous over the ultraviolet region (190-400 nm), Xenon arc lamp, which is continuous from 160-2.000 nm; or more recently, light emitting diodes (LED) for the visible wavelengths. The detector is typically a photomultiplier tube, a photodiode, a photodiode array or a charge-coupled device (CCD). Single photodiode detectors and photomultiplier tubes are used with scanning monochromators, which filter the light so that only light of a single wavelength reaches the detector at one time. The scanning monochromator moves the diffraction grating to "step-through" each wavelength so that its intensity may be measured as a function of wavelength. Fixed monochromators are used with CCDs and photodiode arrays. As both of these devices consist of many detectors grouped into one or two dimensional arrays, they are able to collect light of different wavelengths on different pixels or groups of pixels simultaneously.

A spectrophotometer can be either single beam or double beam. In a single beam instrument, all of the light passes through the sample cell. I_o must be measured by removing the sample. This was the earliest design and is still in common use in both teaching and industrial labs. In a double-beam instrument, the light is split into two beams before it reaches the sample. One beam is used as the reference; the other beam passes through the sample. The reference beam intensity is taken as 100% Transmission (or 0 Absorbance), and the measurement displayed is the ratio of the two beam intensities.

Samples for UV-Vis spectrophotometry are most often liquids, although the absorbance of gases and even of solids can also be measured. Samples are typically placed in a transparent cell, known as a cuvette. Cuvettes are typically rectangular in shape, commonly with an internal width of 1 cm. (This width becomes the path length, L, in the Beer-Lambert law). The most widely applicable cuvettes are made of high quality fused silica or quartz glass because these are transparent throughout the UV, visible and near infrared regions. Glass and plastic cuvettes are also common, although glass and most plastics absorb in the UV, which limits their usefulness to visible wavelengths.

A complete spectrum of the absorption at all wavelengths of interest can often be produced directly by a more sophisticated spectrophotometer. In simpler instruments the absorption is

determined one wavelength at a time and then compiled into a spectrum by the operator. By removing the concentration dependence, the extinction coefficient *(ε)* can be determined as a function of wavelength.

References

[1] C. P. Poole, F. J. Owens *Introduction to Nanotechnology* 2003 Wiley

[2] R. G. Chaudhuri, S. Paria *Core/Shell Nanoparticles: Classes, Properties, Synthesis Mechanisms, Characterization and Applications* 2012 Chem. Rev. 112 2373–2433

[3] A. P. Alivisatos *Perspectives on the Physical Chemistry of Semiconductor Nanocrystals* 1996 The Journal of Physical Chemistry 100 13226-13239

[4] C. Cohen-Tannoudji, B. Diu, F. Laloë *Quantum Mechanics* 1977 Wiley

[5] V. I. Klimov *Semiconductor and Metal Nanocrystals: Synthesis and Electronic and Optical Properties* 2004 Marcel Dekker

[6] U. Banin, O. Millo *Tunneling and Optical Spectroscopy of Semiconductor Nanocrystals* 2003 Annual Review of Physical Chemistry 54 465-492

[7] S. Kumar, T. Nann *Shape Control of II-VI Semiconductor Nanomaterials* 2006 Small 2 316-319

[8] J. B. Li, L. W. Wang *Shape Effects on Electronic States of Nanocrystals* NanoLetters 2003 3 1357-1363

[9] Y. Cui, U. Banin, M.T Bjork, A.P. Alivisatos *Electrical Transport through a Single Nanoscale Semiconductor Branch Point* 2005 NanoLetters 5 1519-1523

[10] A.L. Rogach *Semiconductor Nanocrystal Quantum Dots: Synthesis, Assembly, Spectroscopy and applications* New York 2008

[11] P. Reiss, M. Protière, L. Li *Core/Shell Semiconductor Nanocrystals* 2009 Small 5 2 154–168

[12] M.A. Hines, P. Guyot-Sionnest *Synthesis and Characterization of Strongly Luminescing ZnS-Capped CdSe Nanocrystals* 1996 Journal of Physical Chemistry 100 468-471

[13] Z.A. Peng, X. Peng *Nearly Monodisperse and Shape-Controlled CdSe Nanocrystals via Alternative Routes: Nucleation and Growth* 2002 JACS 124 3343-3353

[14] B.K. Hughes, J.M. Luther, M.C. Beard *The Subtle Chemistry of Colloidal, Quantum-Confined Semiconductor Nanostructures* 2012 ACS Nano 6 6 4573–4579

[15] Y.Yin, A.P. Alivisatos *Colloidal nanocrystal synthesis and the organic-inorganic interface* 2005 Nature 437 664-670

[16] L. Manna, D.J. Milliron, A. Meisel, E.C. Scher, A.P. Alivisatos *Controlled growth of tetrapod-branched inorganic nanocrystals* 2003 Nature Materials 2 6 382-385

[17] Carbone L., Nobile C., De Giorgi M., Della Sala F., Morello G., Pompa P., Hytch M., Snoeck E., Fiore A., Franchini I.R., Nadasan M., Silvestre A.F., Chiodo L., Kudera S., Cingolani R., Krahne R., Manna L. *Synthesis and Micrometer-Scale Assembly of Colloidal CdSe/CdS nanorods prepared by a seeded growth approach* 2007 NanoLetters 7 2942-2950

[18] Deka S., Miszta K., Dorfs D., Genovese A., Bertoni G., Manna L. *Octapod-Shaped Colloidal Nanocrystals of Cadmium Chalcogenides via "One-Pot" Cation Exchange and Seeded Growth* 2010 Nano Letters 10 3770-3776

[19] Miszta K., Dorfs D., Genovese A., Kim M.R., Manna L. *Cation Exchange Reactions in Colloidal Branched Nanocrystals* 2011 ACS Nano 5 7176-7183

[20] H. Haug, S.W. Koch *Quantum Theory of the Optical and Electronic Properties of Semiconductors* 1998 III Ed. New York [21]

[21] S. Kinge, M. Crego-Calama, D.N. Reinhoudt *Self-assembling nanoparticles at surfaces and interfaces* 2008 Chem. Phys. Chem. 9 20-42

[22] C.de Mello Donegà, M. Bode, A. Meijerink *Size- and temperature-dependence of exciton lifetimes in CdSe quantum dots* 2006 Physical Review B 74 085320

[23] Gur, I., Fromer N.A., Chen C.P., Kanaras, A.G., Alivisatos A.P. *Hybrid solar cells with prescribed nanoscale morphologies based on hyperbranched semiconductor nanocrystals* 2007 NanoLetters 7 2 409-414; I. Gur, N.A. Fromer, M.L. Geier, A.P. Alivisatos *Air-Stable All-Inorganic Nanocrystal Solar Cells Processed from Solution* 2005 Science 2005 310 462

[24] D. Carboni, D. Marongiu, P. Rassu, A. Pinna, H. Amenitsch, M. Casula, A. Marcelli, G. Cibin, P. Falcaro, L. Malfatti, P. Innocenzi *Enhanced Photocatalytic Activity in Low-Temperature Processed Titania Mesoporous Films* 2014 J. Phys. Chem. C 118 12000−12009

[25] Khan Sum, Al-Shahry M., Ingler W.B. *Efficient photochemical water splitting by a chemically modified n-TiO_2* 2002 Science 297 5590 2243-2245

[26] Y. Pu , G. Wang, K. Chang, Y. Ling , Y. Lin, B.C. Fitzmorris ,C. Liu , X. Lu, Y. Tong, J. Z. Zhang , Y. Hsu, Y. Li *Au nanostructure-decorated TiO_2 nanowires exhibiting photoactivity across entire UV-visible region for photoelectrochemical water splitting* 2013 NanoLett 13 3817-3823

[27] V. Kamat *Manipulation of Charge Transfer Across Semiconductor Interface. A Criterion That Cannot Be Ignored in Photocatalyst* 2012 Design J. Phys. Chem. Lett. 3 663−672

[28] Pankhurst Q.A., Connolly J., Jones S.K., Dobson J. *Applications of magnetic nanoparticles in biomedicine* 2003 J. Phys. D Appl. Phys. 36 167-181

[29] Allan H Morrish *The Physical Principles of Magnetism* 1965 Wiley New York 1965

[30] Leslie-Pelecky D.L., Rieke R.D. *Magnetic Properties of Nanostructured Materials* 1996 Chem. Mater. 8 1770-1783

[31] Kittel, C. *Theory of the structure of ferromagnetic domains in films and small particles.* 1946 Phys. Rev. 70 965–971

[32] Gubin S.P., Koksharov Y.A., Khomutov G.B., Yurkov G.Y. *Magnetic nanoparticles: Preparation, structure and properties.* 2005 Russ. Chem. Rev. 74 489–520

[33] Colombo M., Carregal-Romero S., Casula M.F., Gutiérrez L., Morales M.P., Bohm I.B., Heverhagen J.T., Prosperi D., Parak W.J. *Biological applications of magnetic nanoparticles* Chem. Soc. Rev. 2012 41 4306–4334

[34] A.R. West *Basic Solid State Chemist*ry Second Edition Wiley 1999

[35] Bellouard C., Mirebeau I., Hennion M. *Magnetic correlations of fine ferromagnetic particles studied by small-angle neutron scattering.* 1996 Phys. Rev. B 53 5570–5578

[36] B. Issa, I.M. Obaidat, B.A. Albiss, Y. Haik *Magnetic Nanoparticles: Surface Effects and Properties Related to Biomedicine Applications* 2013 Int. J. Mol. Sci. 14 21266-21305

[37] J. Smit, H.P.J. Wijn *Ferrites* Philips Technical Library 1959

[38] H.St.C. O'Neill, A. Navrotsky *Simple Spinels: Crystallographic Parameters, Cation Radii, Lattice Energies, and Cation Distributions* 1983 Amer. Miner. 68 181

[39] S. Sun, H. Zeng, D.B. Robinson, S. Raoux, P.M. Rice, S.X. Wang, G. Li *Monodisperse MFe_2O_4 (M = Fe, Co, Mn) Nanoparticles* 2004 J. AM. CHEM. SOC. 126 273-279

[40] Bulte J.W.M., Kraitchman D.L. *Iron oxide MR contrast agents for molecular and cellular imaging* 2004 NMR Biomed. 17 484–499.

[41] Ito A., Honda H., Kobayashi T. *Cancer immunotherapy based on intracellular hyperthermia using magnetite nanoparticles: A novel concept of -heat-controlled necrosis with heat shock protein expression* 2006 Cancer Immunol. Immunother. 55 320–328

[42] Nitin N., LaConte L.E.W., Zurkiya O., Hu X., Bao G. *Functionalization and peptide-based delivery of magnetic nanoparticles for intracellular MRI contrast.* 2004 J. Biol. Inorg Chem. 9 706–712

[43] Mann S., Frankel R.B., Blakemore R. *Structure, morphology and crystal growth of bacterial magnetite* 1984 Nature 310 405–407

[44] https://www.cis.rit.edu/htbooks/mri/

[45] Laurent S., Forge D., Port M., Roch A., Robic C., Vander Elst L., Muller R.N. *Magnetic iron oxide nanoparticles: synthesis, stabilization, vectorization, physicochemical characterizations, and biological applications* 2008 Chem Rev. 108 6 2064-110.

[46] E. Taboada, E. Rodríguez, A. Roig, J. Oró, A. Roch, R.N. Muller *Relaxometric and Magnetic Characterization of Ultrasmall Iron Oxide Nanoparticles with High Magnetization. Evaluation as Potential T_1 Magnetic Resonance Imaging Contrast Agents for Molecular Imaging* 2007 Langmuir 23 8 4583–4588

[47] Corti M., Lascialfari A., Micotti E., Castellano A., Donativi M., Quarta A., Cozzoli P.D., Manna L., Pellegrino T., Sangregorio C. *Magnetic properties of novel superparamagnetic MRI contrast agents based on colloidal nanocrystals.* 2008 J. Magn. Magn. Mater. 320 e320–e323

[48] Arcangeli G, Guerra A, Lovisolo G, Cividalli A, Marino C, Mauro F. *Tumor response to heat and radiation: Prognostic variables in the treatment of neck node metastases from head and neck cancer.* Int. J. Hyperthermia 1985 1 201-217 1985.

[49] Q.A. Pankhurst, N.K.T. Thanh, S.K. Jones, J.Dobson *Progress in applications of magnetic nanoparticles in biomedicine* 2009 J. Phys. D: Appl. Phys. 42 224001

[50] Fortin JP, Wilhelm C., Servais J., Ménager C., Bacri JC., Gazeau F. *Size-sorted anionic iron oxide nanomagnets as colloidal mediators for magnetic hyperthermia* 2007 J Am Chem Soc. 7 129 9 2628-35

[51] Lartigue L., Innocenti C., Kalaivani T., Awwad A., Sanchez M, Guari Y., Larionova J., Guérin C., Montero JL., Barragan-Montero V., Arosio P., Lascialfari A., Gatteschi D., Sangregorio C. *Water-dispersible sugar-coated iron oxide nanoparticles. An evaluation of their relaxometric and magnetic hyperthermia properties* 2011 JACS. 133 10459

[52] M. Zeisberger, S. Dutz *Metallic Co nanoparticles for heating applications* 2007 J. Magn. Magn. Mater. 311 224-227; B. Mehdaoui, A. Meffre, L. Lacroix, J. Carrey, S. Lachaize, M. Gougeon, M. Respaud *Large specific absorption rated in the magnetic hyperthermia properties of metallic iron nanocubes* 2010 *J. Magn. Magn. Mater. 322* L49; F. Mohammad, G. Balaji, A. Weber, R.M. Uppu, C.S. S.R. Kumar *Influence of Gold Nanoshell on Hyperthermia of Super Paramagnetic Iron Oxide Nanoparticles (SPIONs)* 2010 J. Phys. Chem. C 114 45 19194–19201

[53] Milliron D.J., Hughes S.M., Cui Y., Manna L., Li J., Wang L.W., Alivisatos A.P. *Colloidal nanocrystal heterostructures with linear and branched topology* 2004 Nature 430

[54] Mokari T. *Synthesis and characterization of hybrid nanostructures* 2011 NanoReviews2

[55] Habas S.E., Yang P., Mokari T. *Selective growth of metal and binary metal tips on CdS nanorods* 2008 Journal of The American Chemical Society 130 3294-3295

[56] Amirav, L., Alivisatos, A.P. *Photocatalytic Hydrogen Production with Tunable Nanorod Heterostructures* 2010 J. Phys. Chem. Lett 1 1051–1054

[57] S. Kudera, L. Carbone, L. Manna, W. J. Parak *Growth Mechanism, shape and composition control of semiconductor nanocrystals, in Semiconductor Nanocrystal Quantum Dots* A. L. Rogach, Ed. Springer, Wien 2008

[58] Talapin D.V., Nelson J.H., Shevchenko E.V., Aloni S., Sadtler B., Alivisatos A.P. *Seeded growth of highly luminescent CdSe/CdS nanoheterostructures with rod and tetrapod morphologies* 2007 NanoLetters 7 10 2951-2959; R. Brescia, K. Miszta, D. Dorfs, L. Manna,

G. Bertoni *Birth and Growth of Octapod-Shaped Colloidal Nanocrystals Studied by Electron Tomography* 2011 J. Phys. Chem. C 115 20128–20133

[59] Miszta K., de Graaf J., Bertoni G., Dorfs D. Brescia R., Marras S., Ceseracciu L., Cingolani R., Van Roij R., Dijkstra M., Manna L. *Hierarchical self-assembly of suspended branched colloidal nanocrystals into superlattice structure*s 2011 Nature Materials 10 872-876

[60] Streetman B., Banerjee S. *Solid State Electronic Devices* 2000 New Jersey

[61] A. Corrias, **E. Conca**, G. Cibin, G. Mountjoy, D. Giannolio, F. De Donato, L. Manna, M.F. Casula *Insights on the structure of dot-rod and dot-octapod CdSe@CdS semiconducting nanocrystals,* submitted

[62] A.J. Dent, G. Cibin, S. Ramos, A.D. Smith, S.M. Scott, L. Varandas, M.R. Pearson, N.A. Krumpa, C.P. Jones, P.E. Robbins J. Phys. Conf. Ser. 190 2009 012039.

[63] B. Ravel and M. Newville, *ATHENA, ARTEMIS, HEPHAESTUS: data analysis for X-ray absorption spectroscopy using IFEFFIT* 2005 Journal of Synchrotron Radiation 12 537

[64] Mokari T., Rothenberg E., Popov I., Costi R., Banin U. *Selective Growth of Metal Tips onto Semiconductor Quantum Rods and Tetrapods* 2004 Science 304 1787–1790

[65] **E. Conca**, M. Aresti, M. Saba, M. F. Casula, F. Quochi, G. Mula, D. Loche, M. R. Kim, L. Manna, A. Corrias, A. Mura and G. Bongiovanni *Charge separation in Pt-decorated CdSe@CdS octapod nanocrystals* 2014 Nanoscale 6 2238–2243

[66] F. Scotognella, K. Miszta, D. Dorfs, M. Zavelani-Rossi, R. Brescia, S. Marras, L. Manna, G. Lanzani and F. Tassone *Ultrafast Exciton Dynamics in Colloidal CdSe/CdS Octapod Shaped Nanocrystals* 2011 J. Phys. Chem. C 115 9005–9011; M.R. Antognazza, F. Scotognella, K. Miszta, D. Dorfs, M. Zanella, M. Zavelani-Rossi, L. Manna, G. Lanzani and F. Tassone *Steady-state photoinduced absorption of CdSe/CdS octapod shaped nanocrystals* 2011 Phys. Chem. Chem. Phys. 2011 13 15326–15330

[67] Reiss G., Hütten A. *Magnetic nanoparticles: Applications beyond data storage* Nature Materials 2005 4 725-726

[68] Ge J., Hu Y., Biasini M., Beyermann W.P., Yadong Y. *Superparamagnetic Magnetite Colloidal Nanocrystal Clusters* 2007 Angew. Chem. Int. Ed. 46 4342

[69] Z. Lu, Y. Yin Colloidal nanoparticle clusters: functional materials by design 2012 Chem. Soc. Rev. 41 6874–6887

[70] Casula M.F., Jun Y.W., Zaziski D.J, Chan E.M, Corrias A., Alivisatos A.P. *The concept of delayed nucleation in nanocrystal growth demonstrated for the case of iron oxide nanodisks* J. Am. Chem. Soc. 2006, 128,1675.

[71] W.W. Yu, E. Chang, C.M. Sayes, R. Drezek, V.L. Colvin *Aqueous dispersion of monodisperse magnetic iron oxide nanocrystals through phase transfer* 2006 Int. J. Nanotechnol. 17 4483

[72] V. K. La Mer, R. H. Dinegar *Theory, production and mechanism of formation of monodispersed hydrosols* 1950 J. Am. Chem. Soc. 72 4847-4854

[73] Ming Ma, Jun Xie, Yu Zhang, Zhongping Chen , Ning Gu *$Fe_3O_4@Pt$ nanoparticles with enhanced peroxidase-like catalytic activity* 2013 Materials Letters 105 36–39

[74] Yoo D., Lee J.H., Shin T.H., Cheon J. Theranostic Magnetic Nanoparticles 2011 Acc. Chem. Res. 44 863–874

[75] L. Lartigue, P.Hugounenq, D. Alloyeau, S.P. Clarke, M. Levy, J.C. Bacri, R. Bazzi, D. F. Brougham, C. Wilhelm, F. Gazeau *Cooperative Organization in Iron Oxide Multi-core Nanoparticles Potentiates Their Efficiency as Heating Mediators and MRI Contrast Agents* 2012 ACS Nano 6 12 10935-10949

[76] Abdulwahab K.O., Mohammad A. Malik, P. O'Brien, G. A. Timco, F. Tuna *A One-Pot Synthesis of Monodispersed Iron Cobalt Oxide and Iron Manganese Oxide Nanoparticles from Bimetallic Pivalate Clusters* 2014 Chem. Mater. 26 999

[77] J.Ge, Y. Hu, T. Zhang, T. Huynh, Y. Yin *Self-Assembly and Field-responsive Optical Diffractions of Superparamagnetic Colloids* Langmuir 2008, 24, 3671-3680

[78] J.Ge, Y.Yin *Magnetically responsive colloidal photonic crystals* J. Mater. Chem. 2008 18 5041–5045

[79] G. F. Goya, T. S. Berquo´, F. C. Fonseca *Static and dynamic magnetic properties of spherical magnetite nanoparticles* 2003 Journal Of Applied Physics 94 5;

D. Mamula-Tartalja *Effects of manufacturing conditions and heating on properties of electrochemically produced magnetite nano-powders* Ceramics International 40 2014 3517

[80] http://imagej.nih.gov/ij/

[81] D.B. Williams, C.B. Carter *Transmission Electron Microscopy A Textbook for Materials Science* SPRINGER 2009

[82] PDF-2 International Centre for Diffraction Data 2007

[83] Pons T., Uyeda H.T., Medintz I.L., Mattoussi H.J. *Hydrodynamic Dimensions, Electrophoretic Mobility, and Stability of Hydrophilic Quantum Dots* 2006 Phys. Chem. B 110 20308–20316

[84] Bunker G. Introduction to XAFS: *A Practical Guide to X-ray Absorption Fine Structure Spectroscopy* 2010 Cambridge University Press

[85] K.E. Sapsford, K.M. Tyner, B.J. Dair, J.R. Deschamps, I.L. Medintz *Analyzing Nanomaterial Bioconjugates*: *A Review of Current and Emerging Purification and Characterization Techniques* 2011 Anal. Chem. 83 4453–4488

Acknowledgements

Ringraziamenti

Tante persone, ognuna a suo modo, ha fatto parte di questo lungo percorso, il quale mi ha portato, non senza difficoltà, a una profonda crescita interiore e intellettuale.
E' stata un'esperienza autentica, profondamente voluta e vissuta.
E' stata una esperienza bellissima.

Con grande affetto e profonda stima ringrazio il mio supervisore, Maria, per avermi dato la possibilità di far parte del Gruppo di Ricerca Materiali Funzionali presso il Dipartimento di Chimica e di collaborare con persone dall'alto profilo professionale, per tutto quello che mi ha insegnato e per avermi supportata e consigliata, stimolando la mia curiosità intellettuale e la mia sete di conoscenza.

Ringrazio e abbraccio i miei colleghi, Claudia, Tore, Matteo, Danilo che mi hanno accompagnata in questa parentesi della mia vita, con i quali ho riso, condiviso, discusso, ma che ogni giorno hanno contribuito a rendere questi 3 anni speciali e indimenticabili.

Ringrazio Andrea, Anna e Gavin per l'affetto e la disponibilità mostrata nei miei confronti, e per i preziosi insegnamenti. La vostra dedizione al lavoro e professionalità rappresentano un esempio da seguire per me, ogni giorno.

Ringrazio i miei genitori, che mi hanno sempre sostenuta e su(/o)pportata, che hanno sempre creduto in me e nelle mie scelte, e i miei nipotini, Nicola e Riccardo, perché il loro sorriso è stato spesso il regalo più grande.

Ringrazio Massimo, per la protezione, la stima e la pazienza con cui mi ha sostenuta e amata in questi anni.

Ringrazio tutti i miei amici, in particolare Didi, Amelie e Johanna, e con loro tutte le persone che continuano a credere in me.

Grazie a tutti di cuore.